Understanding growth rate limitations in production of single-crystal cadmium zinc telluride (CZT) by the traveling heater method (THM)

A DISSERTATION
SUBMITTED TO THE FACULTY OF THE GRADUATE SCHOOL
OF THE UNIVERSITY OF MINNESOTA
BY

Jeffrey H. Peterson

IN PARTIAL FULFILLMENT OF THE REQUIREMENTS
FOR THE DEGREE OF
DOCTOR OF PHILOSOPHY

Jeffrey J. Derby

March, 2017

Acknowledgements

I would like to acknowledge the many people who have helped me to complete my thesis and dissertation defense. First I would like to thank my advisor, Jeff Derby, for his continued support throughout my PhD and for his very helpful guidance in pursuing these projects. He has given me the opportunity to work in a variety of very interesting areas and has taught me so much about crystal growth, numerical methods, fluid mechanics, and more. Most of all though, I would like to thank him for encouraging my curiosity and allowing me to fully explore the topics that I wish to pursue. I would also like to thank the NSF and NNSA for their continued funding (with multiple no-cost extensions) throughout my PhD.

I would also like to thank some key figures in my personal development that have all contributed to my success. The late Dave Thurston was my junior biology teacher in high school and despite the very different subject from where I am today, he was a key teacher who reminded me just how fun an interesting science could be. After high school, the faculty at NMSU taught me the fundamentals I needed in this field and I am happy to forever be an Aggie. I especially wish to thank professors David Johnson and Charlie Johnson for their letters of recommendation when I was applying to graduate school. I never read these letters but from people who read my applications, I have heard that my recommendation letters were my strongest asset.

I am also deeply indebted to my mentors at Los Alamos National Laboratory, Chris Rousculp and Kevin Honnell. Working for them was a great experience and taught me so much about numerical modeling, equations of state, magnetohydrodynamics, statistical mechanics, and z-pinch experiments. They also gave me my first opportunities to present my work both at conferences and with our research collaborations. I'll never forget the collaboration we had with our Russian colleagues at the VNIIEF laboratory

in Sarov both because of the wool boots that they forced on our project lead, Bob, and because of the unique experience of giving a technical talk while it was simultaneously translated into Russian. Also, I would especially like to thank Barbara Devolder who saw my potential as a researcher and advocated for my hiring at LANL without ever having met me in person and even though I wasn't a good fit for her particular project. Getting a job at LANL was a key moment in my career both for my professional and personal development and I cannot emphasize enough how grateful I am that Barbara connected me with Chris in the first place. Without her, I definitely would not be here defending my thesis at the University of Minnesota right now.

My parents played an influential role in my life and I would like to thank them for their continued support. At the beginning of my life, they fostered within me the curiosity that has brought me to this point in my scientific career. I was encouraged to seek out answers to my own questions using my own resources, and this sense of independence has given me the drive to succeed in graduate school. Despite many frustrations and a learning process that may have felt glacial at times, I am forever thankful for the motivation to continue on a path of life-long learning. I would also like to thank the rest of my family and friends for your continued support and encouragement. Without this, I would not have been able to focus on my PhD.

Abstract

Cadmium telluride (CdTe) and cadmium zinc telluride (CZT) are important optoelectronic materials with applications ranging from medical imaging to nuclear materials monitoring. However, CZT and CdTe have long been plagued by second-phase particles, inhomogeneity, and other defects. The traveling heater method (THM) is a promising approach for growing CZT and other compound semiconductors that has been shown to grow detector-grade crystals.

In contrast to traditional directional solidification, the THM consists of a moving melt zone that simultaneously dissolves a polycrystalline feed while producing a single-crystal of material. Additionally, the melt is highly enriched in tellurium, which allows for growth at lower temperatures, limiting the presence of precipitated tellurium second-phase particles in the final crystal. Unfortunately, the THM growth of CZT is limited to millimeters per day when other growth techniques can grow an order of magnitude faster.

To understand these growth limits, we employ a mathematical model of the THM system that is formulated to realistically represent the interactions of heat and species transport, fluid flow, and interfacial dissolution and growth under conditions of local thermodynamic equilibrium and steady-state growth. We examine the complicated interactions among zone geometry, continuum transport, phase change, and fluid flow driven by buoyancy. Of particular interest and importance is the formation of flow structures in the liquid zone of the THM that arise from the same physical mechanism as lee waves in atmospheric flows and demonstrate the same characteristic Brunt–Väisälä scaling. We show that flow stagnation and reversal associated with lee-wave formation are responsible for the accumulation of tellurium and supercooled liquid near the growth interface, even when the lee-wave vortex is not readily apparent in the overall flow structure. The supercooled fluid is posited to result in morphological instability at growth rates far below the limit predicted by the classical criterion by Tiller *et al.* for constitutional supercooling.

Contents

Acknowledgements **i**

Abstract **iii**

List of Tables **vii**

List of Figures **viii**

1 Introduction **1**

1.1 The promise of CZT: small-scale detectors for gamma ray detection . . 1

1.2 Previous modeling efforts 6

1.3 Organization of thesis 8

2 Mathematical model of Traveling Heater Method (THM) system **12**

2.1 Field phenomena 14

2.2 Boundary Conditions 15

2.2.1 Growth and dissolution interfaces 15

2.2.2 Other boundary conditions 17

2.3 The quasi-steady approximation 18

2.4 Approximating the traveling heater 19

2.5 System description 22

2.6 Material properties and uncertainty 22

3 Numerical method **26**

3.1 Finite Element Approximation 26

3.2 Elliptic mesh generation 28
3.3 Residual equations 29
3.4 Application of boundary conditions 31
3.5 Solution method 32

4 Effect of gravity and zone size 36
4.1 Behavior without flow 36
4.2 Effect of buoyant flow 39
4.3 Influence of zone size and ampoule radius 44
4.3.1 Influence of ampoule radius 44
4.3.2 Influence of zone length 45
4.4 Conclusions 47

5 Evolution of lee waves and the effect of constitutional supercooling 50
5.1 An introduction to lee waves 50
5.2 Presence of lee waves in the THM system 54
5.2.1 The Kelvin-Helmholtz instability and its connection to the lee wave 57
5.3 Lee waves and constitutional supercooling 62
5.3.1 An introduction to constitutional supercooling 62
5.3.2 Constitutional supercooling limits growth in the THM system . . 67
5.4 Conclusions 69

6 Improving interface morphology in the Bridgman growth technique 72
6.1 Introduction and prior Literature 72
6.2 Heat transfer analysis 74
6.2.1 Analysis 76
6.3 Application of criterion 78
6.3.1 Prior studies 78
6.3.2 Application to furnace design 80
6.4 Conclusions 82

7 Concluding Remarks 85
7.1 Summary of thesis and discussion of results 85

7.2 Directions for future work 87
7.2.1 Interface instability 87
7.2.2 Use of accelerated crucible rotation technique (ACRT) to eliminate lee waves 92
7.2.3 Magnetic fields in the THM system 102
7.2.4 Generalization of axial inflection point criterion in Bridgman systems to include the effects of thermal conductivity and latent heat 104

Bibliography **106**

Appendix A. License agreements allowing reproduction of published work in this thesis **118**

List of Tables

2.1 Physical properties used in the simulations. 24

List of Figures

1.1 Schematic of the vertical Bridgman (a) and Traveling Heater Method (THM) (b) crystal growth configurations. In Bridgman growth, the crystal grows into a stationary melt whereas in the THM, the melt moves along with a traveling heater, simultaneously solidifying a crystal while dissolving a feed. 3

1.2 THM process for growth of CdTe starting with the initial setup (a), the beginning of growth (b), and an intermediate stage of growth (c). 4

1.3 Phase diagram of CdTe including typical operating paths for both the Bridgman and THM processes. Plot is reproduced from Greenberg[1] and the area near 50% tellurium has been magnified to see the coexistence region. 5

2.1 Schematic (left of symmetry line) and mesh (right) representations of the THM system. The heater is moved upwards in the growth direction and slowly dissolves CdTe or CZT from the feed while simultaneously solidifying a crystal of similar composition. The melt zone consists of 90 radial and axial elements with greater element density at the boundaries. 13

2.2 (a) Results from CrysMAS furnace simulations of a hypothetical THM setup. The left side shows the computational mesh used and the right depicts the temperature field with hotter temperatures shown in red. (b) Comparison between the effective furnace temperature calculated from equation 2.18 and a Gaussian temperature profile. 20

3.1 Schematic representation of the isoparametric mapping of elements from the r-z coordinate frame onto a parent element defined on the unit square in ξ-η space. 27

4.1 Contour plots showing two views of the melt zone and surrounding solid regions for growth at 2.49 mm/day in a 3.2-cm diameter ampoule without buoyancy effects (computed by setting $g = 0$). The spacing between isotherms is 1.16 K, and the maximum temperature is 1005 K. 37
4.2 Contour plots showing the effect of increasing buoyant forces at a growth rate of 1.24 mm/day in a 3.2-cm ampoule, for gravity levels of (a) 0.01% g, (b) 1% g, and (c) full gravity. The spacing between isotherms in each figure is 1.16 K, and the maximum temperature in each figure is approximately 1000 K. Negative streamfunction values denote clockwise rotation, and positive values denote anti-clockwise rotation. 41
4.3 Two scaling regimes are demonstrated by Reynolds number plotted against the Grashof number for ampoules of 3.2-cm and 4.8-cm diameters. The dimensionless Reynolds and Grashof numbers are calculated from eqs. (4.3) and (4.4), respectively. 43
4.4 Contour plots of streamlines and isotherms in the 4.8-cm ampoule at a growth rate of 0.90 mm/day for gravity levels of (a) 40% gravity and (b) full gravity. The flow pattern in (a) is very similar to that in the 3.2-cm ampoule at full gravity. 44
4.5 Contour plots of streamlines and isotherms in the 3.8-cm ampoule for excess tellurium masses of (a) 43.5 g, (b) 50.8 g, (c), 58.6 g, (d) 70.4 g, (e) 82.1 g, (f) 91.7 g. Streamfunction extrema are indicated within each figure along with the maximum fluid speed. 46
5.1 Schematic representation of how lee waves are formed in the atmosphere. Air flows over a perturbation (a) forming waves that persist downwind of the initial perturbation. As the air rises, it cools adiabatically through expansion and can sometimes condense water vapor to form clouds (b). These clouds take on the form of the oscillation and so tend to form a lens-like shape. Additionally, the air between the oscillation and the ground can become turbulent and produce counter-rotating vortices under the wave peaks. 51

5.2 Satellite image of lee waves produced by Amsterdam Island off the coast of Antarctica in the south Indian Ocean. This photo was captured by the Moderate Resolution Imaging Spectroradiometer (MODIS) flying onboard NASA's Terra satellite [2]. 52

5.3 (a) Different furnace profiles are used to investigate the scaling relationship between the Brunt-Väisälä period and the thermal gradient. The thick black line represents the original Gaussian profile with parameters given in Table 2.1. (b) Log-log plot of the Brunt-Väisälä period, τ_{BV}, associated with the lee wave versus axial thermal gradient. The filled circle represents the state shown in Figure 4.2(c). 55

5.4 Contour plots showing the effect of decreasing the zone size at zero growth rate in a 3.2-cm diameter ampoule with initial tellurium loading of (a) 70.4 g, (b) 62.6 g, and (c) 50.8 g. The spacing between isotherms in each figure is 1.16 K, and the maximum temperature in each case is approximately 1000 K. The streamline spacing employed here does not capture the lee-wave vortex for the cases shown in (b) and (c); however, local positive streamfunction maxima, indicated for each case, show that flow reversal occurs. 56

5.5 Schematic explanation for the Kelvin-Helmholtz instability depicting two fluid packets moving at velocities v_1 and v_2. As the two fluid packets exchange places, the buoyant potential increases but the kinetic energy decreases. For a Kelvin-Helmholtz instability to form, the decrease in kinetic energy must be greater than the increase in buoyant potential energy. 58

5.6 Structure of the lee wave in 4.8-cm diameter ampoule shown for applied thermal profiles with gradients of (a) 10 K/cm, (b) 40 K/cm, and (c) 120 K/cm at the approximate location of the growth interface. The Richardson number, Ri, is calculated from the thermal gradient and the z-gradient of the radial velocity at the positions marked by a star. . . . 61

5.7 Schematic representation of constitutional supercooling. As the growth interface advances, excess tellurium is rejected in front of the growing interface (a). The concentration can be directly mapped into a local melting point via the phase diagram (b). The melting point can then be plotted as a function of position in front of the interface (c). If the local melting point exceeds the local temperature, the liquid is considered undercooled. 63

5.8 Schematic process by which an interface becomes unstable in the presence of constitutional supercooling. The sub-figures represent (a) the initial perturbation forming, (b) the rearrangement of the composition field in response to the perturbation, and (c) the resulting growth of the instability under supercooled conditions. The schematic on the left represents the concentration field with darker shading corresponding to higher concentrations. In the plots of temperature and concentration (right and middle respectively), the circle and diamond represent the corresponding points in the schematic at left with the dashed lines corresponding to values in front of the perturbation peak. Faded lines indicate the previous state of the system. Note that in the plot of melting point, the circle and diamond will not necessarily lie on the melting point line, indicating a driving force for solidification or melting. 65

5.9 Contour plots of tellurium concentration and temperature for growth rates of (a) 1.5 mm/day and (b) 2.32 mm/day for the case of 50.8 g of initial tellurium in the 3.2-cm ampoule (the same case shown by Figure 5.4c). Supercooled regions are represented by the shaded area near the interface, while the dashed lines indicate the positions where the plots of Fig. 5.10 are constructed. 68

5.10 Temperature and composition-dependent melting point profiles in the liquid zone are plotted as a function of axial position along lines of (a) $r = 1.2$ cm and (b) $r = 0$ cm. Each line begins at the growth interface and continues into the liquid zone. Constitutionally supercooled regions, where the local melting point is higher than the local temperature, are identified by shaded areas. 70

6.1 Schematic of heat transfer in a crystal growth system (a) without a booster and (b) with a booster heater. The booster heater tends to cause the heat flux lines to converge inward at the location of the interface, promoting a convex shape. 75
6.2 Schematic representation heat fluxes in a system with a booster heater and showing that heat is removed radially below the growth interface. In (a), the interface shape is convex due to the fact that the interface is located in the region where the radial component of the heat flux is negative. However in (b), the interface is located where the radial component of the heat flux is positive and a concave shape results. . . . 77
6.3 Top: Axial furnace temperatures; dashed indicates linear profile and solid is the bell-curve profile. Bottom: Simulations of CZT growth under the two profiles. A convex interface shape is produced by the bell-curve profile, which exhibits negative curvature above the melting point. Adapted from [3] with permission from Elsevier. 79
6.4 Two designs for a four-zone Bridgman with temperature isotherms plotted on the right side of each image. In (a), the furnace design incorporates a booster heater but also shows a concave growth interface. By adding a baffle zone below the booster heater in (b), the interface has been transformed from concave to convex. 81
6.5 Axial thermal profiles of the two furnace designs shown in Fig. 6.4. The design with the baffle produces a region of negative curvature in the profile around the melting point. 83
7.1 Heat flux lines for a linear temperature field with a perturbed interface both excluding (a) and including (b) the effect of latent heat. If the perturbation is growing, latent heat will be released at the perturbation peaks and will distort the thermal field such that the heat flux lines resemble the situation shown in (b). The resulting melting point isotherm will then be exactly out of phase with the initial perturbation, causing the interface to return to a planar configuration. 90

7.2 A higher solid thermal conductivity will favor heat flowing more through the solid than the melt, diverting the heat fluxes so that the resulting isotherm is in phase with the original perturbation. Conversely, the isotherm will be out of phase with the original perturbation when the melt has a higher thermal conductivity. 91
7.3 Schematic representation of an ACRT cycle with Ekman flows and the vortices they cause shown in white. Taylor-Görtler vortices appear at the edges of the melt zone near the ampoule wall during the deceleration phase. 94
7.4 Contour plots of excess tellurium concentration and the Stokes streamfunction at a growth rate of 4.06 mm/day for two different ACRT cycles, ACRT1 and ACRT2, in (a) and (b) respectively. Undercooled melt is identified by the shaded region in the concentration contours. Positive values for the streamfunction indicate a clock-wise vortex while negative values (shown as dashed contours) represent counter-clockwise vortices. Both images represent a time 60% through an ACRT cycle after the system has reached a periodic steady state. 97
7.5 Contour plots showing interface stability. On each plot, time is plotted on the vertical axis while the radius scaled by the surface area is plotted on the horizontal axis. Figures (a) and (c) are produced by measuring the instantaneous Sekerka number given by equation 7.5 where white space indicates a stabilizing environment at that position and time. Figures (b) and (d) represent cumulative effect of destabilizing influences over time given by equation 7.8; contours are then a rough measure of how large an instability has grown on the interface. Sub-figures (a) and (b) correspond to the ACRT1 cycle of figure 7.4 (a) while sub-figures (c) and (d) correspond to ACRT2 in figure 7.4 (b). 99

Chapter 1

Introduction

1.1 The promise of CZT: small-scale detectors for gamma ray detection

Ever since Wilhelm Röntgen first detected x-rays using a fluorescent plate in 1895, radiation detection has been a field with diverse applications [4]; indeed, Röntgen made the first x-ray of his wife's hand. Shortly after Röntgen's discovery, gamma rays were also discovered with Paul Villard first observing them and then Ernest Rutherford giving them their name. While x-rays indicate electronic transitions within an atom, gamma rays are fundamentally different in that they indicate nuclear transitions and are in general produced through radioactive decay. As a result, the applications for gamma rays [5] are subtly different than for X-rays.

In medicine, gamma ray detectors are used in positron emission tomography (PET) [6], a technique that is becoming more and more ubiquitous with many applications both in diagnostic medicine and in treatment [7]. Most notably, the technique has found widespread use due to its ability easily penetrate soft tissue and to be specifically targeted. PET works by detecting the characteristic gamma ray produced when the positron emitted from a radioactive nucleus annihilates with an electron to become pure energy. When the radioactive positron-emitter is paired with a molecule targeted to specific types of cells, PET can be a very powerful diagnostic tool.

Gamma detection is also vital for the monitoring of nuclear materials [8, 9]. With

the creation of the International Atomic Energy Agency (IAEA), the world has committed itself making nuclear power available to all countries while also safeguarding against proliferation of nuclear weapons. Integral to this mission is the reliable detection, classification, and accounting of nuclear materials, with gamma ray detectors providing one of the primary non-destructive tools available for determining the isotopes present in a given sample of nuclear material. As a result, there is a strong desire to miniaturize gamma ray detectors to allow for more portable use.

Two primary classes of devices exist for the detection of gamma rays: scintillators and semiconductors. Sodium iodide (NaI) and cesium iodide (CeI) are two of the most common scintillators in use today but suffer from low spatial and energy resolution [9]. Semiconductor-based detectors are at present mostly made from high purity germanium (HPG) and typically improve on both of these issues. However, HPG is prohibitively expensive for a number of applications because the germanium must be grown with defect densities on the order of 10^{10} defects per cm^3 [10]. Also, germanium has a relatively small bandgap, meaning that there are a significant number of electrons in the conduction band at room temperature. Consequently, HPG detectors are generally operated at liquid nitrogen temperatures, further increasing cost and size. Cadmium zinc telluride is another semiconductor gamma ray detector that has gained interest due to the fact that it can operate at or near room temperature, greatly simplifying and miniaturizing the final devices.

Traditionally, CdTe and CZT have been produced via the Bridgman process shown in Figure 1.1 (a), but the crystals are often plagued by the formation of second-phase tellurium particles, inhomogeneity, and other defects [11, 12]. The traveling heater method (THM) is an alternative growth technique that has been shown to successfully produce detector-grade material [13, 14, 15]. Unlike traditional directional solidification, the THM uses a melt zone that is highly enriched in tellurium. This liquid zone is moved with a traveling heater, dissolving a polycrystalline feed at one interface while simultaneously growing single-crystal material of a similar composition at the opposite interface (see Figure 1.1 (b)). Because the liquid zone is most accurately described as cadmium dissolved in a molten tellurium solvent, the THM system is also sometimes classified as a solution growth technique. Indeed, similar growth processes include the traveling solvent method (TSM) and the traveling solution growth (TSG) technique.

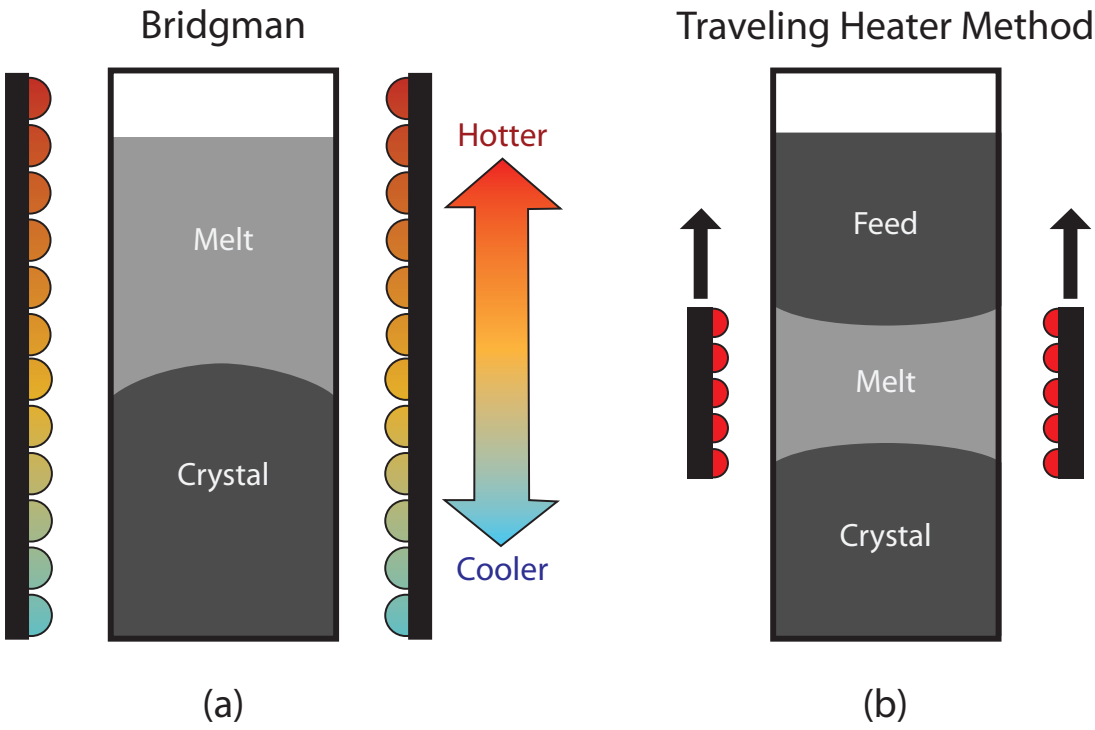

Figure 1.1: Schematic of the vertical Bridgman (a) and Traveling Heater Method (THM) (b) crystal growth configurations. In Bridgman growth, the crystal grows into a stationary melt whereas in the THM, the melt moves along with a traveling heater, simultaneously solidifying a crystal while dissolving a feed.

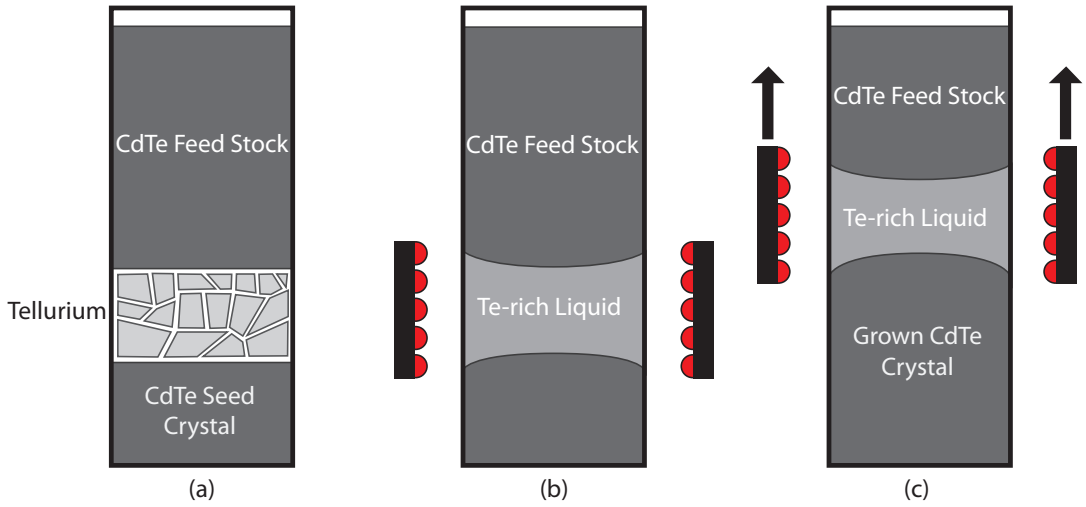

Figure 1.2: THM process for growth of CdTe starting with the initial setup (a), the beginning of growth (b), and an intermediate stage of growth (c).

In the THM process depicted in figure 1.2 (a), the ampoule is initially loaded with a seed crystal at the base, pure tellurium in the middle, and CdTe ingots on top (the seed crystal is omitted when a tapered ampoule is used to promote a single nucleation event). At the beginning of growth, (b), the heater is used to melt the pure tellurium and dissolve some of the CdTe (the amount of which depends on the temperature of the heater and thermodynamics) to form a liquid zone with a high tellurium concentration. This zone then moves as the heater is translated upwards, shown in (c), with the composition remaining relatively constant throughout growth. From the moving liquid frame of reference then, there is a constant flux of CdTe through the liquid zone from feed to crystal as the process operates. If the solid feed contains any excess tellurium (tellurium in excess of the stoichiometric composition), it will cause the size of the liquid zone to increase as the excess tellurium depresses the melting point of the solution until it is diluted by dissolved CdTe.

While CZT solidifies at compositions very close to stoichiometry, figure 1.3 shows that there is actually a small coexistence region at elevated temperatures where excess tellurium is soluble in the solid CZT. While the coexistence region may appear quite large in the diagram, the reader is reminded that the horizontal scale has been purposely enlarged. The Bridgman process is typically operated with a melt that is only slightly

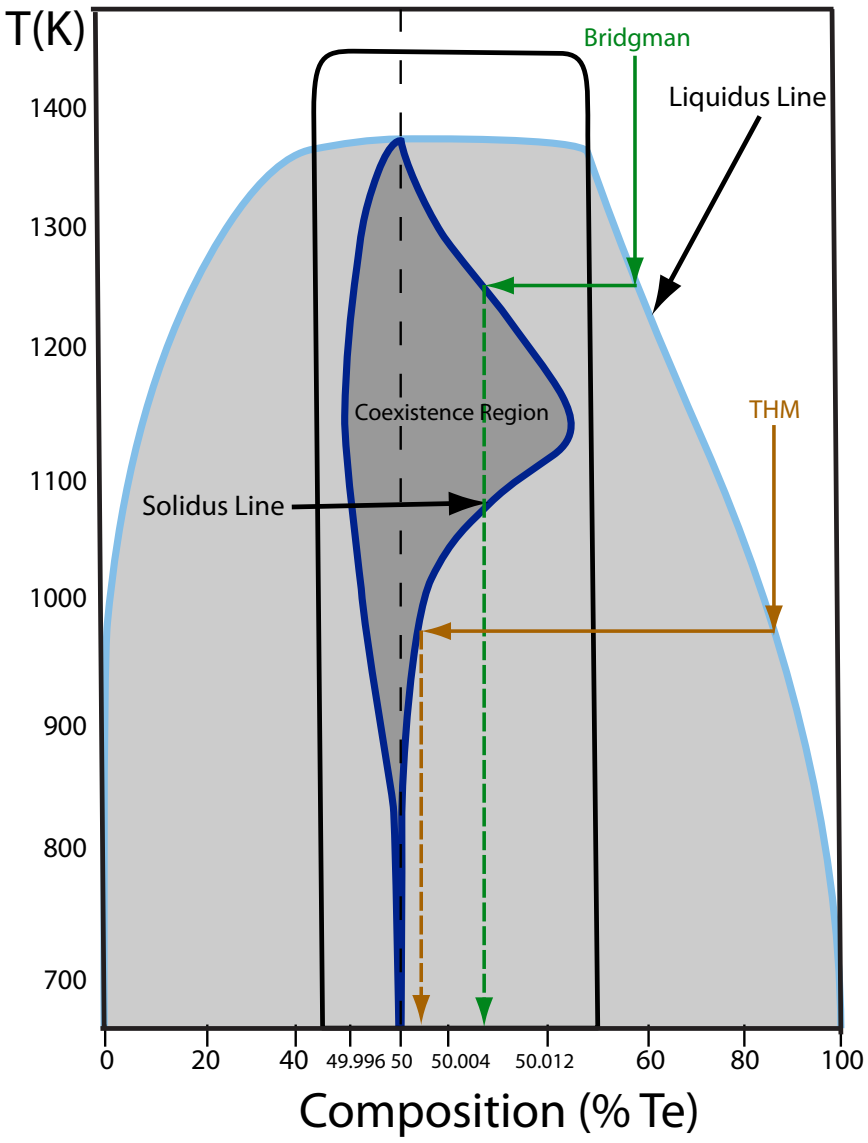

Figure 1.3: Phase diagram of CdTe including typical operating paths for both the Bridgman and THM processes. Plot is reproduced from Greenberg[1] and the area near 50% tellurium has been magnified to see the coexistence region.

enriched in tellurium. On the phase diagram however, the liquid is in equilibrium with a solid that contains a significant amount of excess tellurium. As the solid cools, the excess tellurium will precipitate from the solid-solid solution and second-phase particles will form that are detrimental to device performance [11, 12]. By contrast, the THM solidifies at a much higher tellurium concentration and at a lower temperature. The solid composition in equilibrium with this liquid is actually much closer to stoichiometry and so the danger of precipitates is reduced. For this reason and others, the THM is currently used for much of the production of detector-grade CZT.

Despite the advantages the THM system enjoys, it is currently hampered by growth rates on the order of millimeters per day [16, 15, 14, 13, 17] and by growth interface instabilities [17, 18, 19]. While the THM can reduce the number of second-phase tellurium particles compared to other growth processes [14], many THM ingots still contain levels of these particles that are unacceptable for detector applications. However, improving the THM processes is extremely challenging owing to the very low growth rates (that limit the number of trial and error experiments that can be performed) and the complexity of the process itself. The motivation for the work presented here is to develop a rigorous mathematical model for the traveling heater method and apply it toward a better understanding of the mechanistic workings of the process.

1.2 Previous modeling efforts

Compared to other crystal growth systems, there have been relatively few mathematical models of the THM process. The first description was given by Broder and Wolff [20] for the growth of gallium phosphide over fifty years ago. More than a decade after the study by Broder and Wolff, the seminal work by Wald and Bell first reported the use of the THM in the growth of CdTe [21]. However, Wald and Bell focused mainly on providing a simple model for heat transfer. Chang *et al.* [22] developed a steady-state model for the THM growth of mercury cadmium telluride (MCT) that was capable of representing both dissolution and growth interfaces. However, their model ignored convection in the liquid zone and its effects on heat and mass transport. Apanovich and Ljumkis [23] also considered MCT growth via the traveling heater method. Unlike the prior work of Chang *et al.*, they represented liquid flow in the zone, driven by both thermal and

solutal buoyancy. Their model solved for time-dependent states, but interface velocities were represented via kinetic expressions that assumed the growth to be proportional to the local departure of the liquid composition from equilibrium, an assumption that is likely invalid for the very low growth rates employed in this system.

Lan and Yang [24] constructed a steady-state model for the traveling solvent method that was well-posed and physically consistent. Their studies presented remarkable insight on the strong coupling between transport and thermodynamics in this system. We assert that this has been the most insightful of all prior modeling studies of the traveling heater method. Not only was their model comprehensive and correct, but their study presented a compelling investigation of various parameters in the system. The primary limitation of their analysis was a lack of computational power that prevented the accurate resolution of key flow patterns in the melt.

Ye *et al.* [25] employed a finite-element model to compute heat and mass transfer along with thermosolutal convection in the liquid zone during THM growth of CdTe. However, they assumed a fixed liquid zone with flat interfaces and ignored segregation effects at the growth and dissolution interfaces. Barz *et al.* [26] were among the first to apply numerical simulation to study the effects of the accelerated crucible rotation technique (ACRT) on flows within the liquid zone during the THM growth of CdTe. However, their analysis also assumed a simple zone geometry with flat interfaces and idealized heater input.

Ghaddar *et al.* [27] considered the influence of rotating magnetic fields on zone convection during the THM growth of CdTe using a steady-state model that included fluid flow and heat and mass transfer through the liquid zone. While the effects of latent heat were included at both interfaces, simplified interfacial composition conditions were employed that prescribed a constant composition at the dissolution interface and constant flux conditions at the growth interface. Martinez-Tomas *et al.* [28] applied the commercial code FLUENT to model the THM growth of HgTe. While these authors employed an integral constraint for solvent composition appropriate for a steady-state description of this process, the detailed boundary conditions applied at the dissolution and growth interfaces were not clearly stated.

Okano *et al.* [29] developed a transient model to study THM growth of GaSb that included flow, transport, and phase diagram information; however, they did not include

segregation at either solid-liquid interface. Models by Dost and co-workers [30, 31] have been applied to study THM growth of CdTe. These models described heat and mass transfer, fluid flow in the zone, and interfaces that follow the liquidus temperature according to local concentration; however, like the earlier model by Okano *et al.* [29], they did not account for segregation effects occurring at the interfaces.

Most recently, Stelian and Duffar [19] have employed numerical modeling to investigate CdTe grown under terrestrial and microgravity conditions by the traveling solution growth method. Their model included heat and mass transfer as well as flow driven by buoyancy and provided an accounting for segregation and compositional dependence of the phase change temperature at the growth interface. However, they hypothesized that the dissolution interface was characterized by a constant temperature, an assumption that is not consistent with the thermodynamic liquidus curve. Nevertheless, they were able to broadly survey the effect of melt convection under the different driving forces and concluded that terrestrial growth was limited by morphological destabilization which could be ameliorated under microgravity conditions.

With the exception of the model of Lan and Yang [24], we argue that all of the prior attempts to model this complicated system have been flawed by ignoring important transport phenomena or by inconsistent application of thermodynamic concepts. We address these shortcomings in the model presented here. We also take advantage of the much greater computational resources available today to resolve important and interesting flow phenomena in the liquid zone and discuss their impact on growth behavior. In the following discussion, we demonstrate the strongly coupled nature of the THM growth process, which makes process improvement extremely challenging.

1.3 Organization of thesis

The primary purpose of this thesis is to present an understanding of the growth rate limitations inherent in the THM system. In the previous sections, CZT was presented as a material of promise in the creation of compact radiation detectors. However, current production is limited by low yields due both to slow growth rates and difficulties in growing large-scale crystals. This thesis first presents a mathematical description of the THM system and then presents results from that model both explaining the fundamental

aspects of the system and demonstrating that the presence of standing waves in the melt are responsible for the slow growth rates in the traveling heater method.

In chapter 2, a 2-D axisymmetric mathematical model of the THM system is presented, comprising equations for the conservation of energy, mass, momentum, and chemical species. Boundary conditions are also presented that rigorously take into account the thermodynamically-determined equilibrium melting point as well as the effects of latent heat, segregation, and moving interfaces. A discussion of the quasi-steady approximation is also presented with specific emphasis given to describing the system via a moving reference frame in order to rigorously pose the problem in a steady-state. We also discuss the need to add an additional constraint condition on the species equations in order for the problem to be well-posed. A simple radiation heat transfer model for the furnace is also presented that is applied to the crystal growth system through use of a radiation heat transfer boundary condition. The system geometry and material properties of the system are included along with a discussion of the uncertainty in the material properties and the need to estimate certain quantities.

In chapter 3, a brief description of the Galerkin Finite Element method used to solve this problem is presented. In order to solve for the position of the phase-change interfaces, elliptic mesh equations are also solved, allowing the mesh to freely deform as the interfaces move. The residual equations are shown along with the weak formulations of the field equations that are to be solved. The system of non-linear equations is first linearized through the Newton-Raphson method and the resulting equations are solved using Gaussian elimination. We also discuss how first-order continuation is used to traverse parameter space and arrive at the base-case solution.

In chapter 4, the fundamental behavior of the THM system is presented. First, the a buoyancy-free case is analyzed to illustrate the effects of mass transfer on the system and to demonstrate behavior under microgravity conditions. Next, buoyancy is added through first-order continuation in the magnitude of gravity. At various levels of gravity, the thermal and solutal Peclet numbers both provide important measures of the system through which the fundamental driving forces can be explained. With full gravity, the strength of buoyancy is strong enough that the non-linear terms in the Navier-Stokes equations begin to dominate. As a result, multiple flow cells appear, and we show that this flow is primarily responsible for determining the interface shape. Additionally, we

examine the influence of both ampoule radius and liquid zone length and find that the non-linear behavior is extremely dependent on the dimensions of the system.

In chapter 5, we explain the mechanism by which growth rates are severely limited in the THM system. We identify the presence of lee waves, a phenomena normally associated with cloud formation, as responsible for the counter-rotating vortex present at the growth interface. To prove this, a scaling relationship is identified between the Brunt-Väisälä period and the thermal gradient in the system. Upon varying the heater profile, we see that the predicted behavior is observed for the lee wave under different thermal gradients. At large gradients, we assert that the departure from this scaling is caused by wave shear related to the Kelvin-Helmholtz instability. Most importantly, we show that the lee wave is responsible for disrupting the tellurium transport at the growth interface by inhibiting the natural convection into the bulk of the melt. As the tellurium gradient increases, the melt in front of the growth interface becomes constitutionally supercooled, possibly leading to a condition of morphological instability for the growth interface. We then conclude that constitutional supercooling, driven by the formation of the lee wave, is responsible for the slow growth rates in the THM system.

In chapter 6, a departure from the study of the THM system is taken to present a method for controlling the shape of the growth interface in the Bridgman crystal growth system. We review previous literature and find multiple *ad hoc* methods for controlling the shape and then attempt to unify these ideas under a more general mathematical framework. Using straight-forward heat transfer arguments, we show that the shape of the growth interface can be largely predicted from an analysis of the axial temperature profile. Specifically, we find that a convex interface shape can be promoted when the curvature of the axial temperature profile is negative, i.e. $\mathrm{d}^2T/\mathrm{d}z^2 < 0$. We prove this both by reexamining the prior studies and through use of heat transfer simulations to show the axial temperature profile can be independently used to infer trends in the shape of the growth interface.

Finally in chapter 7, the thesis is concluded with a summary of the results presented along with directions for future research. We first focus on the need to understand the connection between morphological instability and constitutional supercooling in this system, making heavy use of the seminal work by Mullins and Sekerka [32]. Next, we examine ideas for introducing forced convection into the THM system including

the use of the accelerated crucible rotation technique (ACRT) and magnetic fields. Preliminary results are also presented showing simulations of the THM system with the ACRT applied, showing that the presence or absence of undercooling is not itself indicative of a an unstable interface. Finally, we offer future directions for extending the Bridgman interface control criterion to incorporate the effects of latent heat and thermal conductivity.

Chapter 2

Mathematical model of Traveling Heater Method (THM) system

Modeling the traveling heater method presents additional challenges compared to models for classical melt crystal growth processes. Foremost is faithfully representing the role of thermodynamics and the liquid zone. A key idea is the enforcement of local thermodynamic equilibrium at both dissolution and growth interfaces. We argue that the extremely slow rate of movement of the traveling heater (typically on the order of 1–10 mm/day) results in interfaces that can, for all practical purposes, be assumed to separate liquid and solid phases at equilibrium. This assumption has long been used to describe solidifying interfaces in melt crystal growth systems [33, 34, 32, 35], unless kinetic factors are at play that demand a departure from equilibria [36]. We describe in ensuing discussion how this assumption of equilibrium phase behavior is enforced via model boundary conditions.

A schematic representation of the model domains in an axisymmetric coordinate system is shown in Figure 2.1 showing the different parts of the system. The simulation domain consists of the grown CdTe crystal, the melt out of which the crystal has grown, a CdTe feed that dissolves into the melt zone, and an ampoule that contains the entire system. In all equations presented, vectors are denoted by bold-faced serif letters ($\mathbf{v}$), scalar values by italicized serif letters (C), and second-order tensors by bold-faced sans serif capital letters (T). We solve the governing equations in a frame of reference that

is moving with the traveling heater, which makes the solution for quasi-steady states straightforward. This approach is further discussed below.

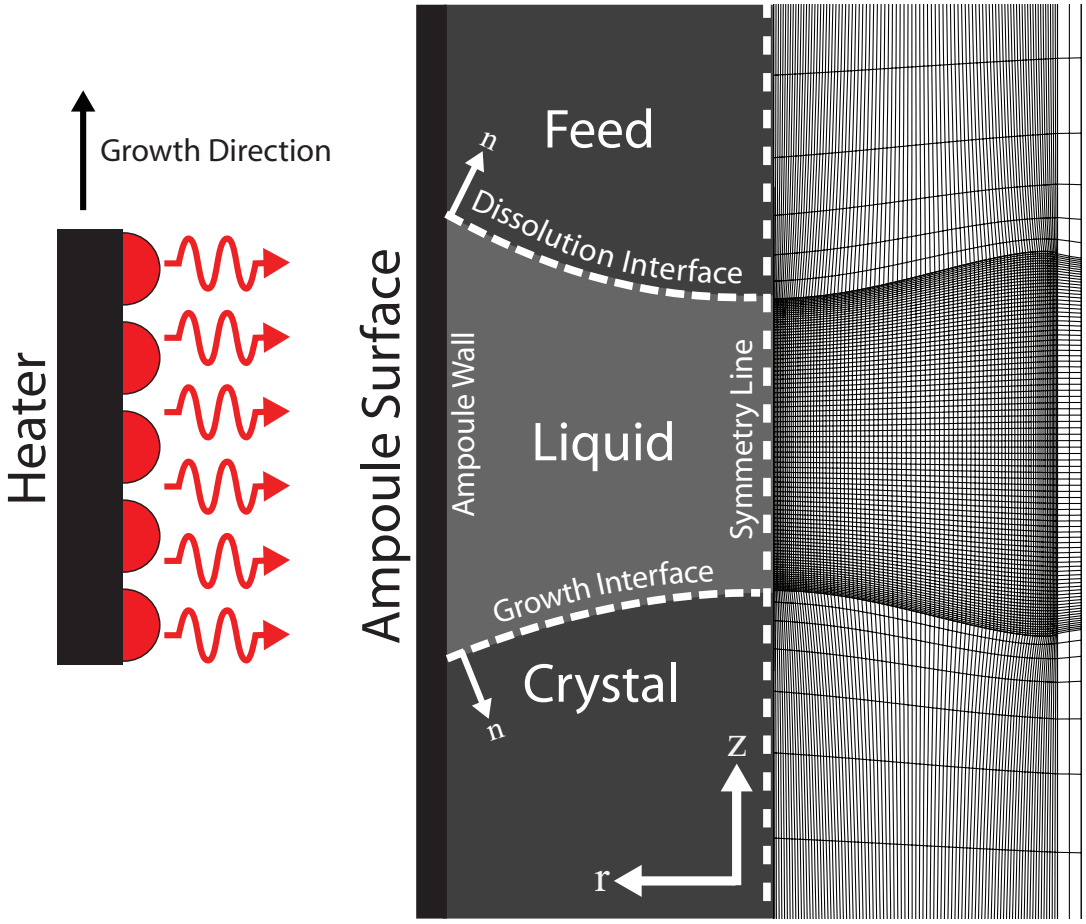

Figure 2.1: Schematic (left of symmetry line) and mesh (right) representations of the THM system. The heater is moved upwards in the growth direction and slowly dissolves CdTe or CZT from the feed while simultaneously solidifying a crystal of similar composition. The melt zone consists of 90 radial and axial elements with greater element density at the boundaries.

2.1 Field phenomena

Heat transfer is calculated throughout the entire ampoule and its contents through application of the energy conservation equation written in vector notation as

$$\frac{\partial T}{\partial t} + \mathbf{u} \cdot \nabla T = \alpha_i \nabla^2 T. \tag{2.1}$$

Here, T is the temperature, $\mathbf{u}$ is the velocity vector, and $\alpha_i \equiv k_i/\rho_i C_{\mathrm{p},i}$ is the thermal diffusivity of material i, where k_i, ρ_i, and $C_{\mathrm{p},i}$ are thermal conductivity, density, and heat capacity. Partial derivatives with respect to position are represented by the gradient operator, ∇, and the Laplacian operator, ∇^2, while partial derivatives with respect to time are denoted as $\partial/\partial t$.

Composition fields are calculated using the species conservation equation,

$$\frac{\partial C_j}{\partial t} + \mathbf{u} \cdot \nabla C_j = \mathcal{D}_j \nabla^2 C_j, \tag{2.2}$$

where C_j is the mole fraction of species j and $\mathcal{D}_j$ is the corresponding diffusivity. The actual species making up the liquid are likely more complex than atomic Cd and Te. For example, Moskvin *et al.* [37] put forth a polyassociative model, positing the existence of several complexes in the liquid phase, which accurately represents phase equilibria over wide temperature and composition ranges. This model predicts that associated CdTe is the prevailing species in near-stoichiometric liquids, with free Te atoms increasing as the liquid composition becomes increasingly tellurium rich. However, their model predicts that the concentration of the CdTe complex dramatically decreases as Te mole fractions increase beyond approximately 0.6, being replaced by complexes of Cd_2Te_3 and $CdTe_2$.

We assume in this study that the primary species of interest in the liquid are associated CdTe with excess free Te. According to the model of Moskvin *et al.* [37], this approach is likely realistic near stoichiometry but becomes less so at high tellurium concentrations. Nevertheless, we believe that the simplicity of this approach is justified for the initial studies presented here. Henceforth, the j subscript will be dropped from eq. (2.2), and only mass transport of liquid-phase, excess tellurium is considered in our model. The composition of the liquid will be represented via the total mole fraction of tellurium, C, or the mole fraction of *excess* tellurium, C', defined as $C' = C - 0.5$. The excess tellurium is a measure of the mole fraction of free Te in the presence of the

associated CdTe complex. Note that C and C' are interchangeable in eq. (2.2), because they only differ by a constant.

Within the liquid domain, the velocity $\mathbf{u}(r,z)$ and dynamic pressure $p(r,z)$ are calculated from the Navier-Stokes and continuity equations written for an incompressible fluid. The well-known Boussinesq approximation is used to couple the Navier-Stokes equations with energy and species conservation, giving:

$$\rho_l\Big(\frac{\partial \mathbf{u}}{\partial t} + \mathbf{u}\cdot\nabla\mathbf{u}\Big) = \nabla\cdot\mathbf{T} + \rho_l\mathbf{g}[1+\beta_{\mathrm{T}}(T_0-T)+\beta_{\mathrm{S}}(C_0-C)], \tag{2.3}$$

$$\nabla\cdot\mathbf{u} = 0, \tag{2.4}$$

where $\mathbf{T}$ is the stress tensor for a Newtonian fluid,

$$\mathbf{T} = -p\mathbf{I} + \mu\Big(\nabla\mathbf{u} + (\nabla\mathbf{u})^{\mathrm{T}}\Big).$$

The density of the liquid is represented by ρ_l, β_T is the volumetric thermal expansion coefficient, β_S is the volumetric solutal expansion coefficient, $\mathbf{I}$ is the identity tensor, and μ is the viscosity of the liquid. The quantities T_0 and C_0 represent the temperature and composition, respectively, at which the liquid density is specified.

2.2 Boundary Conditions

2.2.1 Growth and dissolution interfaces

Solidification at the growth interface and melting at the dissolution interface results in the generation and absorption of latent heat, respectively. An energy balance across each interface represents heat fluxes through the liquid and solid, as well as latent heat evolution as,

$$k_l(\mathbf{n}\cdot\nabla T)|_l - k_s(\mathbf{n}\cdot\nabla T)|_s = \rho_l\Delta H_{\mathrm{f}}\mathbf{n}\cdot(v_{\mathrm{g}}\mathbf{e}_z + \dot{\mathbf{x}}), \tag{2.5}$$

where k_l and k_s are the liquid and solid thermal conductivities, $\mathbf{n}$ is the unit vector normal to the interface, pointed away from the melt, ρ_l is the liquid density, and ΔH_{f} is the latent heat of fusion. The latent heat term on the right-hand-side of this equation is multiplied by the local interface velocity, which is given by the normal component of $v_{\mathrm{g}}\mathbf{e}_z + \dot{\mathbf{x}}$, where v_{g} is the translation rate of the heater, $\mathbf{e}_z$ is the unit vector in the z direction (growth direction), and $\dot{\mathbf{x}}$ is the rate of change of the interface position with

respect to time (representing the deviation of the local growth velocity from the heater translation rate).

As argued in the previous section, we assume that both interfaces are governed by local thermodynamic equilibrium conditions, so that the solid phase is in equilibrium with its contacting liquid. Thus, we argue that both dissolution and growth interfaces must locally satisfy the condition that $C_s = K_{\mathrm{p}} C_l$, as prescribed by the phase diagram. Performing a species balance across either interface then involves representation of the diffusive flux of the species through liquid and solid to the interface via Fick's law, which then must balance the net flux of the species at the moving interface that arises from the discontinuous concentration between the liquid and solid phases. Mathematically, this condition is represented by,

$$\mathcal{D}_l(\mathbf{n}\cdot\nabla C)|_l - \mathcal{D}_s(\mathbf{n}\cdot\nabla C)|_s = -(1-K_{\mathrm{p}})C_l\ \mathbf{n}\cdot(v_{\mathrm{g}}\mathbf{e}_z + \dot{\mathbf{x}}), \tag{2.6}$$

where $K_p \equiv C_s/C_l$ is the equilibrium partition coefficient. The physical interpretation of the above equation is somewhat different at each interface. Specifically, at the dissolution interface, the feed is dissolved, and the newly melted stoichiometric material dilutes the local tellurium concentration with additional cadmium, forming a diffusion layer that it depleted in tellurium. At the growth interface, excess tellurium is rejected from the newly solidified CdTe, diffusing back into the melt zone and creating a layer that is enriched with tellurium. We note that this boundary condition has been routinely applied at the *growth* interface in most prior models of THM. However, most prior THM models apply different conditions along the *dissolution* interface, which we assert is inappropriate. Only Apanovich and Ljumkis [23] and Lan and Yang [24] openly identify the use of this condition at the dissolution interface.

The tellurium balance represented by the above equation can be further simplified for the case of CdTe growth. First, we consider that the solid feed is stoichiometric CdTe. Next, we consider that the extremely narrow coexistence region on the temperature-composition phase diagram for CdTe makes the assumption of a perfectly vertical solidus curve very reasonable; under this approximation, stoichiometric CdTe is assumed to grow from all liquid compositions. Thus, excess tellurium is exactly zero in both feed and crystal, namely $C_s' = 0$ everywhere. In reality, the solidus curve deviates from stoichiometry at the temperatures employed for THM growth, and the grown crystal

contains an unavoidable amount of excess tellurium. However, the excess mole fraction of Te in the solid is on the order of $C'_s \sim 10^{-4}$, which is sufficiently small to ignore in the analysis of liquid zone composition. As a result, eq. (2.6) can be posed in terms of C' to become

$$\mathcal{D}_l(\mathbf{n} \cdot \nabla C')|_l = -C' \ \mathbf{n} \cdot (v_\mathrm{g}\mathbf{e}_z + \dot{\mathbf{x}}). \tag{2.7}$$

The subscript l has been dropped as the species conservation equations are now only relevant within the liquid domain; henceforth C' represents the excess tellurium in the liquid.

The boundary conditions for the Navier-Stokes equations are found by applying conservation of mass across the growth and dissolution interfaces such that,

$$\left[\rho_l(\mathbf{u}_l - \dot{\mathbf{x}}) - \rho_s(\mathbf{u}_s - \dot{\mathbf{x}})\right] \cdot \mathbf{n} = 0, \tag{2.8}$$

where ρ is the density and $\mathbf{u}$ is the velocity; the subscripts l and s denote the corresponding values on liquid and solid sides of the interface. In the reference frame of the moving heater at steady state, the interface velocity, $\dot{\mathbf{x}}$, is zero but both the feed and growing crystal have velocities equal and opposite to the growth velocity, namely $\mathbf{u}_\mathrm{s} = -v_\mathrm{g}\mathbf{e}_z$. This sets up a downwards flow through the zone that arises from the bulk transport of CdTe from the feed to the growth interface.

The shape and location of both dissolution and growth interfaces must be determined as part of the overall model solution. We require that each interface lie along the composition-dependent melting point of the liquid solution, namely

$$T = T_\mathrm{mp}(C'), \tag{2.9}$$

where $T_\mathrm{mp}(C')$ is determined from the liquidus curve of the phase diagram. This is another important coupling between transport and thermodynamics that strongly affects the behavior of the traveling heater method.

2.2.2 Other boundary conditions

Along the centerline,

$$\left.\frac{\partial T}{\partial r}\right|_{r=0} = \left.\frac{\partial C'}{\partial r}\right|_{r=0} = 0, \tag{2.10}$$

to ensure symmetry in temperature and concentration fields and

$$\mathbf{e}_r \cdot \mathbf{T}\big|_{r=0} = 0 \ , \ u_r = 0, \tag{2.11}$$

to ensure a symmetric velocity field. At the inside ampoule wall, the no-slip and no-penetration conditions are satisfied by setting the fluid velocity equal to the translational velocity of the ampoule,

$$\mathbf{u} = -v_{\mathrm{g}}\mathbf{e}_z. \tag{2.12}$$

Between any adjacent domains (other than the dissolution and growth interfaces) i and j, energy is conserved by setting

$$\mathbf{n} \cdot k_{\mathrm{i}} \nabla T\big|_{\mathrm{i}} = \mathbf{n} \cdot k_{\mathrm{j}} \nabla T\big|_{\mathrm{j}}. \tag{2.13}$$

and since for species equations in the melt,

$$\frac{\partial C'}{\partial r} = 0, \tag{2.14}$$

at the inner surface of the ampoule.

2.3 The quasi-steady approximation

We have posed the above conservation equations in a general form that includes time derivatives. However, for the model results presented in this paper, we focus on quasi-steady states in the THM. While such states are argued to exist in Bridgman crystal growth, they only arise in the limit of diffusion controlled growth when compositional changes in the melt are considered [34]. Indeed, the modeling of compositional changes in Bridgman systems, particularly at slow growth rates, almost always requires a fully transient model; see, e.g., [38]. However, the small size of the liquid zone, compared to typical system heights, allows for the compositional field to rather quickly approach a steady-state in the traveling heater method. We describe the THM system via a moving reference frame, such that the heater is stationary and the ampoule is pulled through a static temperature field. This allows the problem to be rigorously posed from a quasi-steady-state perspective, becoming truly steady-state in the limit of an infinitely long ampoule. Thus, all time derivatives in the above equations are set to zero.

An interesting situation arises under the quasi-steady-state assumption. Since all boundary conditions for the species conservation equations are specified in terms of flux conditions that involve spatial derivatives of concentration, the absolute level of concentration is arbitrary to an additive constant and the underlying mathematical formulation is under-specified. To find a relevant solution, either the underlying equations must be posed as a time-dependent problem, as done by Apanovich and Ljumkis [23], or an additional constraint must be applied to set the concentration level.

An appropriate manner for specification of this constraint in a quasi-steady-state model is to argue that, due to the assumption that the solid is perfectly stoichiometric, the amount of excess tellurium in the liquid zone then must remain constant. This can be specified by using an integral constraint,

$$\overline{C}'V = \int_V C' \, \mathrm{d}V \tag{2.15}$$

where $\overline{C}'$ is the average concentration of excess Te in the liquid zone and V is the computed volume of the liquid zone. The quantity $\overline{C}'V$ is known from the amount of excess tellurium originally added to the growth system to produce the liquid zone. The prior models of Chang *et al.* [22], Lan and Yang [24], Martinez-Tomas *et al.* [28], and Dost and Liu [31] explicitly identified the specification of such an integral constraint, while Ghaddar *et al.* [27] and Stelian and Duffar [19] did not. These two models instead relied on the specification of composition at the dissolution interface to set the overall level of excess tellurium in the zone, an expedient that we believe is inappropriate (see also the discussion after eq. 2.6).

2.4 Approximating the traveling heater

We represent the heating of the ampoule via a radiation boundary condition that is specified on the ampoule surface such that

$$-\mathbf{n} \cdot k_a \nabla T|_a = \epsilon_a \sigma \Big(T^4 - T_{\mathrm{f}}^4(z) \Big). \tag{2.16}$$

The left-hand side represents the conductive heat flux at the ampoule surface, and the right-hand side describes the radiative exchange between the ampoule surface and

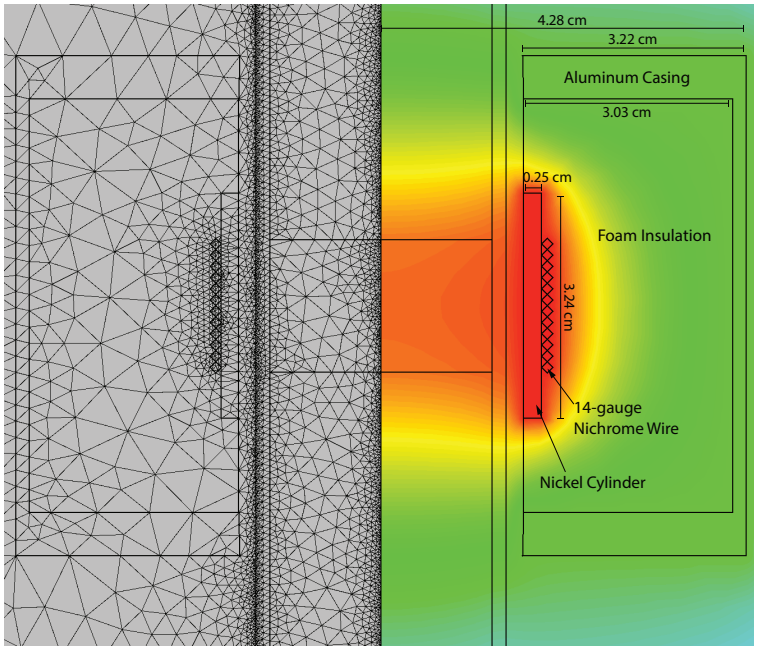

(a)

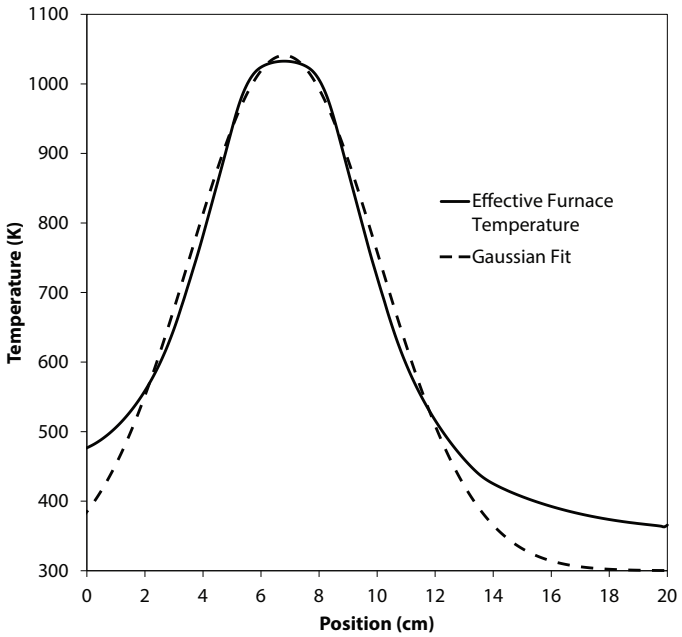

(b)

Figure 2.2: (a) Results from CrysMAS furnace simulations of a hypothetical THM setup. The left side shows the computational mesh used and the right depicts the temperature field with hotter temperatures shown in red. (b) Comparison between the effective furnace temperature calculated from equation 2.18 and a Gaussian temperature profile.

the traveling heater at an effective temperature of T_{f}. The parameters ϵ_a and σ are the emissivity of the ampoule and the Stefan-Boltzmann constant. Near the growth temperatures for this system, typically between 700–1,000 K, we expect that surface heat fluxes will be dominated by radiative transport [39].

To calculate the external heater temperature profile, we employ the CrysMAS code [40, 41] developed by the Fraunhofer Institute for Integrated Systems and Device Technology. A hypothetical design for a THM furnace is depicted in Figure 2.2(a) and consists of a nickel cylinder wrapped in 14-gauge nichrome wire that is then embedded in foam insulation and encased in aluminum. This heater is placed around an ampoule containing a dummy charge with a simple zone shape meant to represent a nominal configuration of the THM, and a heat transfer computation is performed using CrysMAS.

The ampoule surface temperature, $T_a(z)$, and heat flux, $q_a(z)$, are found from the CrysMAS simulation and, rearranging eq. (2.16) with $T_a(z) = T$ and $q_a(z) = -\mathbf{n} \cdot k_a \nabla T|_a$, we obtain:

$$T_{\mathrm{f}}(z) = \left(T_a^4(z) - \frac{q_a(z)}{\epsilon_a \sigma} \right)^{\frac{1}{4}}. \tag{2.17}$$

The value of the effective heater temperature, $T_{\mathrm{f}}(z)$, is plotted as a function of length along the ampoule surface in Figure 2.2(b), and it is also shown to be nicely approximated by a Gaussian function of the form

$$T_{\mathrm{f}}(z) = (T_{\max} - T_0) \exp\left(- \frac{(z-B)^2}{A^2} \right) + T_0. \tag{2.18}$$

Here, $T_{\max}$ sets the maximum value of $T_{\mathrm{f}}(z)$, B is the position of this maximum value, A sets the width of the function, and T_0 sets the minimum value. While the Gaussian curve does differ from the effective furnace temperature farther away from the heater, the goal here is simply to provide a representation of a realistic heater rather than exactly duplicate the thermal environment of a specific heater. This Gaussian fit of the effective furnace temperature is therefore used to represent the furnace in eq. (2.16) in all following calculations.

2.5 System description

In an effort to tie these results to a physical system, geometry of the THM system in these simulations is meant to closely resemble that for CdTe growth deployed in the PHOTON missions [42] performed by collaborator Dr. Professor Michael Fiderle. The ampoule used both in those experiments and the calculations presented here has a diameter of 3.2 cm and is made of 2-mm-thick, graphite-coated quartz. In chapters 4 and 5, an identical system is considered with a 4.8 cm-diameter ampoule to investigate the scaling behaviors associated with flows in the liquid zone.

As described in section 2.4, a Gaussian temperature profile is used to approximate the nominal THM heater via the use of equation 2.18, using the parameters $T_0 = 300$ K, $T_{\max} = 1040$ K, $B = 8.1801$ cm, and $A = 3.266$ cm. The resulting thermal profile is given by the dashed line in Figure 2.2 and produces a thermal gradient of approximately 50 K/cm near the interfaces. While this heater does not necessarily reproduce the exact thermal conditions present in the PHOTON missions, it allows for more flexibility and variability while still remaining an appropriate representation of an realistic system.

The THM process can also be considered a solution growth technique so the amount of tellurium solvent used is an important but sometimes overlooked system parameter. In an experimental system, this would typically be specified as a mass of excess tellurium added as the solvent zone but takes the form of the average mole fraction integral constraint in equation 2.15. As will be shown in chapter 4 and as was shown by Lan *et al.* [24], the size of the liquid zone has a very strong influence on both the strength and structure of the flow. As a base case, we chose the mass of excess tellurium in the 3.2-cm system to be 78.2 g in order to best illustrate the important physics in the system. This produces a liquid zone that is approximately 1.8 cm tall and in the 4.8-cm system, the mass of excess tellurium was chosen to be 176 g to produce a zone of the same height.

2.6 Material properties and uncertainty

The liquidus curve used to determine the composition-dependent melting point in eq. (2.9) is created by fitting data reported by Greenberg [1] and Steininger [43] to

a fourth-degree polynomial of the form,

$$T_{\mathrm{mp}}(C') = a + bC' + cC'^2 + dC'^3 + eC'^4, \tag{2.19}$$

where the the coefficients a, b, c, d, and e are given in Table 2.1.

Material properties of the ampoule, melt, and solid CdTe are listed in table 2.1. While we have some confidence in the properties on the ampoule and solid CdTe, there is considerable uncertainty regarding the properties of the tellurium-rich liquid in the traveling zone. We are not aware of any prior measurements made for liquid mixtures of cadmium and tellurium. However, we believe that its properties are likely quite complicated, based on the behaviors of pure liquid CdTe and Te alone.

Ab inito calculations [52, 53, 54] have shown that, in the stoichiometric limit, liquid CdTe near its melting temperature locally conserves its solid-phase, crystalline, open structure with a coordination number of approximately 4 and, due to this structure, is a semiconductor like its solid phase. In addition, Te atoms have been shown to form extremely long, branched chains in liquid CdTe near the melting point. Thus, liquid CdTe displays a very low thermal conductivity (not much changed from the value of its solid) and a relatively high viscosity [55]. Pure tellurium liquid also exhibits very complicated behavior due to the formation structural features such as rings and chains [56, 51]. For example, these short-range structures have been demonstrated to produce a non-positive thermal expansion coefficient near the melting point [50] as the increasing temperature promotes more efficient packing. Stoichiometric cadmium telluride in the liquid phase also exhibits surprising behavior arising from this short- and long-range ordering [52]. Furthermore, Ko *et al.* [51] predict a density of states that exhibits more metallic character as the tellurium concentration is increased, likely due to the presence of these chain structures.

The effect of this ordering on the thermophysical properties of liquid CdTe has never been investigated however, so we are left to speculate as to what their effect would be. Likely, the liquid phase thermal conductivity is actually much higher than that given here and the thermal expansion coefficient is likely much smaller. However, in lieu of any quantitative measurements or predictions for how these behaviors could affect the properties of a molten tellurium-cadmium mixture, we have estimated the properties of the liquid zone by a linear combination of the values for pure, liquid CdTe

Table 2.1: Physical properties used in the simulations.

Property (units)	**Material**	**Symbol**	**Value**
Thermal Conductivity ($\mathrm{W\,m^{-1}\,K^{-1}}$)	Melt Mixture	k_l	$2.39^{\dagger}$ [44, 45]
	Solid CdTe	k_s	0.907 [44]
	Quartz ampoule	k_a	2.8 [46]
Heat Capacity ($\mathrm{J\,kg^{-1}\,K^{-1}}$)	Melt Mixture	$C_{\mathrm{p},l}$	$250^{\dagger}$ [44, 47]
	Solid CdTe	$C_{\mathrm{p},s}$	159.5 [44]
	Quartz ampoule	$C_{\mathrm{p},a}$	770 [46]
Density ($\mathrm{kg\,m^{-3}}$)	Melt Mixture	ρ_l	5640 [21]
	Solid CdTe	ρ_s	5680 [48]
	Quartz Ampoule	ρ_a	2200 [46]
Thermal Diffusivity ($\mathrm{m^2\,s^{-1}}$)	Melt Mixture	α_l	1.46×10^{-6}
	Solid CdTe	α_s	1.00×10^{-6}
	Quartz Ampoule	α_a	1.65×10^{-6}
Dynamic Viscosity (Pa s)	Melt Mixture	μ	$3.38 \times 10^{-3\dagger}$ [49, 50]
Te Self Diffusivity ($\mathrm{m^2\,s^{-1}}$)	Melt Mixture	$\mathcal{D}$	5×10^{-9} [51]
Thermal Expansion Coefficient ($\mathrm{K^{-1}}$)	Melt Mixture	β_{T}	5×10^{-4} [11]
Solutal Expansion Coefficient*	Melt Mixture	β_{S}	$0.121^{\ddagger}$ [50, 44]
Latent Heat of Fusion ($\mathrm{J\,kg^{-1}\,K^{-1}}$)	CdTe	ΔH_f	210,000 [5]
Emissivity (unitless)	Quartz ampoule	ϵ	1
Melting point polynomial coefficients (K)	Melt Mixture [1, 43]	a	1363.203228
		b	−1070.91350
		c	−1708.508133
		d	12693.04764
		e	−20276.0064

† Properties of the liquid are calculated as a linear combination of the properties of pure tellurium and pure CdTe at 85 mole% Te (and 15 mole% Cd).

* Units are ($[\mathrm{mole\,fraction}]^{-1}$).

‡ This value represents an upper-bound on the solutal expansion coefficient estimated by using the density of liquid tellurium at the melting point of CdTe and the density of liquid CdTe at the same temperature.

and pure, liquid tellurium at the nominal composition of the liquid zone (specifically, a tellurium mole fraction of 0.824 with the balance CdTe). We find that there are not large variations of local composition in the liquid, so we have further assumed that the liquid zone properties are constant. Again, we emphasize that, without more detailed studies on the thermophysical properties of liquid Cd-Te mixtures, it is difficult to assess whether these thermophysical properties are truly representative.

Chapter 3

Numerical method

3.1 Finite Element Approximation

To solve the equations given in chapter 2, the Galerkin finite element method [57] is applied by utilizing the Cats2D code originally developed by Yeckel and Goodwin [58], a code that has been successfully used in the simulation of many different crystal growth systems [59, 38, 60, 61, 62]. What follows is a brief description of the underlying numerical methods that are used to solve these equations. For more information on the specifics of the method employed, the reader is directed to other sources [58, 57] as the following discussion is only intended as an overview.

The first step of the Galerkin Finite Element Method is to discretize each of the field variables, $\mathbf{u}$, p, T, and C' using the finite element basis functions:

$$\begin{aligned}
\mathbf{u} \approx \hat{\mathbf{u}} &= \sum_{k=1}^{N_u} \boldsymbol{u}^k \circ \boldsymbol{\psi}_u^k(\xi,\eta), \\
p \approx \hat{p} &= \sum_{k=1}^{N_p} p^k \phi_p^k(\xi,\eta), \\
T \approx \hat{T} &= \sum_{k=1}^{N_T} T^k \psi_T^k(\xi,\eta), \\
C' \approx \hat{C}' &= \sum_{k=1}^{N_C} C^k \psi_C^k(\xi,\eta)
\end{aligned} \tag{3.1}$$

where the hat symbol above the variables indicates the discretized field variable, N_i

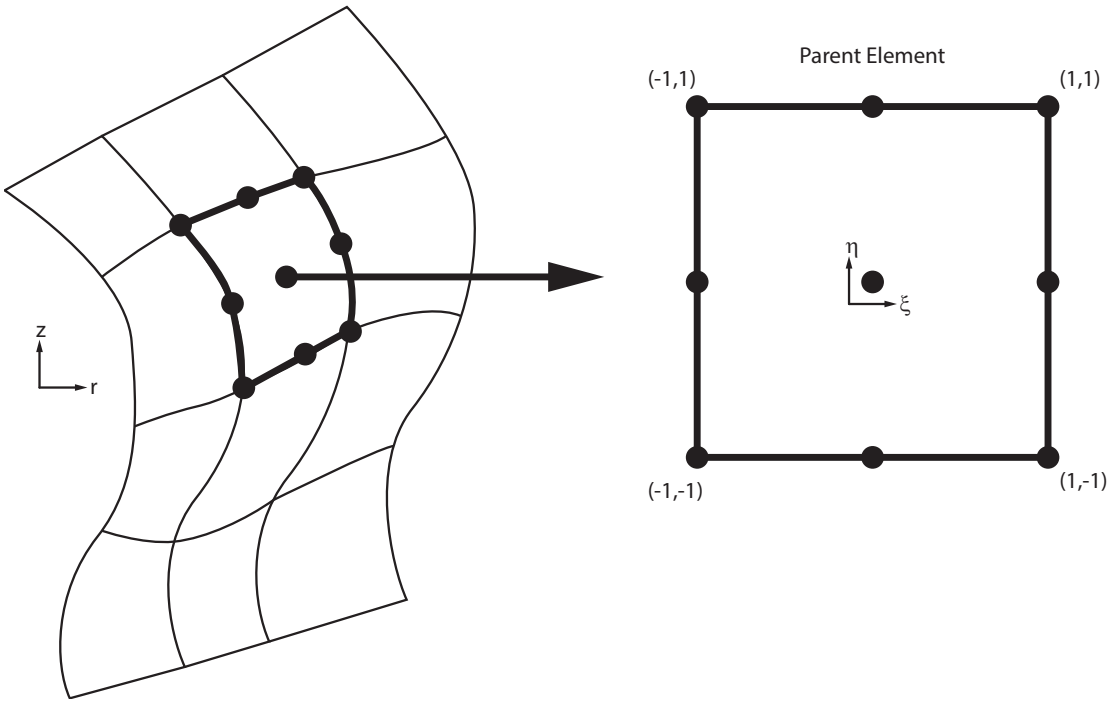

Figure 3.1: Schematic representation of the isoparametric mapping of elements from the r-z coordinate frame onto a parent element defined on the unit square in ξ-η space.

represents the number of nodes defined on a parent element for the field variable i, and where ψ^k and ϕ^k are the Lagrangian basis functions for each node on an element. A different set of basis functions is used for pressure and the other field variables because only certain combinations of velocity and pressure basis functions are numerically stable [57]. In the solution of the THM problem, Lagrangian biquadratic basis functions are used for the field variables while pressure is approximated using discontinuous linear polynomials [57]. Note that the bold-faced $\boldsymbol{\psi}_u$ indicates that the velocity basis function is a vector as well as the velocity coefficients, $\boldsymbol{u}^k$. These two vectors are multiplied element-wise, as indicated by the Hadamard product symbol, $\circ$, to yield the discretized approximation of the velocity vector, $\hat{u}$. This notation is necessary because the weak formulation will yield a gradient of the basis function which must include additional terms in curvilinear coordinate systems.

The variables ξ and η are used through a technique called isoparametric mapping whereby the r and z coordinates for each element in the THM system are mapped to

parent element defined on the unit square as shown in fig 3.1 and mathematically by mapping the coordinates of an arbitrary element using the basis functions:

$$(x, y) = \sum_{k=1}^{N} (x^k, y^k)\psi^k(\xi, \eta). \tag{3.2}$$

Here, (x, y) corresponds to the coordinates of the element itself while x^k and y^k correspond to the nodal coordinates. The variables ξ and η exist on the parent element over the domain $[-1, 1]$ and are the coordinates over which all of the basis functions are defined.

3.2 Elliptic mesh generation

In the travelling heater method, the locations of the growth and dissolution interfaces are not given but are instead determined as part of the numerical solution. A meshing method then is required that allows both fine control over the structure and the freedom to allow the mesh to continuously deform while computing the solutions. To accomplish this, the nodal positions of the rectangular mesh are formulated as an elliptic differential equation that is solved in addition to the field equations described in chapter 2, a technique referred to as elliptic mesh generation. The field equations for mesh motion are

$$\begin{aligned} \nabla \cdot \left(\mathcal{D}_\xi(\xi, \eta)\nabla\xi\right) &= 0, \\ \nabla \cdot \left(\mathcal{D}_\eta(\xi, \eta)\nabla\eta\right) &= 0. \end{aligned} \tag{3.3}$$

The most intuitive understanding of these equations is that they track the diffusion of mesh elements within the larger domain. If the mesh diffusivities are constant, the solution to the mesh equations will tend to produce evenly-spaced elements. In fact, the code actually uses the initial mesh to compute suitable values for $\mathcal{D}_\eta$ and $\mathcal{D}_\xi$ that will duplicate the initial mesh structure even if the mesh nodes start unevenly spaced. For the THM problem, we make use of an initial mesh with a higher concentration of elements around the periphery of the liquid zone (see figure 2.1) in order to accurately compute the concentration within the boundary layer at the edge of the liquid zone.

At all fixed boundaries in the simulation, a boundary condition is used that constrains the nodes to lie along the boundary but does not constrain the absolute positions

of the nodes themselves, allowing them to slide freely along the boundary as the mesh deforms. At the growth and dissolution interfaces, the position of the nodes is coupled with the thermal field through equation 2.9.

3.3 Residual equations

The next step is to formulate residual equations from the field equations referenced in chapter 2, given below:

$$\begin{aligned}
\mathcal{R}_T &= \frac{\partial \hat{T}}{\partial t} + \mathbf{u}\cdot\nabla\hat{T} - \alpha_i\nabla^2\hat{T},\\
\mathcal{R}_u &= \rho_l\Big(\frac{\partial \hat{\mathbf{u}}}{\partial t} + \hat{\mathbf{u}}\cdot\nabla\hat{\mathbf{u}}\Big) - \nabla\cdot\mathbf{T} - \rho_l\mathbf{g}[1+\beta_{\mathrm{T}}(T_0-\hat{T}) + \beta_{\mathrm{S}}(C_0-\hat{C})],\\
\mathcal{R}_C &= \frac{\partial C'}{\partial t} + \mathbf{u}\cdot\nabla C' - \mathcal{D}\nabla^2 C',\\
\mathcal{R}_p &= \nabla\cdot\hat{\mathbf{u}},\\
\mathcal{R}_\xi &= \nabla\cdot\big(\mathcal{D}_\xi(\xi,\eta)\nabla\xi\big),\\
\mathcal{R}_\eta &= \nabla\cdot\big(\mathcal{D}_\eta(\xi,\eta)\nabla\eta\big),
\end{aligned} \tag{3.4}$$

where the subscript i denotes different materials. In order for the approximate solutions to be accurate, these residuals must be minimized both locally and globally. To minimize these residuals, each residual equation is multiplied by a suitable weight and integrated over the entire domain. In fact, the key to the Galerkin finite element method is that the weighting function is chosen to be the basis function used to approximate the solution in equation 3.1, i.e.,

$$\begin{aligned}
&\int_V \phi_T^{k^*}\mathcal{R}_T(\phi_T^{n^*})\,\mathbf{d}V = 0, \quad \int_V \boldsymbol{\phi}_u^{k^*}\mathcal{R}_u(\boldsymbol{\phi}_u^{n^*})\,\mathbf{d}V = \ 0, \quad \int_V \phi_C^{k^*}\mathcal{R}_C(\phi_C^{n^*})\,\mathbf{d}V = 0,\\
&\int_V \psi_p^{k^*}\mathcal{R}_p(\psi_p^{n^*})\,\mathbf{d}V = 0, \quad \int_V \phi^{k^*}\mathcal{R}_\xi(\phi^{n^*})\,\mathbf{d}V = \ 0, \quad \int_V \phi^{k^*}\mathcal{R}_\eta(\phi^{n^*})\,\mathbf{d}V = 0,
\end{aligned} \tag{3.5}$$

where the index k^* refers to the global index over all elements rather than simply the local index on a given element. Each of these residual equations is in fact an inner product between the basis function and the residual so we could reframe the problem by saying that we seek a solution to the residual equations such that they are orthogonal to the basis functions. This property is called Galerkin orthogonality and is at the

heart of the finite element method. The reader should also remember that each residual equation is in fact a function of the basis functions as well, which is indicated by the n^* index. This index is separate from k^* although each still represents a loop over all nodes in the mesh; n^* corresponds to the basis functions used to approximate the solution (also called test functions) which represents a different set than the Galerkin weighting functions (also called trial functions). The solution to these residual integrals is the so-called "weak" solution because a larger function space can be used to satisfy the equation than for the original residual equations. These integrals will eventually be referred to as the "weak formulations" of the residual equations once all second derivatives have been transformed into first derivatives.

At this point, we can use the chain rule to rewrite all second-order terms in the form

$$\phi\nabla^2 b = \nabla\cdot\phi\nabla b - \nabla\phi\cdot\nabla b, \tag{3.6}$$

where b is a generic variable. To transform these terms from second-order to first-order, we can make use of the Gauss divergence theorem,

$$\int_V \nabla\cdot\phi\nabla b\,\mathrm{d}V = \int_A \psi\mathbf{n}\cdot\nabla b\,\mathrm{d}A, \tag{3.7}$$

also thereby converting these volume integrals into surface integrals over the area A with unit normal vector, $\mathbf{n}$. A discussion for exactly *why* we need to reduce the equations from second-order to first-order requires a more careful understanding of the mathematical vector spaces to which these functions belong [57] and is omitted here. After these

manipulations, the residual equations become

$$\begin{aligned}
\int_V \phi_T^{k^*}\Big(\frac{\partial \hat{T}}{\partial t} + \hat{\mathbf{u}}\cdot\nabla\hat{T}\Big)\,\mathrm{d}V + \int_V \alpha_i \nabla\phi_T^{k^*}\cdot\nabla\hat{T}\,\mathrm{d}V + \int_A \alpha_i \phi_T^{k^*}\mathbf{n}\cdot\nabla\hat{T}\,\mathrm{d}A = 0,\\
\int_V \boldsymbol{\phi}_u^{k^*}\circ\rho_l\Big(\frac{\partial\hat{\mathbf{u}}}{\partial t} + \hat{\mathbf{u}}\cdot\nabla\hat{\mathbf{u}}\mathbf{g}[1+\beta_{\mathrm{T}}(T_0-\hat{T})+\beta_{\mathrm{S}}(C_0-\hat{C})]\Big)\\
+\int_V(\nabla\circ\boldsymbol{\phi}_u^{k^*})\cdot\mathbf{T}\,\mathrm{d}V - \int_A \boldsymbol{\phi}_u^{k^*}\circ\mathbf{n}\cdot\mathbf{T}\,\mathrm{d}A = 0,\\
\int_V \psi_p^{k^*}\nabla\cdot\hat{\mathbf{u}}\,\mathbf{d}V = 0,\\
\int_V \phi_C^{k^*}\Big(\frac{\partial\hat{C}'}{\partial t} + \hat{\mathbf{u}}\cdot\nabla\hat{C}'\Big)\,\mathrm{d}V + \int_V \mathcal{D}\nabla\phi_C^{k^*}\cdot\nabla\hat{C}'\,\mathrm{d}V + \int_A \mathcal{D}\phi_C^{k^*}\mathbf{n}\cdot\nabla\hat{C}'\,\mathrm{d}A = 0,\\
\int_V \mathcal{D}_\xi\nabla\psi^{k^*}\cdot\nabla\xi\,\mathrm{d}V - \int_A \psi^{k^*}\mathcal{D}_\xi\mathbf{n}\cdot\nabla\xi\,\mathrm{d}A = 0,\\
\int_V \mathcal{D}_\eta\nabla\psi^{k^*}\cdot\nabla\eta\,\mathrm{d}V - \int_A \psi^{k^*}\mathcal{D}_\eta\mathbf{n}\cdot\nabla\eta\,\mathrm{d}A = 0.
\end{aligned} \tag{3.8}$$

In the Cats2D code, these residuals are further manipulated to be solved in an arbitrary Lagrangian-Eulerian (ALE) frame of reference, but as this is only needed when solving transient problems with a moving mesh, the discussion is omitted here. Additionally, the mesh governing equations as currently written map to a $\xi(x,y)$-$\eta(x,y)$ space whereas to be useful, these must be remapped back into the $x(\xi,\eta)$-$y(\xi,\eta)$ coordinate space. While an important step, this too is omitted for this discussion and instead the reader is referred either to [57] or [58] for detailed information.

3.4 Application of boundary conditions

The boundary conditions introduced in chapter 2 can be broadly sorted into three types of boundary conditions: Dirichlet-type, where the value of a field variable is set at a boundary; flux-type, where the first derivative of a field variable is specified (possibly as a function of the field variable); and constraint-type where the boundary condition is required to couple physics together. Dirichlet conditions are implemented in the finite element method by directly substituting the residual at the boundary with the value of

the field variable to be imposed.

Some of the flux-type boundary conditions actually arise naturally in the Galerkin finite element formulation of the problem during the integration by parts and are called "natural" boundary conditions. These are the area integrals in equation 3.8 which are all functions of a gradient in the field variable; in the case of the energy residual for example, this involves a $\mathbf{n} \cdot \nabla \hat{T}$ term. For the residuals to approach zero, this naturally requires that the gradient term also go to zero and so the natural boundary condition for most residuals requires that the flux be zero at the boundary. Alternatively, if the flux is non-zero at the boundary, one may simply replace the area term with the suitable weak formulation of the flux boundary condition. Particular attention should be paid to the momentum residual as it is formulated here in the so-called stress-divergence weak formulation. Importantly, the natural boundary condition takes a slightly different form than what one would expect given the natural boundary conditions for the other field variables. Here the area integral contains the term $\mathbf{n} \cdot \mathbf{T}$, which, while technically a flux term, is better understood as requiring that the net force on a boundary be equal to zero. As a result, boundary conditions for the Navier-Stokes equations must be specified as either a force or a velocity in this formulation.

The constraint-type boundary conditions are ones that are not actually boundary conditions on the field variables themselves but rather couple the solution of the field variables to the behavior of the mesh. In this problem, the condition that the phase boundaries lie at the composition-dependent melting point is applied as a constraint condition. This is accomplished by replacing a residual equation at a node requiring that the boundary position satisfies the constraint condition. In other problems, the constraint-type boundary condition could be used to specify the position of a fluid boundary given the forces in the system.

3.5 Solution method

The above non-linear residual equations are assembled into a residual vector, $\mathbf{r}(\mathbf{z}) = 0$, that is a function of $\mathbf{z}$ unknowns. This non-linear system is solved using the Newton-Raphson method whereby a new solution vector is given by,

$$\mathbf{z}^{i+1} = \mathbf{z}^{i} + f\delta. \tag{3.9}$$

Here the index $i+1$ represents the next iteration, and f is a dampening factor. The solution update vector, δ, satisfies the linear system,

$$\mathbf{J}\delta = -\mathbf{r}, \tag{3.10}$$

where

$$\mathbf{J} \equiv \frac{\partial \mathbf{r}}{\partial \mathbf{z}} \tag{3.11}$$

is the Jacobian matrix.

This linear problem is then solved using Gaussian-Elimination and iterations are performed until the L2 norms of both the residual vector, $\mathbf{r}$, and the solution update vector, δ, are less than 0.01% of the L2 norm of the solution vector. The L2 norm of a vector quantity, $\boldsymbol{x}$ is given by

$$||\boldsymbol{x}||_{\mathrm{L2}} \equiv \sqrt{\sum_{k=1}^{N} |x_k|^2} \tag{3.12}$$

where all components of the vector, x_k are squared and summed together. Often however, it is not necessary to recompute the Jacobian at every Newton iteration, so a single Jacobian may be reused for several iterations as long as both the norms of residual and solution change continue to decrease.

Newton's method displays quadratic convergence when the initial guess is sufficiently close to the actual solution, but often the issue is in simply being close enough to the solution for Newton's method to converge. As a result, a first-order continuation method is used to traverse solution space so that any initial guess for a solution is very close to the actual solution. Starting from a converged solution, $\mathbf{z}$, the solution at a new parameter, $P + \Delta P$, can be approximated as

$$\mathbf{z}(P + \Delta P) \approx \mathbf{z}(P) + \Delta P \frac{\partial \mathbf{z}}{\partial P}, \tag{3.13}$$

where ΔP is some change in a solution parameter, P. By using this approximation as an initial guess for a Newton iteration at the new parameter value of $P + \Delta P$, steady-state solution space can be traversed through continuation in various solution parameters.

Arriving at a final converged solution in the THM problem is a multi-step process whereby successively more complicated problems are solved until all physics are introduced. The first step is to solve the linear heat transfer problem without the effects of

flow or concentration on a fixed mesh. Rather than introducing physics later, we may instead solve the heat transfer problem with trivial constant solutions to the velocity and composition fields by recognizing the coupling forces between the equations. For example, the driving force for flow is solutal and thermal buoyancy effects so by setting gravity to zero, one may compute a quiescent flow field very easily. Similarly, the driving force for solutal gradients is the process of growth so by setting the translation rate of the furnace to zero, the concentration field should be constant. However, the non-linearity of the radiation heat transfer boundary condition can still present a problem for Newton's method when there is no suitable initial guess. Nonetheless, it is very easy to simply reduce the boundary condition from a function of T^4 to a function of T and instead solve this linear problem. Then, that solution provides a very useful initial guess for the non-linear heat transfer problem.

In order, the continuation scheme is as follows:

- Solve the linear heat transfer problem on a fixed mesh problem by reducing all T^4 powers to T.
- Solve the non-linear heat transfer problem with the T^4 dependence reintroduced. The mesh is still fixed.
- Allow the mesh to deform in order to satisfy the condition that the temperature at a phase change interface be equal to the local melting point. Depending on the thermal field, the initial position of the interfaces, and the degree of deflection of the interface, it may be necessary to reduce the dampening factor, f, in Newton's method to ensure that the mesh does not move too far between successive iterations.
- Introduce flow by using first-order continuation to increase the level of gravity in the system.
- Use first order continuation to continue in the heater translation rate. Because the problem is posed in a translating frame of reference, this continuation step actually involves setting the translation velocities of the crystal, feed, and ampoule.

Since growth and flow are the most non-linear aspects of the system, it is best that they are introduced last. Since growth is connected to all three field variables through

segregation, latent heat, and continuity, its effects are complicated and is best left until last during the continuation scheme. It should also be noted that due to the non-linearity of the system, solution existence is never guaranteed. Furthermore, bifurcations and solution turning points may exist that prevent the first-order continuation method from succeeding in a certain parameter regime. These issues however, are beyond the scope of this thesis and for the parameters presented here, first order continuation was sufficient to reach a converged steady-state solution.

Chapter 4

Effect of gravity and zone size

4.1 Behavior without flow

It is quite instructive to consider the THM steady state under conditions without buoyancy-driven flow in the zone, such as would arise in the absence of gravitational forces. This state is achieved by setting all terms involving gravity in eq. (2.4) to zero and is shown in Figure 4.1. For this case, we consider an ampoule inner diameter of 3.2 cm and a zone translation rate of $v_g = 2.49$ mm/day.

Note that this and all successive figures show the geometry of liquid zone, with the dissolution interface and solid feed above and the growth interface and crystal below. Two images are typically used for each case to show the compositional field and flow streamlines through the liquid zone (on the left-hand side of the left and right image, respectively) and the thermal field throughout the different domains (on the right-hand side of both images). Concentration contours are spaced equally between C'_{min} and C'_{max}, which represent the minimum and maximum values of excess tellurium mole fraction in the liquid zone (see also the explanation of C' in Section 2.1). The liquid flow in the zone is everywhere tangent to the streamlines, which are contours of ψ, the Stokes streamfunction [63], and plotted with constant spacing. The rotational sense of a vortex is given by the sign of the streamfunction, with negative indicating clockwise and positive indicating counter-clockwise flow. The absolute values of the extrema, ψ_{min} and ψ_{max}, are proportional to the volume of fluid recirculation, thus indicating overall flow strength.

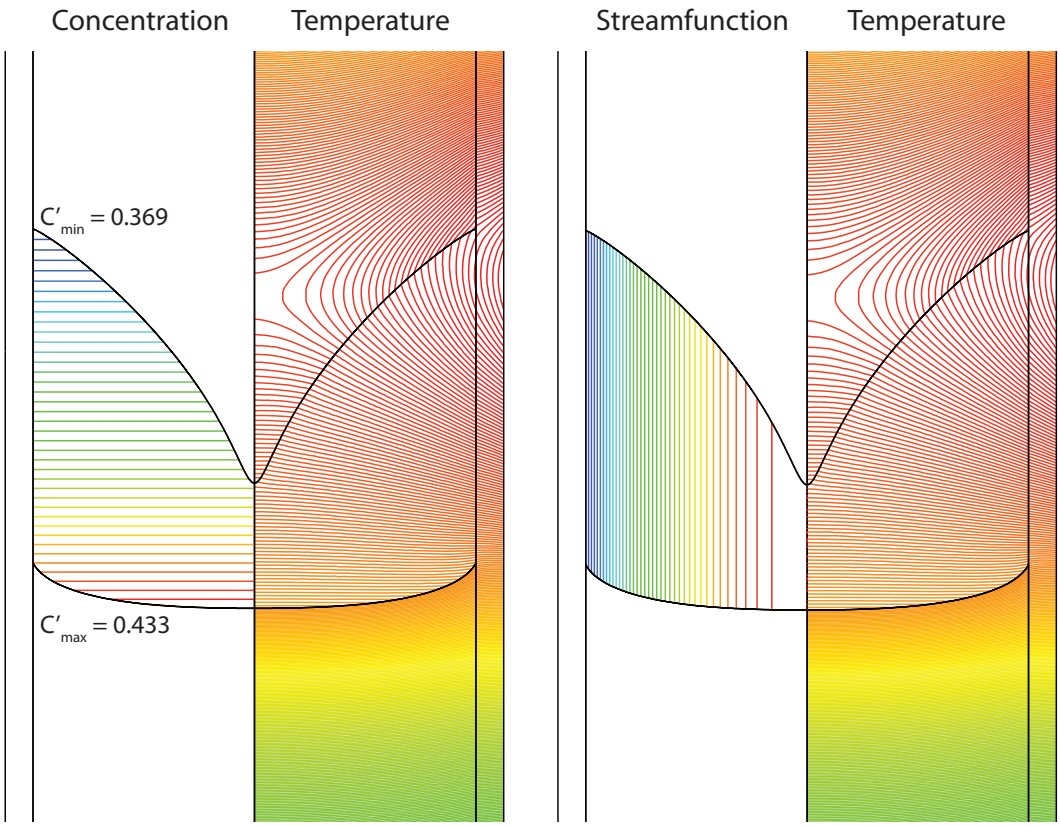

Figure 4.1: Contour plots showing two views of the melt zone and surrounding solid regions for growth at 2.49 mm/day in a 3.2-cm diameter ampoule without buoyancy effects (computed by setting $g = 0$). The spacing between isotherms is 1.16 K, and the maximum temperature is 1005 K.

Without buoyancy, the flow in the liquid arises due to zone motion and is constant in the axial direction. This is demonstrated by the straight, vertical streamlines in the image on the right. Their nonuniform radial spacing arises from the underlying cylindrical geometry and the property that the volumetric fluid flow is constant between successive streamlines plotted with a constant interval. The equally incremented streamlines are thus spaced so that the circular annuli between successive streamlines have constant areas.

The steady movement of the zone drives constant dissolution and growth. Excess tellurium is rejected at the growth interface, while there is a depletion layer at the dissolution interface caused by dilution. Diffusion transports excess tellurium upward across the zone, being driven by the difference between higher and lower tellurium concentrations at the interfaces. Note that in the absence of any convection, the iso-concentration contours are perfectly horizontal and equally spaced, indicating a concentration profile that is perfectly one-dimensional and linear in the axial direction.

Heat is transported into the system via radiation from the surrounding heater, and the maximum temperature is located on the outer ampoule wall slightly below the outer position of the dissolution interface. The thermal field is entirely determined by heat conduction through the domains, and, since heat flows normal to the shape of the isotherms, one observes an inward heat flux turning upward and downward to flow to cooler temperatures.

The shapes of the solid-liquid interfaces are very different for this case. First, we remark that the effect of latent heat release at the growth and dissolution interfaces is minimal for this system in general. One can anticipate this outcome from a scaling argument that provides an estimate of the importance of latent heat to the underlying conductive heat fluxes at the interface via the product of a Peclet number, $\mathrm{Pe_g} = Lv_\mathrm{g}\rho_l C_{\mathrm{p},l}/k_l$, multiplied by a Stefan number, $\mathrm{St} = \Delta H_f/\Delta T C_{\mathrm{p,l}}$, two dimensionless groups that arise naturally from nondimensionalization of eq. (2.5). For the conditions here, $v_\mathrm{g} = 2.49$ mm/day and $\Delta T/L \approx 50$ K/cm, leading to $\mathrm{Pe\ St} \approx 10^{-3}$, indicating that latent heat does not measurably affect the shapes of either interface.

Rather, the shapes of these interfaces are determined by the interplay between heat and mass transport and thermodynamics. The shape of the lower, growth interface is slightly concave with respect to the crystal. At the bottom of the zone, heat flows are

primarily in the axial direction, but the mismatch between the thermal conductivities of the liquid, solid, and ampoule cause the interface to slope upward at the inner ampoule wall, a classical example of the "interface effect" first discussed by Jasinski and Witt [64]. In addition, since there is a small heat flux leaving the system in the radial direction, the outer portion of the liquid zone is cooler than the inner. The interaction of this temperature field with the rejected, upward-diffusing tellurium leads to an interface whose position is determined by both local composition and temperature (via the liquidus relation of the phase diagram). Note that the growth interface is neither an isotherm nor a surface of constant composition.

The coupling between transport and thermodynamics is dramatically stronger for the dissolution interface in this case. In the upper portion of the zone, the heat flux from the traveling heater is turning from inward to downward, leading to a strongly two-dimensional temperature field. The axially linear tellurium concentration profile in the zone then pulls the interface location downward in the direction of the changing heat fluxes. The outcome is the strikingly convex dissolution interface. At slightly higher growth rates (not shown), the increased tellurium segregation drives the dissolution interface further downward until it meets the growth interface, representing the maximum growth rate in zero gravity. Qualitatively, these results agree remarkably well with the prior computations by Lan and Yang [24], where a similar effect is seen for cases under microgravity with small solvent volumes.

4.2 Effect of buoyant flow

Flows in the liquid zone, driven by buoyancy, can strongly influence system behavior. We can estimate the effects of this flow on heat and mass transport via thermal and solutal Peclet numbers, defined as

$$\mathrm{Pe}_T = \frac{v_{\max} R}{\alpha_l}, \tag{4.1}$$

$$\mathrm{Pe}_s = \frac{v_{\max} R}{\mathcal{D}_l}, \tag{4.2}$$

respectively, where $v_{\max}$ is the maximum velocity of the flow in the zone. These Peclet numbers represent the relative importance of convective to diffusive transport [39, 65]. To illustrate and explain these effects in THM growth, we consider a 3.2 cm-diameter

ampoule with a zone translation rate of $v_g = 1.24$ mm/day submitted to various levels of gravitational acceleration.

Figure 4.2(a) shows the system under 0.01% of the full, terrestrial gravity level (in this and all subsequent cases, gravitation is directed downward in the axial direction). The flow in the liquid zone is characterized by a single, toroidal vortex, with warmer, less dense liquid flowing upward along the ampoule wall and cooler, more dense liquid flowing downward along the centerline. While the effect of this flow on heat transfer and the temperature field in the system is quite small, with $\mathrm{Pe}_T \approx 0.3$, its impact on solute transport is significant, as indicated by the deflected iso-concentration contours in the figure and the value of $\mathrm{Pe}_s \approx 90$. The rearrangement of the compositional field in the zone dramatically changes the interface shapes, compared to those exhibited in the zero-gravity case shown in Figure 4.1, due to the strong dependence of melting point on tellurium concentration.

At 1% of full gravity, the flow structure retains its single vortex form, as shown in Figure 4.2(b); however, the flow is much stronger, with calculated values of $\mathrm{Pe}_T \approx 20$ and $\mathrm{Pe}_s \approx 6 \times 10^3$. The stronger flow convects more heat toward the growth interface, flattening it compared to the prior case shown in Figure 4.2(a). The tellurium contours are even more deflected by the flow, leading to nearly uniform composition through much of the zone and boundary layers at the dissolution and growth interfaces. Compared to prior cases, there is less variation of composition and temperature along the interfaces.

Figure 4.2(c) shows the system under full gravity. While the maximum liquid velocity is only 14% larger than the prior case (leading to $\mathrm{Pe}_T \approx 24$ and $\mathrm{Pe}_s \approx 6.9 \times 10^3$), its form has dramatically changed to a multiple-cell structure with one primary vortex and two weaker, counter-rotating flow cells. The primary vortex convects even more heat toward the growth interface, deflecting it further downward. Neither of the two counter-rotating cells is strong enough to locally alter the temperature field; however, both significantly impact the local composition. As will be discussed in chapter 5, the weak vortex near the growth interface has an out-sized effect on the nature of the growth interface.

We can characterize the strength of the flow in the THM zone via a dimensionless Reynolds number,

$$\mathrm{Re} = \frac{\rho_l v_{\max} R}{\mu}, \tag{4.3}$$

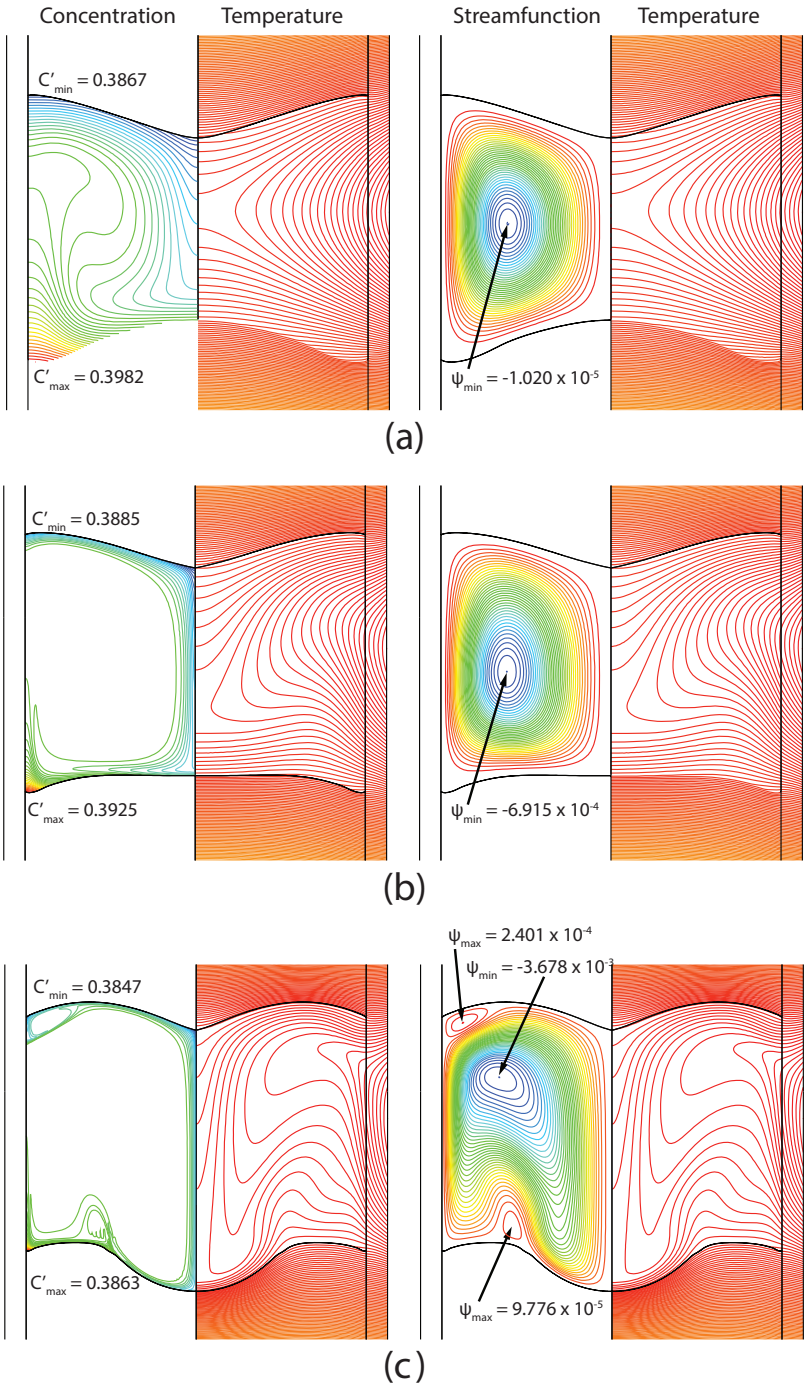

Figure 4.2: Contour plots showing the effect of increasing buoyant forces at a growth rate of 1.24 mm/day in a 3.2-cm ampoule, for gravity levels of (a) 0.01% g, (b) 1% g, and (c) full gravity. The spacing between isotherms in each figure is 1.16 K, and the maximum temperature in each figure is approximately 1000 K. Negative streamfunction values denote clockwise rotation, and positive values denote anti-clockwise rotation.

and the thermal buoyant driving force via the dimensionless Grashof number,

$$\mathrm{Gr} = \frac{\rho_l^2 g \beta_\mathrm{T} \Delta T R^3}{\mu^2}, \tag{4.4}$$

where ΔT is calculated as the maximum temperature difference across the liquid zone. Using a balance of dominant terms in the dimensionless form of the Navier-Stokes equations [65], we expect that $\mathrm{Re} \propto \mathrm{Gr}$ when viscous forces dominate the flow and that $\mathrm{Re} \propto \mathrm{Gr}^{1/2}$ when inertia dominates.

Figure 4.3 presents a log-log plot of Reynolds number versus Grashof number, computed for two THM systems under various levels of gravity. One curve shows the behavior of the 3.2 cm-diameter system considered thus far in this thesis, and the other corresponds to an identical system but with an ampoule inner diameter of 4.2 cm. Both systems clearly show the expected, universal scaling behavior discussed above, with a transition from viscous to inertial flows occurring as the Reynolds number increases from approximately 10 to 100. Further, we also see that the 3.2-cm and 4.8-cm systems are similar when their Grashof numbers are comparable. This will be further discussed in the next section.

Buoyant flows may also arise from density differences due to solutal effects, which can be characterized by a solutal Grashof number,

$$\mathrm{Gr}_s = \frac{\rho_l^2 g \beta_\mathrm{S} \Delta C' R^3}{\mu^2}, \tag{4.5}$$

where β_S is the volumetric expansion coefficient arising from composition and $\Delta C'$ represents the maximum concentration difference across the liquid zone. At full gravity, we calculate $\mathrm{Gr} = 1.5 \times 10^6$ and $\mathrm{Gr}_s = 1.9 \times 10^4$, indicating that solutal buoyancy is far less important than thermal buoyant effects. Indeed, we find that, after removing solutal buoyancy entirely from our computation, changes to the flow structure and interface shapes were almost imperceptible.

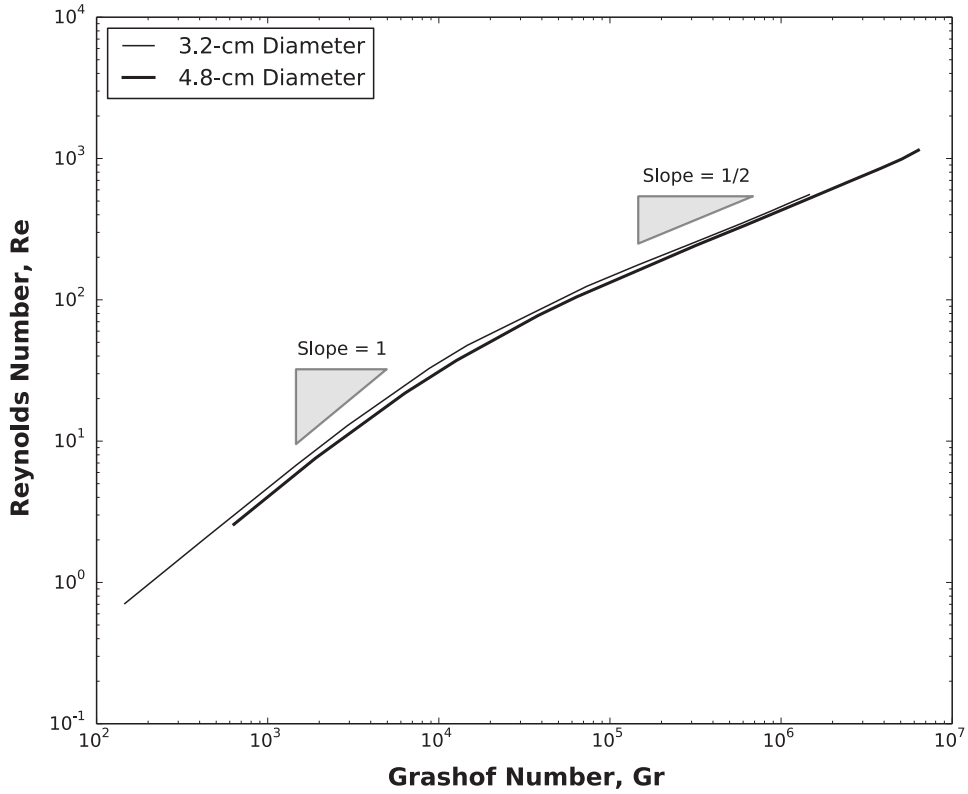

Figure 4.3: Two scaling regimes are demonstrated by Reynolds number plotted against the Grashof number for ampoules of 3.2-cm and 4.8-cm diameters. The dimensionless Reynolds and Grashof numbers are calculated from eqs. (4.3) and (4.4), respectively.

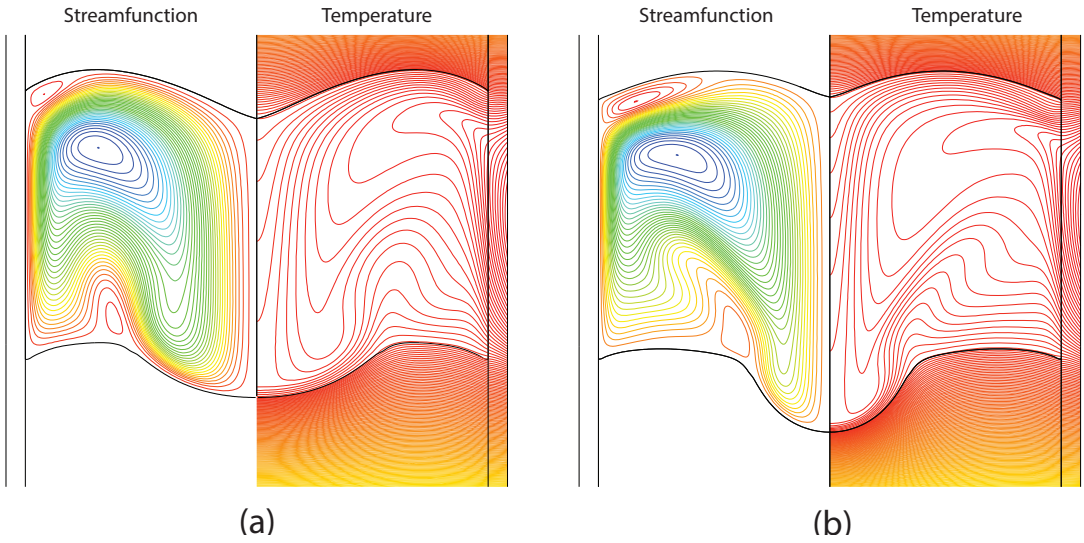

Figure 4.4: Contour plots of streamlines and isotherms in the 4.8-cm ampoule at a growth rate of 0.90 mm/day for gravity levels of (a) 40% gravity and (b) full gravity. The flow pattern in (a) is very similar to that in the 3.2-cm ampoule at full gravity.

4.3 Influence of zone size and ampoule radius

4.3.1 Influence of ampoule radius

Additional calculations were performed in an ampoule with a diameter of 4.8 cm and showed flow structures very similar to those in the 3.2-cm ampoule. As in the buoyancy-free calculations performed for the 3.2-cm ampoule, the maximum growth rate in zero gravity was first found to be approximately 1.9 mm/day again limited by the formation of a solid core. In order to compare the two systems, this growth rate was once again halved before slowly increasing the gravity level.

A key result shown in figure 4.3 is that the scaling relationship between the Reynolds and Grashof numbers is largely independent of ampoule radius for the flows shown here. For comparison, the flow structures in the 4.8-cm ampoule 40% gravity and full gravity are shown in figure 4.4. At 40 % gravity, the flow pattern in the larger ampoule closely resembles that in the smaller ampoule at full gravity while the Grashof numbers in both systems are similar at 2.54×10^6 and 1.46×10^6 respectively. Therefore as a first approximation, one may predict the effects of changing the ampoule size by looking

at systems with a similar Grashof number and zone height. With a smaller ampoule, the viscous effects become more dominant as indicated by the Grashof number which scales with the length scale cubed, i.e $\mathrm{Gr} \sim r^3$. Since the Grashof scales so strongly with radius, the effect of a small increase in radius is enough to drive much stronger flows. Indeed, we have found that we are unable to compute steady state solutions for the 4.8-cm ampoule under certain parameter regimes and we believe that this indicates that the solution has become time dependent or is approaching a bifurcation.

4.3.2 Influence of zone length

The amount of excess tellurium used as a solvent directly translates into a specific zone size and shape given a particular heating profile. Again, as the Grashof number scales with the length scale cubed, increasing either the size of the liquid zone or the radius will greatly increase the Grashof number and the driving force for flow. The evolution of the system for increasing tellurium solvent at zero growth rate is shown in figure 4.5 with the amount of tellurium solvent varying from (a), 43.5 g, to (f), 91.7 g. We have found that the existence of steady state solutions at a specific growth rate is not guaranteed for all zone sizes and so, for comparison's sake, we have chosen to use a growth rate of zero. Additionally, this simplifies the comparison by removing any solutal effects. Each image represents a solution that was produced by continuing in the constraint parameter from equation 2.15 using a first-order continuation scheme.

With only 43.5 g in figure 4.5 (a), there is barely enough tellurium in the system to keep a solid core from forming at the centerline. As the mass of excess tellurium is increased to 50.8 g in figure 4.5 (b), the stronger flow at the centerline flattens the growth interface just as it did when the strength of gravity was increased in section 4.2. In contrast to figure 4.2 though, there are areas where the interface is locally concave even though the overall shape of the interface is generally convex. At 58.6 g of excess tellurium, the growth interface has become mostly concave again due to the strong flow at the centerline.

Up until this point, the primary flow cell has dominated the flow structure but with 70.4 g of excess tellurium, the secondary flow cells now begin to rapidly increase in strength. The upper corner vortex has increased in strength fully eight times between figures 4.5 (c) and (d) and a new vortex has formed at the growth interface. The vortex

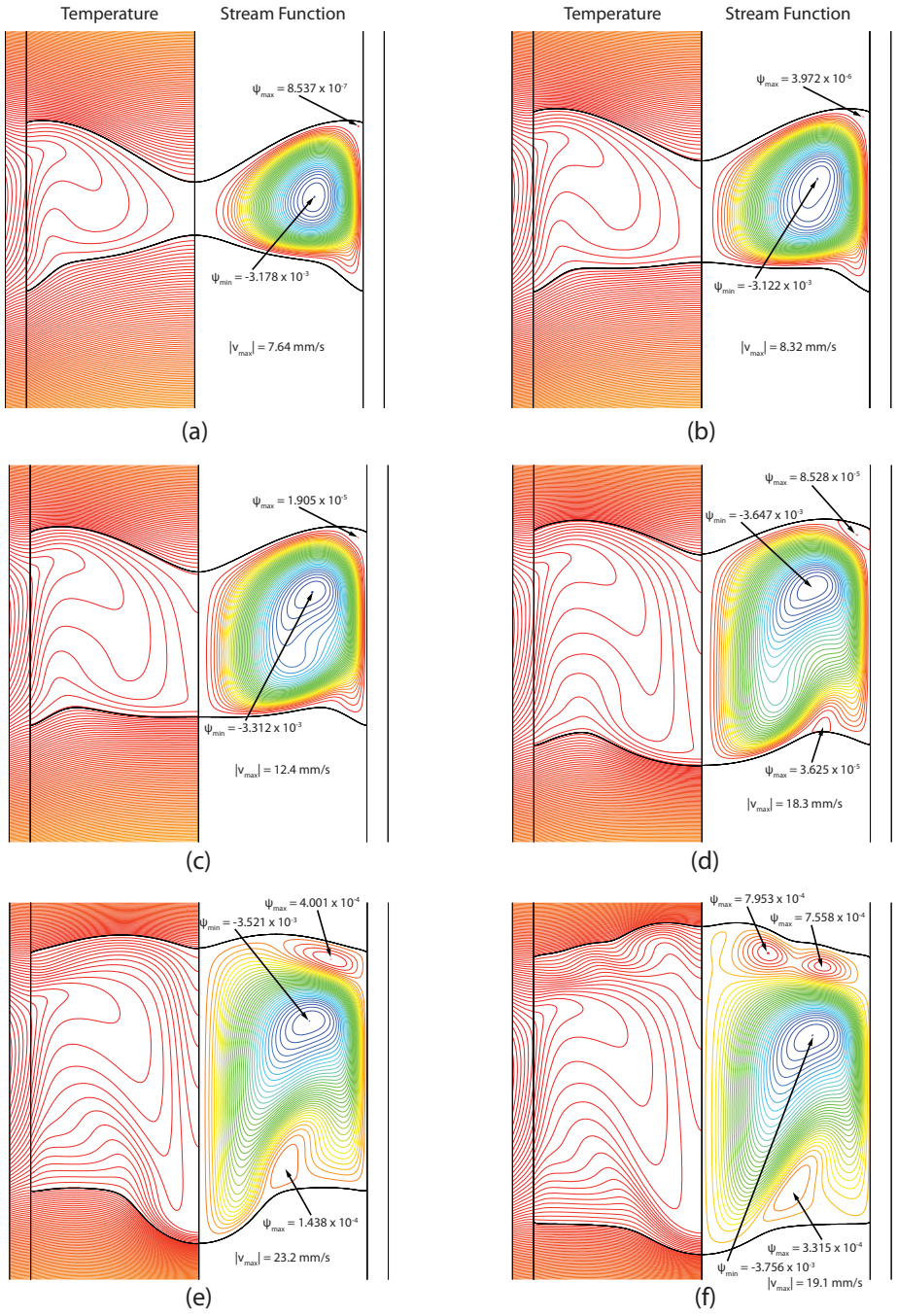

Figure 4.5: Contour plots of streamlines and isotherms in the 3.8-cm ampoule for excess tellurium masses of (a) 43.5 g, (b) 50.8 g, (c), 58.6 g, (d) 70.4 g, (e) 82.1 g, (f) 91.7 g. Streamfunction extrema are indicated within each figure along with the maximum fluid speed.

at the dissolution interface resembles a classic Moffatt eddy [66] but since this vortex exists in an unstable portion of the melt (i.e. one where a cold fluid lies on top of a hotter fluid), the eddy quickly gains strength as the zone size is increased. Again, the vortex at the growth interface turns out to be crucial to understanding the growth rate limits in the THM system and will be discussed extensively in chapter 5.

Increasing excess tellurium to 82.1 g and 91.7 g in figures 4.5 (e) and (f) show that the secondary vortices grow in strength much faster than the primary vortex. At 82.1 g, the top vortex has flattened as its strength has increased by a factor of five in the presence of a large unstable temperature field. Beyond this, the top vortex splits into multiple convective cells that occupy the space above the primary vortex. We were actually unable to simulate any systems beyond 91.7 g of excess tellurium and we believe this is due to a loss of steady state solution existence. We believe these flow cells will become increasingly time-dependent as the driving force for flow increases and the system becomes increasingly non-linear. Stellian and Duffar [19] also simulated a 3.2-cm ampoule and managed to show calculations for longer zones but only by calculating a long-time transient state rather than a true steady state.

The maximum flow speed in the melt zone has also been indicated in each system shown in figure 4.5 and interestingly, it does not obey the $\mathrm{Re} \sim \mathrm{Gr}^{1/2}$ scaling observed in section 4.2. Up until a mass of 78.2 g of tellurium, the vortex at the dissolution interface is fairly weak and the fastest portion of the flow remains at the centerline. However, as the mass of excess tellurium is increased, this vortex becomes stronger and fastest area of the flow shifts upward. Between 82.1 g and 91.7 g, the maximum speed of the melt actually *decreases* as the top vortex splits into two. Even though the streamfunction indicates that these vortices have increased in strength, the reader must remember that the streamfunction represents a volumetric flow rate and not a linear velocity. So while the vortices increase in size, they may not increase in speed as the zone size becomes larger and the flow is less directed.

4.4 Conclusions

We have presented a comprehensive mathematical and computational model for the growth of cadmium telluride by the traveling heater method. While previous models for

the THM have been put forth, we argue that most are inconsistent in the representation of local thermodynamic equilibrium conditions at the dissolution interface and steady-state operation, save for that of Lan and Yang [24]. We have demonstrated the strong interplay among thermal, solutal, and flow effects in the THM, as coupled through the liquidus curve of the phase diagram. We have shown that, under terrestrial conditions, fluid flow in the relatively small liquid zone is strong enough to give rise to complicated flow structures.

When simulating crystal growth on the continuum scale, we are unable to directly predict crystal quality as we are not modelling the phase change explicitly. However, we can still infer aspects of crystal quality by analyzing the conditions under which the crystal is forming. In this chapter, the main tool we have to assess crystal quality is the growth interface shape. The way that the growth interface influences crystal quality is discussed in more detail in chapter 6, but for our purposes here, we simply say that a convex interface is likely to yield a higher quality crystal by concentrating defects at the periphery. However, our results show that the classification of an interface as either "convex" or "concave" isn't as straightforward as it tends to be in Bridgman systems. The strong flows in the THM system drive large heat fluxes that tend to create a highly concave center to an interface that is actually convex on the outer edges. The implications for crystal quality are far from certain.

Communications from collaborators and contacts in the CZT industry have overall been skeptical of this interface shape. While the true interface shape has not been observed in experimental systems, they infer the shape from the striations and grain structure in the final crystal, and they tend to see fairly flat or sightly convex interfaces in THM growth of CZT. Most likely this is due to uncertainty in the physical properties of the system. As we mentioned in chapter 2, the properties of the liquid zone are particularly suspect. Little is known about the molten form of pure CZT and almost nothing is known about non-stoichiometric mixtures of molten cadmium, zinc, and tellurium. Indeed, since the concentration of tellurium in the melt zone is a function both of the thermal profile and the amount of initial tellurium, it is even possible that the physical properties of the melt are highly process-dependent even if they are not spatially-dependent.

With such a high degree of uncertainty in the physical properties, the results presented in this chapter should be seen as an explanation of trends and processes. While we cannot predict the exact interface shape for a given set of parameters with absolute certainty, there is little doubt that the physical processes behind the model are accurate. As a result, we believe that the most valuable information from these results is the trajectory of the system through parameter space. For example, figure 4.5 suggests that there is an intermediate zone size where the centerline becomes highly concave and where either an increase or decrease in zone size should lead to a flatter interface shape. Discussions with our collaborators have revealed the existence of just such a pattern where smaller zones or larger zones tend to be much better than intermediate zones. As a result, we are confident that our model provides an informative illustration of the important processes at work in the THM system.

Chapter 5

Evolution of lee waves and the effect of constitutional supercooling

5.1 An introduction to lee waves

A surprising outcome of increasing the role of gravity in the THM system is the dramatic rearrangement of flow structure. In the previous chapter, this was demonstrated by the single vortex of Figure 4.2 (b) evolving into the multiple-vortex structure shown in Figure 4.2(c). We will demonstrate in this chapter that the flow structure near bottom of the melt zone has important effects on the stability of the growth interface later in this chapter. First though, we seek to identify the physical mechanisms responsible for such flows in the THM.

The counter-rotating vortex at the growth interface can be understood by first recognizing its link to the primary flow vortex in the liquid zone. Liquid near the centerline flows downwards and is heated for most of its journey from the top of the zone to the bottom. However, as the flow approaches the growth interface, the axial thermal gradient reverses to produce an adverse density gradient, i.e., a stabilizing density gradient, with denser fluid underlying less-dense fluid, that resists the downward flow of the warm liquid. We can imagine this situation as if the adverse density gradient were a spring:

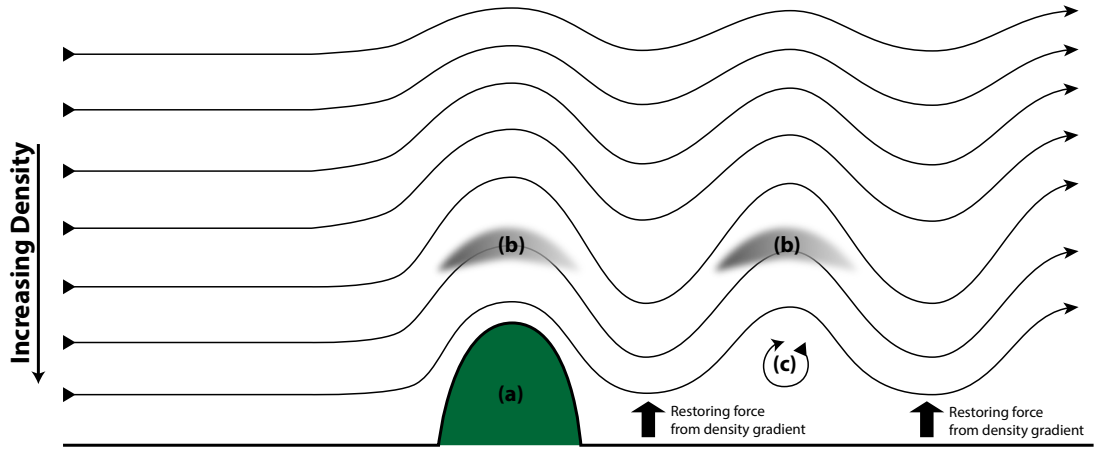

Figure 5.1: Schematic representation of how lee waves are formed in the atmosphere. Air flows over a perturbation (a) forming waves that persist downwind of the initial perturbation. As the air rises, it cools adiabatically through expansion and can sometimes condense water vapor to form clouds (b). These clouds take on the form of the oscillation and so tend to form a lens-like shape. Additionally, the air between the oscillation and the ground can become turbulent and produce counter-rotating vortices under the wave peaks.

the downwards flow acts to compress the flow and then when that flow turns sideways, there is no longer an inertial force on the spring and fluid bounces upwards, forming a wave structure with a counter-rotating vortex underneath the wave peak.

Density-stratified flows have been studied extensively in the atmospheric sciences, and the wave structures that form in these stratified flows are referred to as gravity waves. More specifically, a "lee" wave is a specific type of gravity wave that forms when stratified air in the atmosphere flows over a perturbation, such as a mountain, and produces a wave on the lee side of the mountain. Without other air currents to disrupt the waves, they may persist many miles downwind of the initial perturbation [2]. A schematic diagram of how lee waves are formed is shown in figure 5.1

Such lee waves are often identified by the characteristic lenticular clouds that form in the peaks of the wave as the rising air expands adiabatically. These lenticular clouds derive their name from their resemblance to a lens shape and are actually believed to be responsible for many of the UFO (unidentified flying object) sightings around the world. A particularly dramatic manifestation of these lenticular clouds is shown in figure 5.2

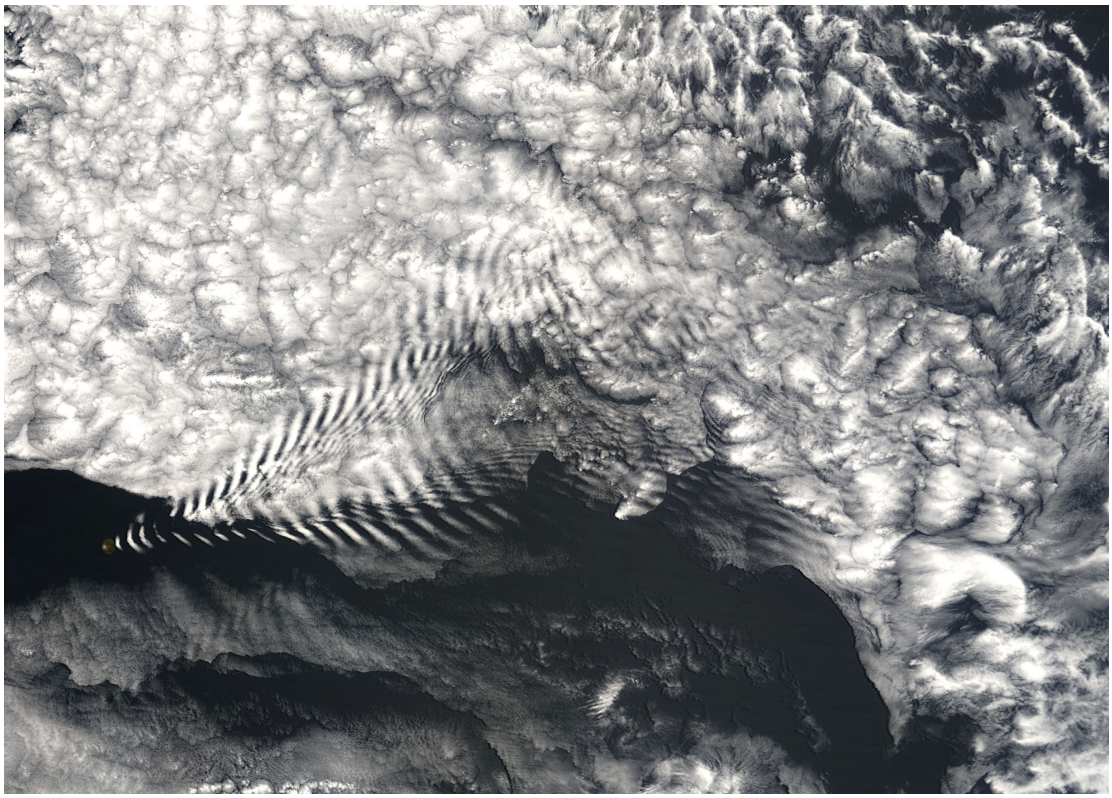

Figure 5.2: Satellite image of lee waves produced by Amsterdam Island off the coast of Antarctica in the south Indian Ocean. This photo was captured by the Moderate Resolution Imaging Spectroradiometer (MODIS) flying onboard NASA's Terra satellite [2].

as air passes over Amsterdam Island off the coast of Antarctica. The volcanic island is barely visible on the image, but the wave train resulting from the mountain extends hundreds of miles downwind of the island in the dramatic V-shape seen in the photo. A comprehensive description of lee waves and gravity waves is given by Nappo in [67], but a simplified mathematical description follows to demonstrate how lee waves evolve in the THM.

Consider a parcel of fluid acted upon only by buoyant forces; conservation of momentum in the vertical direction is represented by the following form of Newton's second law,

$$\frac{\partial^2 z'}{\partial t^2} = \frac{g}{\rho_0}\frac{\partial \rho}{\partial z} z' \tag{5.1}$$

where z' is the vertical displacement of the parcel around an equilibrium position, where it has density ρ_0, g is the acceleration due to gravity, and $\partial\rho/\partial z$ is the vertical density gradient in the fluid, which we consider to be a constant.

The solutions to this equation will be of the form

$$z'(t) = A\mathrm{e}^{iNt} + B\mathrm{e}^{-iNt} \tag{5.2}$$

where A and B are constants determined by boundary conditions and N is the classical Brunt-Väisälä frequency [67]. Using the Boussinesq approximation, the Brunt-Väisälä frequency can be rewritten in terms of the vertical temperature gradient as,

$$N = \sqrt{-\frac{g}{\rho_0}\frac{\partial \rho(z)}{\partial z}} = \sqrt{g\beta\frac{\partial T}{\partial z}}. \tag{5.3}$$

If N is imaginary, i.e., when the density gradient is positive, the solution contains a an exponential that grows without bound; this situation is referred to as a convective instability. On the other hand, if N is real, the exponential is imaginary and the solution will simply oscillate about its equilibrium position. This is the case of interest here, which occurs under the adverse density gradient that arises when $\partial T/\partial z$ is positive.

5.2 Presence of lee waves in the THM system

The Brunt-Väisälä frequency can be related to the wavelength of the oscillation, λ, and the phase velocity of the wave, $\mathbf{v}$, through the Brunt-Väisälä period,

$$\tau_{\mathrm{BV}} = \frac{\lambda}{|\mathbf{v}|}. \tag{5.4}$$

We thus expect a scaling relationship of,

$$\tau_{\mathrm{BV}} = \frac{2\pi}{N} = \frac{2\pi}{\sqrt{g\beta\frac{\partial T}{\partial z}}} \propto \left(\frac{\partial T}{\partial z}\right)^{-1/2}, \tag{5.5}$$

that should arise from this mechanism.

To test this scaling, we performed a series of calculations of steady-state THM growth where the axial heating profile was varied, keeping all other parameters constant. Specifically, the representation of the heater temperature profile was varied, via changes of $T_{\max}$ and A in eq. 2.18, to change the axial temperature gradient while maintaining an approximately constant zone height. The different heating profiles, shown in Figure 5.3(a), produced axial thermal gradients that ranged from approximately 10 K/cm up to 140 K/cm. The heater profile denoted by the thickest line in this figure corresponds to that employed for the THM cases shown previously in Figures 4.1 to 4.3.

From these steady states, the Brunt-Väisälä period was calculated from eq. (5.4), with the wavelength of the oscillation determined from the radial location of the lee-wave vortex streamfunction maximum and the phase speed of the wave taken as the maximum speed of the liquid within the zone. Figure 5.3(b) shows a log-log plot of τ_{BV} versus the maximum axial thermal gradient along the system centerline for both the 3.2-cm and 4.8-cm ampoules under the different heater profiles shown in Figure 5.3(a). In this representation, the slope of -1/2 clearly displays the lee-wave scaling behavior specified by eq. (5.5). The solid circle shown on the 3.2-cm-diameter curve corresponds to the case presented in Figure 4.2(c).

Prior models of THM growth have not identified the lee-wave instability, likely because of limited ability to resolve the complicated flows in the melt. However, Stelian and Duffar [19] present flow patterns that are consistent with the formation of a lee wave at the growth interface. Specifically, they show a large quiescent region near the growth interface where the primary flow is deflected upwards in a pattern that is likely

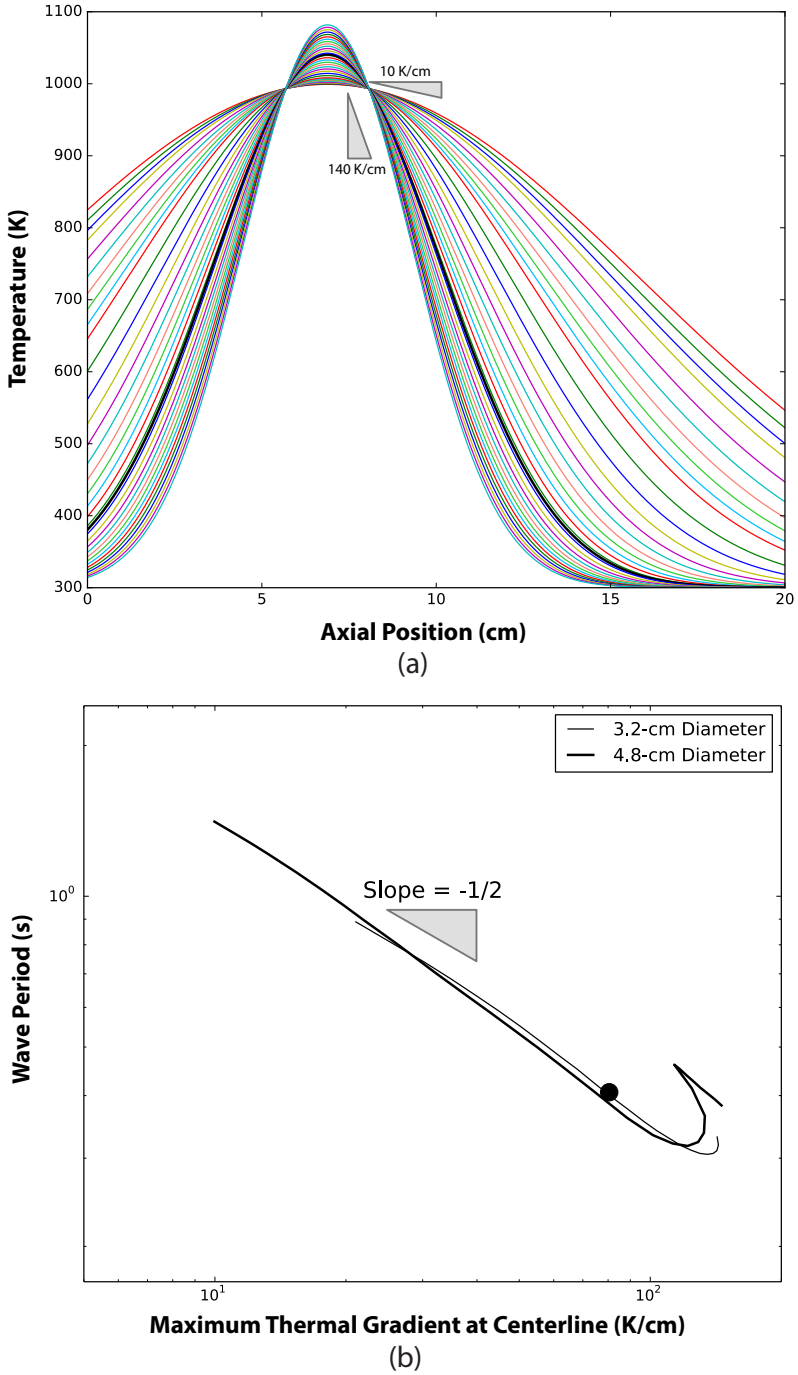

Figure 5.3: (a) Different furnace profiles are used to investigate the scaling relationship between the Brunt-Väisälä period and the thermal gradient. The thick black line represents the original Gaussian profile with parameters given in Table 2.1. (b) Log-log plot of the Brunt-Väisälä period, τ_{BV}, associated with the lee wave versus axial thermal gradient. The filled circle represents the state shown in Figure 4.2(c).

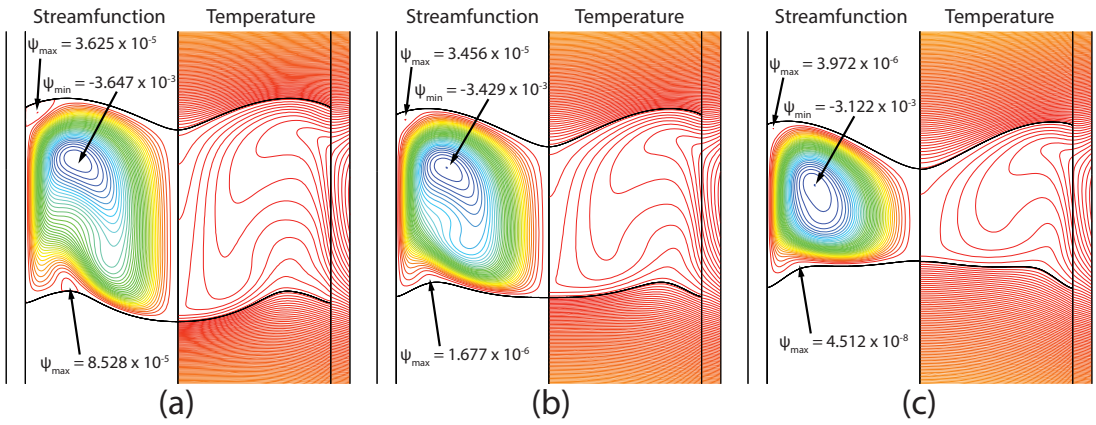

Figure 5.4: Contour plots showing the effect of decreasing the zone size at zero growth rate in a 3.2-cm diameter ampoule with initial tellurium loading of (a) 70.4 g, (b) 62.6 g, and (c) 50.8 g. The spacing between isotherms in each figure is 1.16 K, and the maximum temperature in each case is approximately 1000 K. The streamline spacing employed here does not capture the lee-wave vortex for the cases shown in (b) and (c); however, local positive streamfunction maxima, indicated for each case, show that flow reversal occurs.

a lee wave. We have also reported the formation of this flow structure and its impact on growth stability in [68, 65].

The lee-wave structure is strongly influenced by the size of the liquid zone. In larger zones, the velocity at the centerline is stronger, and the resulting lee wave has a larger amplitude. For smaller zone sizes, the lee wave itself becomes less apparent, but its effect is still measurable. This is demonstrated by the cases shown in Figure 5.4, where steady states of the 3.2-cm THM system at zero growth rate are calculated for different zone sizes, corresponding to different initial tellurium loadings. As the zone size is decreased, the size and strength of the counter-rotating vortex under the lee wave significantly lessens. While the lee wave is readily seen for the case shown in Figure 5.4(a), which has the same zone size as prior cases, the lee-wave vortex is not as apparent in the smaller liquid zones. However, there is a local maximum and change in sign of the streamfunction, i.e., where $\psi_{max} > 0$ near the growth interface in all of these cases, indicating a stagnation and flow reversal region. We will show in section 5.3 that even without a visible lee wave, the underlying mechanism and the onset of the lee wave leads to a region of recirculating flow at the growth interface. Flow due to the

lee wave inhibits the transport of tellurium in the melt and gives rise to constitutional supercooling at growth rates well below classical limits.

5.2.1 The Kelvin-Helmholtz instability and its connection to the lee wave

At very large gradients, in excess of 100 K/cm, the Brunt-Väisälä scaling relationship of figure 5.3 appears to break down as the curves for both systems turn back upon themselves. We posit that this behavior arises from a combination of factors, including the finite extent of the liquid zone and the possibility of Kelvin-Helmholtz instabilities associated with the shearing of the top of the lee waves.

Introduction to the Kelvin-Helmholtz instability

The Kelvin-Helmholtz instability can occur in density-stratified fluids where the velocity gradient opposes the density gradient. From an intuitive point of view, the Kelvin-Helmholtz instability can be thought of as a competition between inertial and buoyant forces. The mechanical energy of the system is divided into two components: the kinetic energy of the flowing fluid and the buoyant potential energy of having a heavy fluid above a light fluid. At low velocities, the buoyant potential energy dominates and so the lowest energy configuration is achieved when the heavier fluid is underneath the lighter fluid. However, since the kinetic energy scales as the velocity squared, there will be a point when the kinetic energy begins to dominate. At this point, the system can reach a lower energy state by allowing the light and heavy fluid to mix, thereby sacrificing an increase in buoyant potential so as to decrease the kinetic energy.

Mathematically, one can easily find the critical shear gradient at which this transition occurs. Although one can use linear stability analysis to arrive at this value along with the critical wavelength, a simpler argument is presented here using energy arguments by finding when the kinetic energy lost is greater than the buoyant potential gained.

Imagine two fluid packets such as those in figure 5.5 where the top fluid packet at position $z + \Delta z$ is lighter and traveling at the faster velocity, v_1, while the bottom fluid packet at position z is heavier and is traveling slower at v_2. If the fluid packets were to switch positions, the heavy packet would be accelerated and the light packet would be

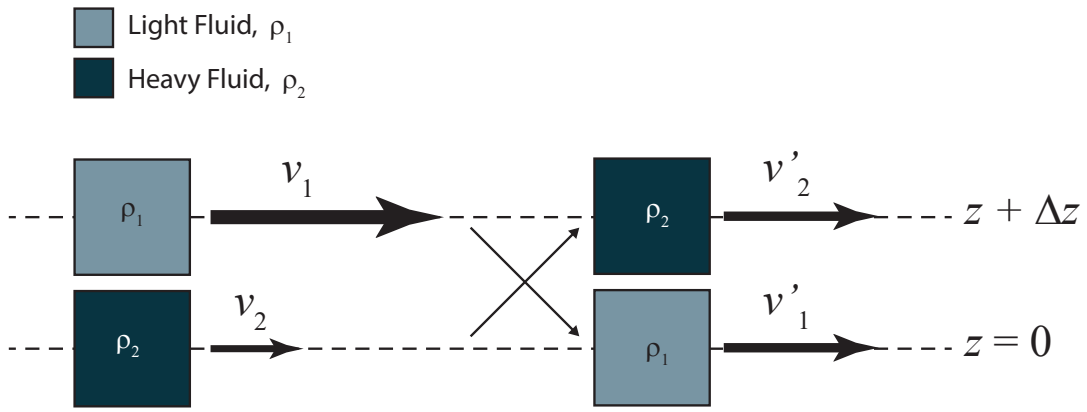

Figure 5.5: Schematic explanation for the Kelvin-Helmholtz instability depicting two fluid packets moving at velocities v_1 and v_2. As the two fluid packets exchange places, the buoyant potential increases but the kinetic energy decreases. For a Kelvin-Helmholtz instability to form, the decrease in kinetic energy must be greater than the increase in buoyant potential energy.

decelerated. Assuming that the density difference is only important for buoyant effects and not inertial effects (as we assumed in the Boussinesq approximation described in chapter 2) we can assume that the resulting velocities of the two packets, v_1' and v_2' are nearly equal.

The buoyant potential gained by the fluid packets exchanging places is equal to the net work required to raise the heavy packet and lower the light packet, or

$$W_{\mathrm{B}} = \int_0^{\Delta z} g(\rho_2 - \rho_1)\,\mathrm{d}z = g\Delta z(\rho_2 - \rho_1). \tag{5.6}$$

Here ρ is the density and g is the acceleration due to gravity. Subscripts 1 and 2 refer to the light and heavy fluid packets respectively. If we specify that we are discussing a fluid with relatively constant density gradient, we can instead express one of the densities in terms of this gradient and rewrite the buoyant work as

$$W_{\mathrm{B}} = g\Delta z\left(\rho_2 - \left(\rho_2 + \Delta z\frac{\mathrm{d}\rho}{\mathrm{d}z}\right)\right) = -g(\Delta z)^2\frac{\mathrm{d}\rho}{\mathrm{d}z}. \tag{5.7}$$

Note that the density gradient $\frac{\mathrm{d}\rho}{\mathrm{d}z}$ is negative for a system that is not convectively unstable so the work required to exchange the packets is positive.

To calculate the kinetic energy decrease for the system after the packets exchange, we first recognize that the fluid exists in a velocity gradient so it makes sense to rewrite the velocity of the light particle as $v_1 = v_2 + \Delta v$ where Δv is some velocity change that occurs over the distance Δz. Additionally, since we already assumed that the density difference was unimportant for inertial effects, we can safely assume the two densities, ρ_1 and ρ_2, are equal to some reference density, ρ, for the sake of the kinetic energy calculation. With these assumptions in mind, the total kinetic energy of the system before the packets exchange places is simply the sum of the kinetic energies of the individual packets, or

$$E_{\mathrm{K}} = \frac{\rho}{2}(v_2^2 + (v_2 + \Delta v)^2) = \frac{\rho}{2}(2v_2^2 + 2v_2\Delta v + (\Delta v)^2). \tag{5.8}$$

As we have assumed that the resulting velocities of the two packets after the exchange, v_1', and v_2', are equal, the kinetic energy of the system after the exchange is simply expressed using the average of the two initial velocities such that

$$E_{\mathrm{K}}' = \frac{\rho}{2}\left(2\Big(\frac{v_2 + (v_2 + \Delta v)}{2}\Big)\right) = \frac{\rho}{2}(2v_2^2 + 2v_2\Delta v + \frac{(\Delta v)^2}{2}). \tag{5.9}$$

Subtracting the initial energy from the final energy, the total kinetic energy change for the system is then expressed as

$$\Delta E_{\mathrm{K}} = -\frac{\rho}{2}\frac{(\Delta v)^2}{2}. \tag{5.10}$$

For the Kelvin-Helmholtz stability to manifest, the exchange of fluid packets must be more energetically stable than if the packets remained at their positions. To find this point, we write down the energy inequality such that the overall energy of the system is lowered by the packets switching:

$$0 > -g(\Delta z)^2\frac{\mathrm{d}\rho}{\mathrm{d}z} + -\frac{\rho}{2}\frac{(\Delta v)^2}{2}. \tag{5.11}$$

which can be rearranged to show that

$$\frac{1}{4} > \frac{-g(\Delta z)^2\frac{\mathrm{d}\rho}{\mathrm{d}z}}{\rho(\Delta v)^2} = \frac{N^2}{\left(\frac{\mathrm{d}v}{\mathrm{d}z}\right)^2} = \ \mathrm{Ri}, \tag{5.12}$$

where N is again the Brunt-Väisälä frequency, and Ri is the dimensionless Richardson number. The preceding energy balance shows that the Richardson number represents a

ratio between buoyant effects and shear effects with Richardson numbers smaller than 1/4 indicating that Kelvin-Helmholtz wave breaking could occur. While this criterion is necessary for the instability, it is not sufficient to predict its onset. Generally, the fastest-growing unstable wavelength is the shortest thus viscous effects will tend to stabilize the growth of any perturbations.

Effect of Kelvin-Helmholtz instability on the lee wave

To explain the anomalous scaling in figure 5.3, the Richardson number was calculated for three representative cases shown in Figure 5.6 with applied thermal gradients of (a) 10 K/cm, (b) 40 K/cm, and (c) 120 K/cm. Without constant gradients, unfortunately there is no exact Richardson number that can characterize the system. In order to be the most methodical, we used the radial position of the lee wave vortex as the radial coordinate and then the position where the z-gradient in the radial velocity was greatest for the axial coordinate. This position is shown in each sub-figure by the small star above the lee wave vortex.

While figure 5.3 (b) clearly shows that 10 K/cm represents a region where the scaling relationship holds, we can already see the wave bending over due to the high rate of shear. As the thermal gradient is changed to 40 K/cm, the maximum velocity only increases by about 40% while the buoyant force has increased by four-fold. As a result, the Richardson number is now much higher and we see that the wave shape has become more symmetric, indicating stability. Increasing the applied thermal gradient to 120 K/cm, however, shows significant distortion of the lee wave and a corresponding decrease in the Richardson number.

If both the 10 K/cm and 120 K/cm cases demonstrate a high degree of shearing the reader may ask how the onset of the Kelvin-Helmholtz instability can help explain the anomalous scaling behavior. The important detail to notice here is the size of the lee wave. At 10 K/cm, the amplitude of the wave is actually quite small while the wavelength is comparatively large, so while the strong shear acts mainly on the wave peak, it only acts upon a small portion of the wave while the buoyant forces that determine the wavelength act on the whole wave. At 120 K/cm, the wavelength has almost halved while the amplitude has increased by a factor of five. This, along with higher shear forces, actually acts to force the lee wave vortex outwards and reverse the

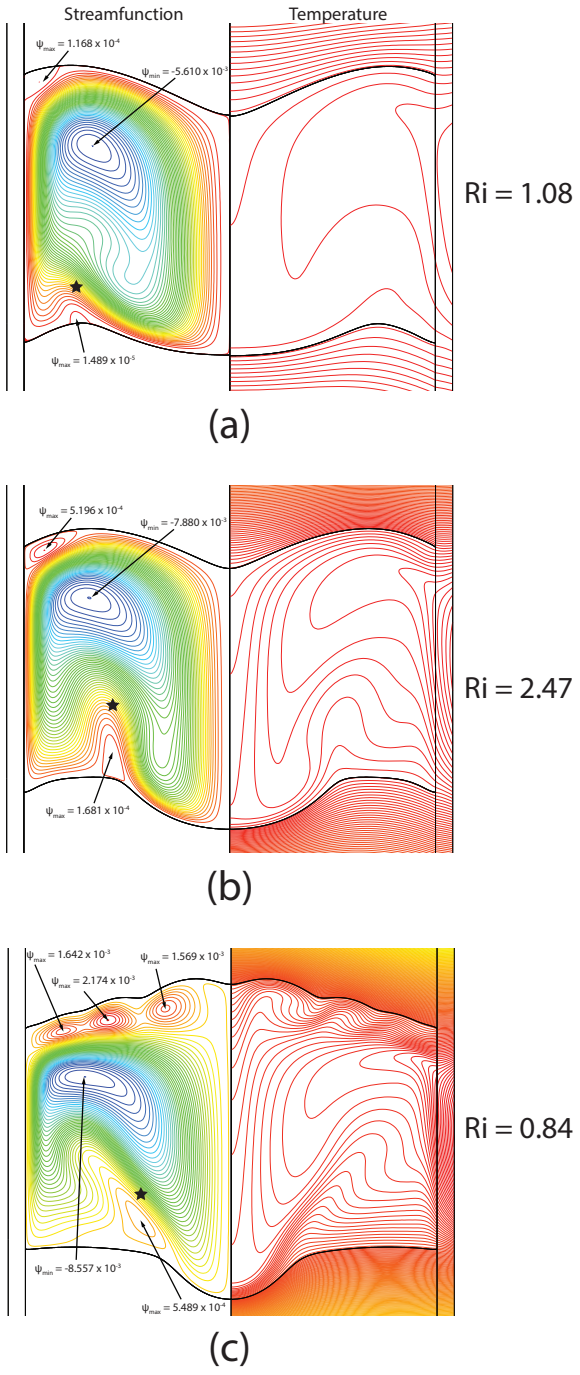

Figure 5.6: Structure of the lee wave in 4.8-cm diameter ampoule shown for applied thermal profiles with gradients of (a) 10 K/cm, (b) 40 K/cm, and (c) 120 K/cm at the approximate location of the growth interface. The Richardson number, Ri, is calculated from the thermal gradient and the z-gradient of the radial velocity at the positions marked by a star.

scaling relationship.

We should also note that at these very high gradients, several additional vortices form in the upper region of the melt where the thermal field is unstable. These additional vortices actually cause the maximum velocity in the system to decrease with increasing thermal gradients under certain conditions. Combined with the non-linear interaction between the flow structure and the growth and dissolution interface shapes, the appearance of these very strong flow cells may also contribute to the anomalous scaling behavior.

5.3 Lee waves and constitutional supercooling

5.3.1 An introduction to constitutional supercooling

While many of the advantages of CZT growth by the traveling heater method stem from the fact that it operates with a melt that is highly enriched in tellurium, constitutional supercooling also becomes a much greater concern because this excess tellurium cannot incorporate into the growing crystal. As the growth interface advances, the tellurium that cannot be incorporated into the solid accumulates in front of the interface, forming a large concentration gradient; the faster that the growth interface advances, the larger this concentration gradient becomes. This concentration gradient can be translated directly into a position-dependent melting point and when the gradient is high enough, the melting point in front of the interface will actually be higher than the local temperature and thus the melt will become undercooled. This situation is shown graphically in Figure 5.7.

Tiller *et al.*[69] presented the original analysis of morphological instability during crystal growth via the mechanism of constitutional supercooling. In short, their analysis demonstrated that stable growth of a solidification interface required that the growth velocity be slow enough to allow the melt temperature to be always greater than the composition-dependent melting temperature, which is determined by the diffusive transport of the segregated species away from the growth interface. Tiller's criterion can be derived starting with the application of conservation of a chemical species, C, across

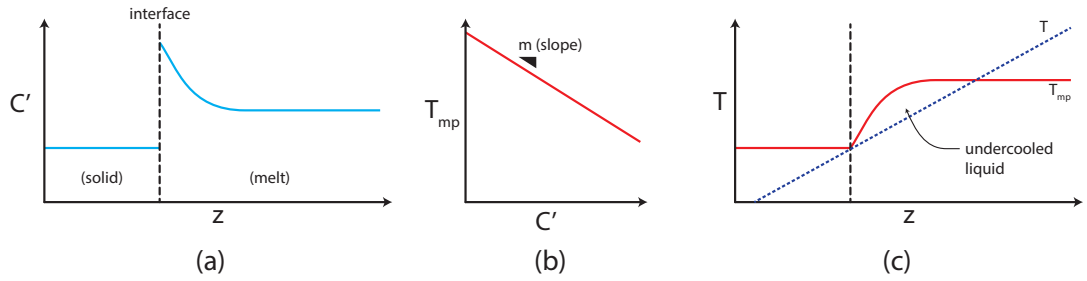

Figure 5.7: Schematic representation of constitutional supercooling. As the growth interface advances, excess tellurium is rejected in front of the growing interface (a). The concentration can be directly mapped into a local melting point via the phase diagram (b). The melting point can then be plotted as a function of position in front of the interface (c). If the local melting point exceeds the local temperature, the liquid is considered undercooled.

the growth interface,

$$\left[\mathbf{f} + C(\mathbf{v} - \mathbf{v}_\mathrm{I})\right]_\mathrm{s} - \left[\mathbf{f} + C(\mathbf{v} - \mathbf{v}_\mathrm{I})\right]_\mathrm{l} \cdot \mathbf{n} = 0 \tag{5.13}$$

where $\mathbf{f}$ is the diffusive flux, s and l denote the solid and liquid sides of the interface, v is the local velocity in the material, and v_I is the interface velocity. Grouping the diffusive and convective fluxes, this becomes

$$\mathbf{f}\big|_\mathrm{s} - \mathbf{f}\big|_\mathrm{l} = C_\mathrm{l}(\mathbf{v} - \mathbf{v}_\mathrm{I}) - C_\mathrm{s}(\mathbf{v} - \mathbf{v}_\mathrm{I}), \tag{5.14}$$

which becomes

$$-\mathcal{D}\mathbf{n} \cdot \nabla C\big|_\mathrm{s} + \mathcal{D}\mathbf{n} \cdot \nabla C\big|_\mathrm{l} = -(C_\mathrm{l} - C_\mathrm{s})\mathbf{n} \cdot v_\mathrm{g}\mathbf{e}_x, \tag{5.15}$$

after the application of Fick's law, $\mathbf{f} = -\mathcal{D}\nabla C$, and after recognizing that the flow velocity, v, will be zero at the interface. Here we have also recognized that the interface velocity is simply the growth rate, v_g. While crystal growth is inherently a non-equilibrium process, at a continuum scale, it is safe to assume that the growth interface is very nearly at thermodynamic equilibrium (as was assumed in chapter 2). As such, we can make use of the equilibrium partition coefficient, $K_\mathrm{p} = C_\mathrm{s}/C_\mathrm{l}$, to eliminate the solid concentration. Furthermore, solid diffusion coefficients tend to be two orders of magnitude smaller than those in the liquid phase. Diffusion in the solid tends to be in

general slower than the growth process, and as a result we can ignore the concentration gradient in the solid. Incorporating these assumptions into our equation then yields,

$$\mathcal{D}\mathbf{n}\cdot\nabla C\big|_{\mathrm{l}} = -(1-K_{\mathrm{p}})C_{\mathrm{l}}\mathbf{n}\cdot v_{\mathrm{g}}\mathbf{e}_x, \tag{5.16}$$

and in 1-D,

$$\mathcal{D}\frac{\partial C}{\partial x}\bigg|_{\mathrm{l}} = -(1-K_{\mathrm{p}})C_{\mathrm{l}}v_{\mathrm{g}}. \tag{5.17}$$

Solving for the concentration gradient at the liquid/solid interface, we are left with

$$\frac{\partial C}{\partial x} = -\frac{C_{\mathrm{l}}(1-K_{\mathrm{p}})v_{\mathrm{g}}}{\mathcal{D}}. \tag{5.18}$$

For constitutional supercooling to occur, the gradient must be high enough so that the local melting point increases in front of the interface faster than the local temperature (see Figure 5.7). Mathematically, we can express this with the inequality,

$$\frac{\mathrm{d}T}{\mathrm{d}x} > m\frac{\mathrm{d}C}{\mathrm{d}x} \tag{5.19}$$

where m is the slope of the liquidus line. The resulting inequality for stability is

$$\frac{\mathrm{d}T}{\mathrm{d}x} > m\left(-\frac{C_{\mathrm{l}}(1-K_{\mathrm{p}})v_{\mathrm{g}}}{\mathcal{D}}\right) \tag{5.20}$$

which can be rearranged to give a maximum stable growth rate of

$$v_{\mathrm{g}} < -\frac{\mathcal{D}}{mC_{\mathrm{l}}(1-K_{\mathrm{p}})}\frac{\mathrm{d}T}{\mathrm{d}x} \tag{5.21}$$

bearing in mind that m is negative and K_{p} is less than one for tellurium in the CZT system. If we rewrite this equation in terms of excess tellurium, C', the partition coefficient is on the order of 10^{-4}, or approximately zero, transforming our limit into

$$v_{\mathrm{g}} \leq \frac{-\mathcal{D}}{mC'}\frac{\partial T}{\partial z}. \tag{5.22}$$

A consistent interpretation of this constraint is simply that stable growth occurs when no undercooled liquid exists in front of the growth interface.

The connection between undercooling and the unstable interface can be understood through an analysis of the composition field and its effect on the melting point as was done by Rutter and Chalmers [70]. Consider figure 5.8, which depicts a three-step

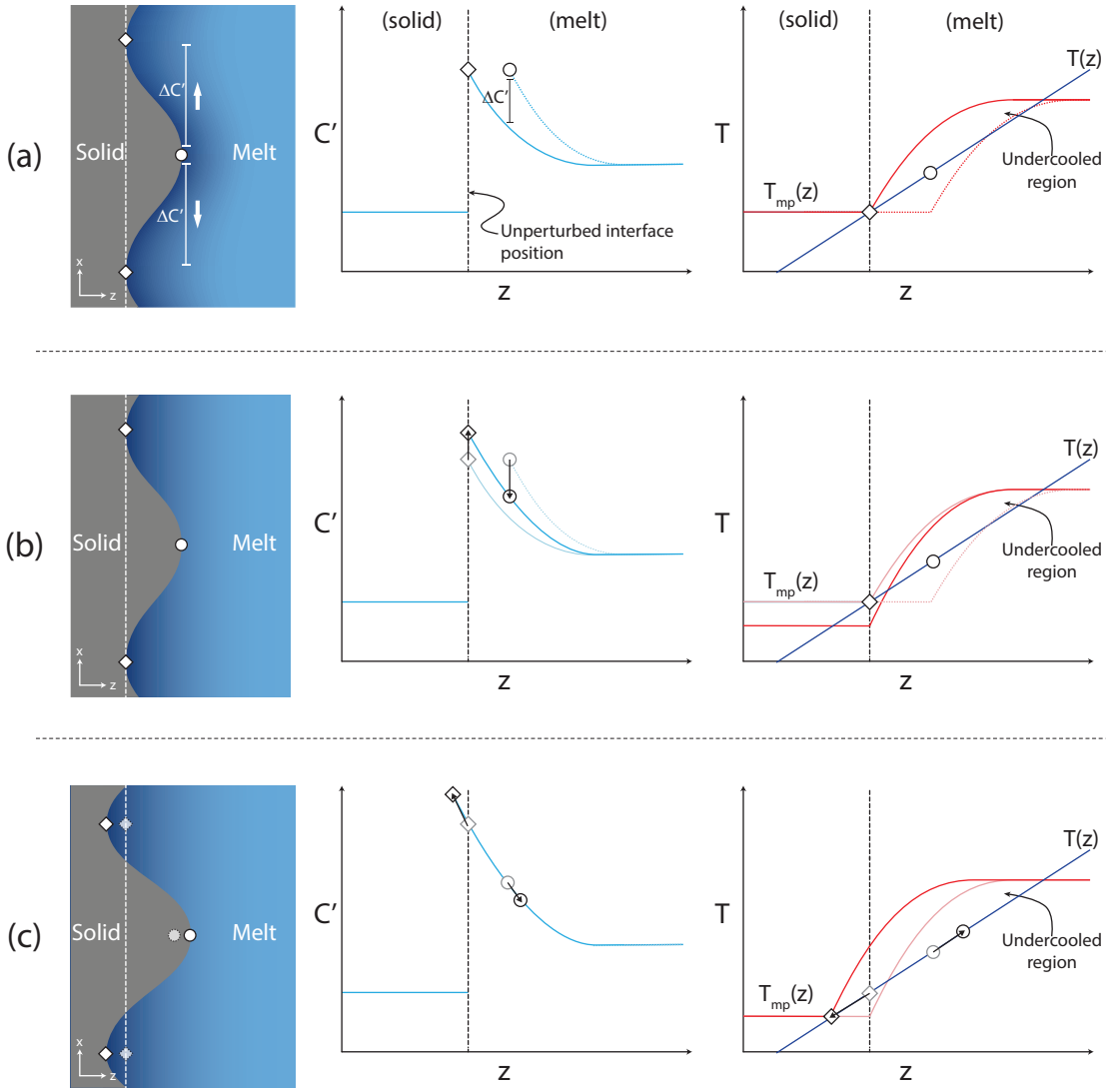

Figure 5.8: Schematic process by which an interface becomes unstable in the presence of constitutional supercooling. The sub-figures represent (a) the initial perturbation forming, (b) the rearrangement of the composition field in response to the perturbation, and (c) the resulting growth of the instability under supercooled conditions. The schematic on the left represents the concentration field with darker shading corresponding to higher concentrations. In the plots of temperature and concentration (right and middle respectively), the circle and diamond represent the corresponding points in the schematic at left with the dashed lines corresponding to values in front of the perturbation peak. Faded lines indicate the previous state of the system. Note that in the plot of melting point, the circle and diamond will not necessarily lie on the melting point line, indicating a driving force for solidification or melting.

mechanism by which the interface will become unstable while growing into a constitutionally supercooled liquid. First, a perturbation occurs that drives a projection of the solid into the supercooled liquid as is shown in figure 5.8 (a). Initially, the composition field has not reacted and so the concentration all along the interface is the same and the concentration at a given z-position now varies with x. However, we assume that the thermal field was not effected by the perturbation and remains a 1-D function of z. Looking at the plot of temperature in figure 5.8 (a), the projection has driven the system out of equlibrium at the point marked by the circle where the temperature is now higher than the local melting point.

Before the projection can melt back though, the concentration field reacts. If we examine the composition field in the x-direction at the z-position of the projection tip, we see that the concentration decreases away from the tip. This will drive a species flux in the x-direction towards the liquid ahead of the rest of the perturbation valleys. Two things will then happen: the concentration at the point marked by the circle will decrease while the concentration at a position in front of the diamond will increase. Since the excess tellurium must be transported away from the interface through diffusion, the concentration at the diamond must rise in response to maintain the necessary gradient for transporting this material into the bulk liquid. Consequently, the lateral (x-direction) concentration gradient will be extremely small and the composition field will return to being largely a 1-D function of z. Now both the peak and the valley are out of thermodynamic equilibrium; they are now at temperatures below and above their respective melting points as is seen in the temperature graph of figure 5.8 (b).

One can see that if there had been no undercooling in front of the interface, the melting point curve would be unable to exceed the local temperature at the projection peak. As a result, the driving force would be for both the peak and valley to recede such that a flat interface is again achieved. As figure 5.8 (c) shows however, the presence of undercooling will cause the valleys to recede while the peaks grow. This will restart the whole process once more and the instability will grow without bound. There are other factors that influence the morphological stability of an interface including the effects of latent heat an thermal conductivity. For more on this subject, the interested reader is referred to chapter 7 for a full discussion of the interplay between undercooling and morphological instability.

5.3.2 Constitutional supercooling limits growth in the THM system

We consider the case of smallest zone size, corresponding to the prior case of Figure 5.4(c), and compute new states at higher growth rates. Figure 5.9 shows two cases, with the excess tellurium concentration field in the liquid zone indicated on the left and the overall temperature field shown on the right. With the concentration and temperature fields determined, we evaluate the local thermodynamic state of the liquid, denoting the liquid to be supercooled when the concentration-dependent melting point is higher than the calculated local temperature, namely when

$$T \leq T_{\mathrm{mp}}(C'). \tag{5.23}$$

Regions of supercooled liquid adjacent to the growth interface are indicated in both cases, clearly showing that constitutional supercooling and growth instability are predicted to occur.

Supercooling in the liquid is first encountered just below 1.5 mm/day, consistent with the shaded region shown in Figure 5.9(a). Of note is the fact that initial supercooling coincides perfectly with the radial position of the lee-wave vortex, even when no obvious lee wave is present. Further increases in the growth rate lead to an even larger undercooled region at this location, as indicated in Figure 5.10(b). Additional supercooling is also observed at the centerline for this case of higher growth rate.

According to the classical understanding of constitutional supercooling, tellurium rejected at faster growth rates is unable to diffuse away fast enough unless the local concentration near the interface increases, thus further decreasing the melting temperature and increasing the likelihood of supercooling in front of the growth front. However, this behavior is *not quantitatively* explained by the limit of Tiller *et al.*, eq. 5.22, which predicts a growth rate limit of 8.8 mm/day for this system. To understand why supercooling occurs at growth rates *far less* than predicted by the Tiller limit, we must examine the details of the tellurium concentration field in front of the growth interface, which depends on segregation, diffusion, and convection via the flow field near the interface.

The large, primary vortex in the liquid zone generally acts to sweep the rejected tellurium from the growth front into the bulk of the melt, thus preventing supercooled regions over most of the interface. However, this transport is disrupted by the lee-wave

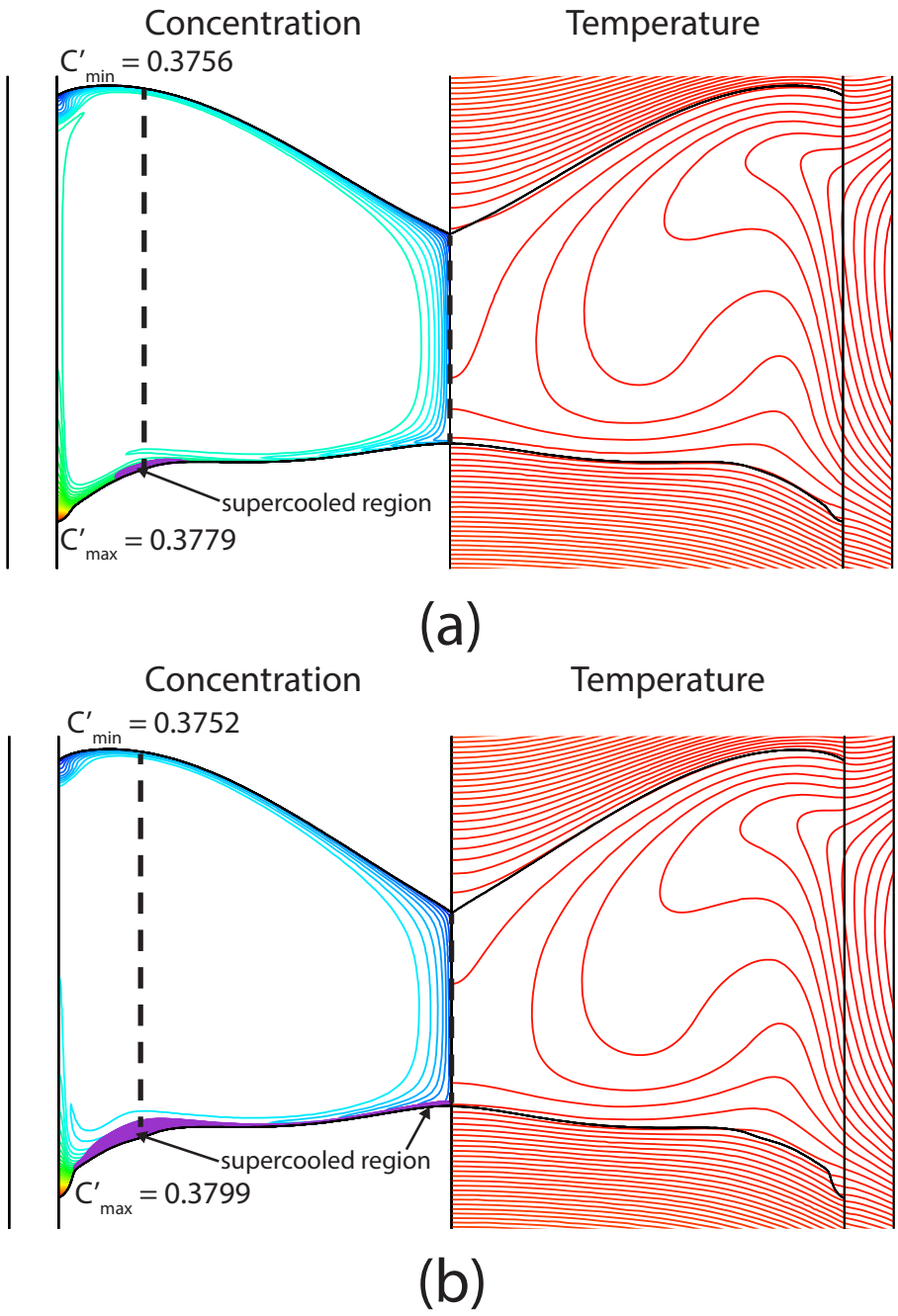

Figure 5.9: Contour plots of tellurium concentration and temperature for growth rates of (a) 1.5 mm/day and (b) 2.32 mm/day for the case of 50.8 g of initial tellurium in the 3.2-cm ampoule (the same case shown by Figure 5.4c). Supercooled regions are represented by the shaded area near the interface, while the dashed lines indicate the positions where the plots of Fig. 5.10 are constructed.

vortex, which is circulating in the opposite direction of the primary vortex. This reversal in flow along the interface disrupts the sweeping away of tellurium by the primary vortex and leads to a local accumulation of tellurium that decreases the melting point and ultimately leads to supercooling. Thus, the critical element leading to supercooling and instability is the formation of the lee wave.

Figure 5.10 represents another view of these cases, where solid curves show the temperature in the liquid plotted as a function of axial position in front of the growth interface and dashed curves show the local melting temperature, which is determined from the phase diagram and the local concentration of tellurium in front of the interface. Supercooling occurs when the actual temperature falls below the local melting temperature and is denoted in the plots by a shaded region. Figure 5.10(a) plots these quantities upward along $r = 1.2$ cm, the position of the lee-wave vortex. This is the position where the interface first becomes unstable for growth rates slightly less than 1.5 mm.day. Note also that the melting point at the interface, the point at which the solid and dashed profiles intersect (at left), steadily decreases with increasing growth rate, consistent with the higher levels of rejected tellurium during faster growth.

Figure 5.10(b) plots the axial temperature and melting points along the centerline for different growth rates. First, note that the interface temperature actually increases as the growth rate is increased, opposite to the behavior observed under the lee-wave vortex. This occurs because the primary flow vortex directly transports tellurium-poor (cadmium-rich) liquid from the dissolution interface downward along the system centerline, and this effect becomes stronger with increasing growth rate, leading to increasing interface temperatures. Eventually, however, the additional tellurium rejected at higher growth rates creates a large concentration gradient that also leads to undercooling and instability in the center.

5.4 Conclusions

In this chapter, we have shown that, fluid flow in the relatively small liquid zone is strong enough to give rise to complicated flow structures. Of particular importance is the formation of a lee wave and associated counter-rotating vortex adjacent to the growth interface, which we have demonstrated to arise from the same density stratification

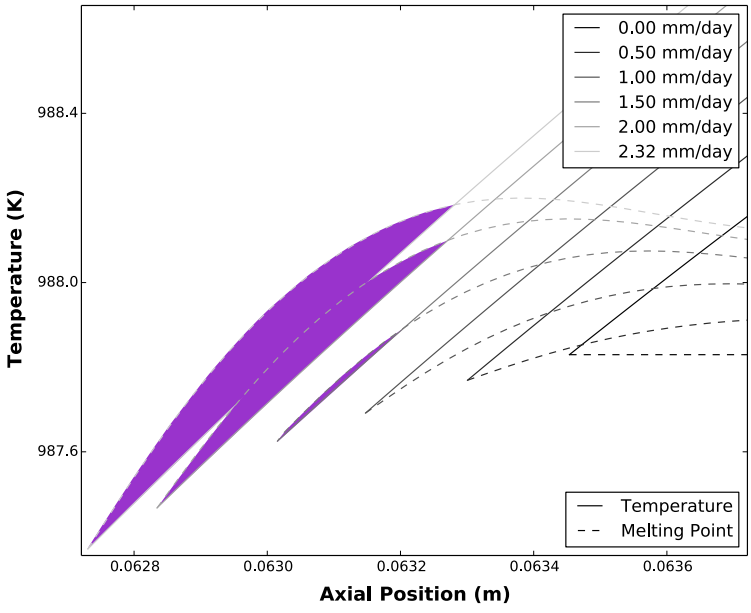

(a)

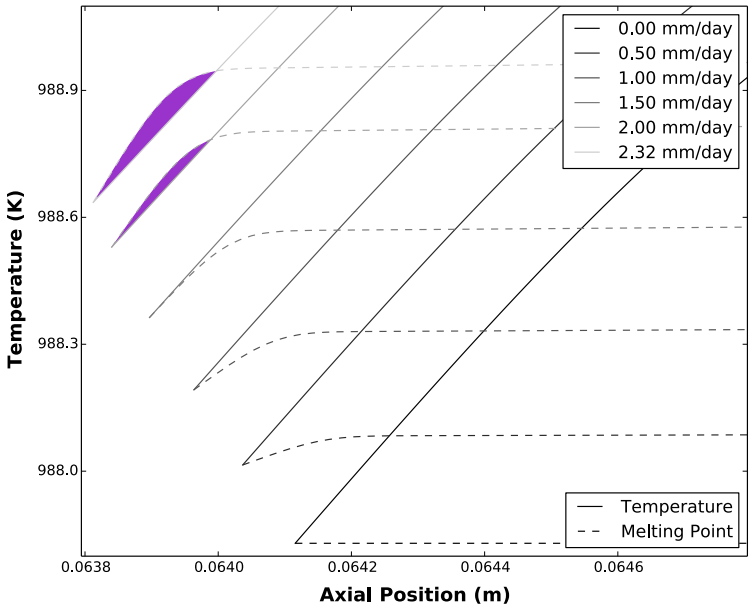

(b)

Figure 5.10: Temperature and composition-dependent melting point profiles in the liquid zone are plotted as a function of axial position along lines of (a) $r = 1.2$ cm and (b) $r = 0$ cm. Each line begins at the growth interface and continues into the liquid zone. Constitutionally supercooled regions, where the local melting point is higher than the local temperature, are identified by shaded areas.

mechanism as acting in atmospheric flows.

These lee-wave flow structures inhibit the lateral convective transport of tellurium rejected by segregation along the growth interface, leading to local accumulations of tellurium. The increased tellurium in the liquid depresses the thermodynamic melting point, ultimately leading to supercooling of the liquid adjacent to the interface and thereby promoting growth instability. Significantly, this mechanism is shown to occur even in smaller zones where the lee-wave structure is not nearly as apparent as in larger zones. Because the supercooling is driven by lateral convection of tellurium along the interface rather than diffusion away from it, constitutional supercooling arises at growth rates far lower than predicted by the classical analysis of Tiller *et al.* [69]. Indeed, we have asserted that this is the fundamental mechanism that has acted to severely limit growth rates in the traveling heater method.

Importantly, since the lee-wave vortex is triggered by the stable temperature gradient near the growth interface, increasing the applied thermal gradient is only expected to exacerbate the lee wave problem. Paradoxically then, the classical strategy of increasing the thermal gradient to suppress constitutional supercooling and allow increased growth rates (per the limit expressed by eq. 5.22), will not be as effective in the travelling heater method.

Future work will assess strategies whereby added body forces may alter the deleterious lee-wave flow structure and permit faster growth. Two promising approaches are the accelerated crucible rotation technique (ACRT), which has been studied in Bridgman growth [71, 72], and the application of a rotating magnetic field (RMF), which we have considered in microgravity THM systems [73]. We will further consider these effects in THM in forthcoming studies. We believe that computational models, based on that employed here, will be invaluable toward the development of effective strategies to increase growth rates in the THM.

Chapter 6

Improving interface morphology in the Bridgman growth technique

While Bridgman crystal growth technique and the traveling heater method share much in terms of their mathematical models, there are distinct differences that differentiate the two systems. For the THM, the heater produces a temperature maximum within the liquid zone whereas in the Bridgman system, the temperature tends to monotonically increase through the liquid zone. This difference in particular leads to flow behaviors that are drastically different. Therefore, the following discussion, while extremely useful in Bridgman systems, is of less value in the THM system. This chapter is mostly independent of the rest of this thesis although some conclusions from this chapter could be applied to the THM system due to the universal mechanisms of heat transfer.

6.1 Introduction and prior Literature

While Percy Williams Bridgman received his Nobel Prize for ground-breaking research on high-pressure physics [74], it is his namesake process [75], the Bridgman method, described "more or less in passing" [76] that established his legacy in the field of crystal growth. With significant modifications by Stockbarger [77] to better define axial

furnace profiles, the Bridgman-Stockbarger technique has become indispensable for the growth of a wide variety of crystals, from II–VI semiconductors [44, 11] to group IV semiconductors [78, 79] to oxide materials [80, 81].

It has been widely appreciated that the macroscopic shape of the solidification interface during growth is an important determinant of crystal quality [82], with a convex interface tending to produce fewer defects and favorable grain selection conditions [83]. Here, we define a convex interface as curving into the melt, whereas a concave interface extends into the solid. In Bridgman systems, the interface shape is determined by a balance of heat fluxes between the melt and the solidifying crystal and, as a result, controlling these heat fluxes is instrumental for interface shape determination.

Many previous studies have analyzed the heat transfer environment in the Bridgman system and have offered suggestions for better interface control. Wilcox and coworkers [83, 84] performed some of the first studies of the interaction between heat transfer in the furnace and the shape of the growth interface. Representing a furnace via two isothermal zones, both works demonstrated that the shape of the growth interface is highly sensitive to heat transfer conditions. Jasinski and Witt [85] employed a more realistic numerical model to provide one of the most comprehensive studies of the factors influencing interface shape. Their work was consequential, because they offered perhaps the first practical recommendations for achieving a convex growth interface: the interface should be located closer to the hot zone and additional heating should be provided near the growth interface. Taghavi and Duval [86] performed an inverse calculation to demonstrate the furnace temperature profiles that would be required to achieve specified interface shapes. While some of the furnace profiles that they computed were wildly unrealistic, they demonstrated that achieving a flat growth interface requires discarding simple notions of constant gradients and isothermal zones.

More recent studies by Volz *et al.* [87] and Derby and coworkers [88, 3] have employed more extensive computational tools to answer questions about promoting convex interfaces in specific growth systems. Volz *et al.* focused on a system for growing germanium and further reinforced the conclusions of Jasinski and Witt, i.e. that localized heating near the growth front could lead to a convex interface shape. In contrast, Derby and coworkers considered both Bridgman and vertical gradient freeze systems for the growth of CdZnTe (CZT). Kuppurao and Derby [88] demonstrated that suitable design

of the support pedestal, specifically the use of a "cold finger" underneath the tip of the ampoule, could redirect heat flows, promoting a convex interface shape in the early stages of growth. The later work by Zhang *et al.* [3] posited that a dynamic, "bell-curve" furnace profile could produce and maintain a convex interface shape. Despite the different system and material, Derby and coworkers concluded similarly to Volz *et al.* that the key to a convex interface was the presence of inward radial heat fluxes near the growth interface.

Whereas all of these studies focused on a specific system and strategy to promote a convex interface, we believe that these approaches can be unified under a more general framework. For our analysis, we begin with the idea of Jasinski and Witt [85] of a localized application of heat to the surface of the crucible near the axial location of the interface. Lan *et al.* [89] appear to be among the first to implement this idea via the use of a "booster" heater, which also formed the basis for the study by Volz *et al.* [87]. In the following analysis, we consider the change in structure of the heat flows though the Bridgman system caused by a booster heater. We then formulate a mathematical criterion to judge whether a given axial furnace profile will tend to produce the heat fluxes required for a convex interface. Subsequently, we show that this criterion explains the results found in the previous studies on interface control and further demonstrate, through heat transfer simulations, that the same criterion can be used to guide furnace design.

6.2 Heat transfer analysis

In the traditional design of the Bridgman system, the furnace consists of three regions: a hot zone at a temperature above the melting point, a cold zone at a temperature below the melting point, and a "gradient" zone in between. The classical, idealized notion of such a setup is that, within the gradient zone, heat will flow predominantly in the axial direction, as indicated in Fig. 6.1(a). In this case, there is no radial input or extraction of heat in the gradient zone, as all of the heat simply flows down into the crystal.[1]

By introducing a booster heater just above the interface, as Lan [89] and Volz [87]

[1] To simplify our discussion, we are considering quasi-steady-state heat transfer without complications due to melt convection, unequal thermal conductivities, the presence of an ampoule wall, or the release of latent heat at the solidification interface. We comment on these factors in the conclusions.

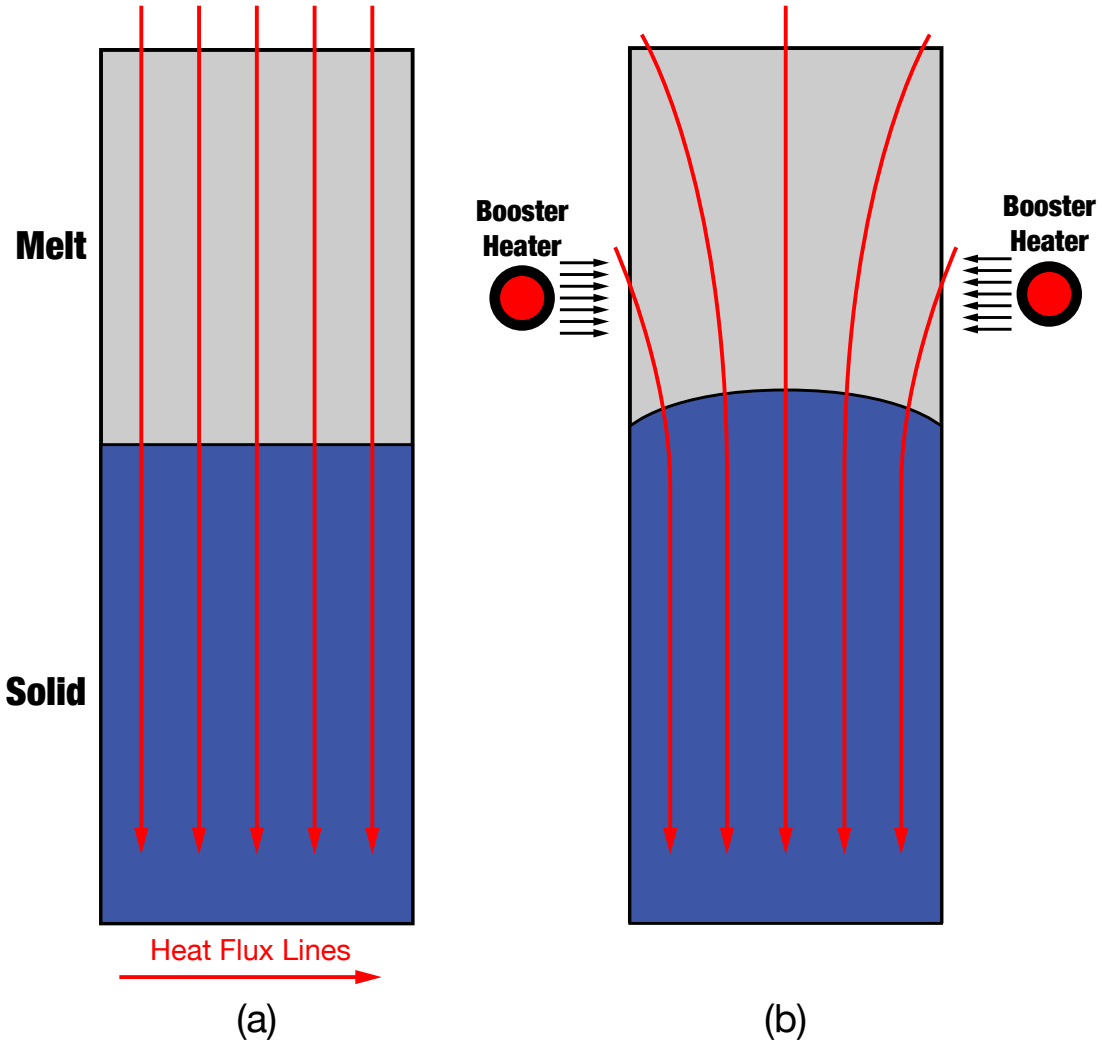

Figure 6.1: Schematic of heat transfer in a crystal growth system (a) without a booster and (b) with a booster heater. The booster heater tends to cause the heat flux lines to converge inward at the location of the interface, promoting a convex shape.

advocated, the heat fluxes are directed inwards. With the presumption that the melt-solid interface lies along the melting-point isotherm and is thus perpendicular to the heat flux lines, this scenario will produce a convex interface, as shown in Fig. 6.1(b). Similarly, it is has also been suggested that one should grow "high in the gradient zone," i.e., placing the interface closer to the hot zone, in order to provide a situation similar to that attained with the booster heater.

However, these idealized pictures are too simple. To maintain perfectly vertical heat fluxes in the solid portion of the crystal, the temperature of the furnace through the gradient zone must exactly match the that of the crystal in order to eliminate radial heat fluxes. The problem with the booster is not its action of adding heat to the system, rather it is how to remove the heat added by the booster.

6.2.1 Analysis

A more accurate depiction of the heat fluxes in the system is shown in Fig. 6.2, where heat is entering from a hot zone in the liquid and is exiting into the cold zone surrounding the solidified crystal. This figure also shows that, for the same heat flux configuration, the interface could adopt either a convex or concave shape, depending on its position within the furnace. As a result, the location of the interface must be carefully controlled relative to the booster heater.

We represent the heat flux using vector notation as,

$$\mathbf{q} = q_r \mathbf{e}_r + q_z \mathbf{e}_z, \tag{6.1}$$

where $\mathbf{e}_r$ and $\mathbf{e}_z$ are the unit vectors in the radial and axial directions and q_r and q_z are the respective components of the heat flux vector. From Fig. 6.2(a), it is apparent that the radial component of the heat flux should be negative above the melting point for the interface to be convex, namely,

$$q_r < 0. \tag{6.2}$$

As discussed previously, one thinks of attaining this condition via the booster heater; however, unless we can guarantee that the additional heat is always *added above* the interface and *removed below,* the success of a booster is not assured. Rather, we desire

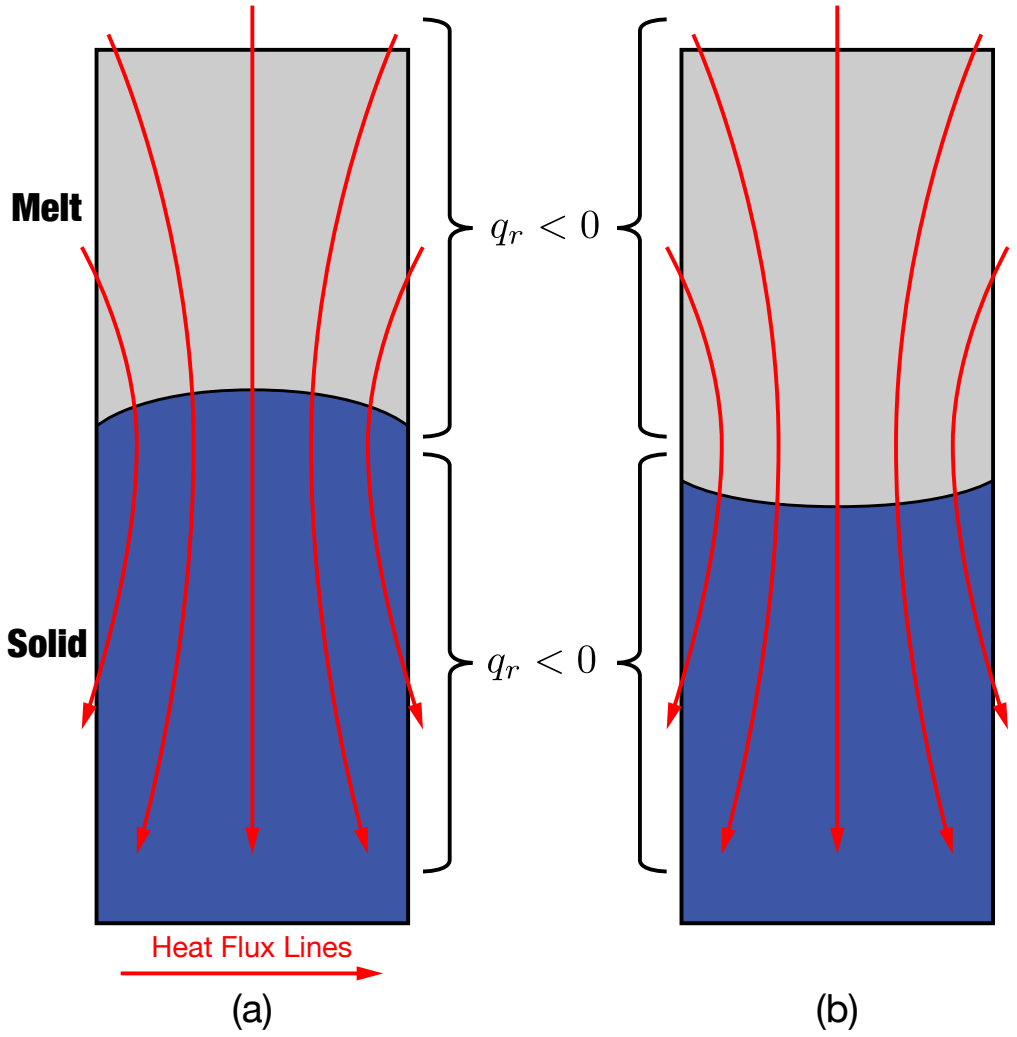

Figure 6.2: Schematic representation heat fluxes in a system with a booster heater and showing that heat is removed radially below the growth interface. In (a), the interface shape is convex due to the fact that the interface is located in the region where the radial component of the heat flux is negative. However in (b), the interface is located where the radial component of the heat flux is positive and a concave shape results.

to infer both the heat fluxes and the position of the interface solely from the furnace temperature profile.

The above criterion can be transformed in terms of the axial temperature via the application energy conservation. At steady state, without melt convection or heat generation, the conservation energy equation is written in 2D, axisymmetric coordinates as,

$$\frac{1}{r}\frac{\partial}{\partial r}\Big(rq_r\Big) + \frac{\partial q_z}{\partial z} = 0. \tag{6.3}$$

Applying a finite difference,we argue that the first term of the energy balance, eq. 6.3 is approximated by,

$$\frac{\partial}{\partial r}\Big(rq_r\Big) \approx \frac{(rq_r)|_r - (rq_r)|_{r=0}}{r} = q_r. \tag{6.4}$$

Arguing again that q_r must be negative above the melting point for the interface to be convex (see Fig. 6.2a), this implies that the remaining term of the energy balance must be positive, namely,

$$\frac{\partial q_z}{\partial z} > 0, \quad \text{when } T \geq T_m. \tag{6.5}$$

Relating the heat flux to the temperature through Fourier's law, the above inequality becomes,

$$\frac{\partial}{\partial z}\Big(-k\frac{\mathrm{d}T}{\mathrm{d}z}\Big) > 0, \tag{6.6}$$

or, since the thermal conductivity k must always be positive,

$$\frac{\mathrm{d}^2T}{\mathrm{d}z^2} < 0, \quad \text{when } T \geq T_m. \tag{6.7}$$

To promote a convex interface, the axial temperature profile of the furnace should have negative curvature at the melting point and above.

6.3 Application of criterion

6.3.1 Prior studies

While the preceding analysis is fairly idealized, it can readily be used to reinterpret the prior literature on interface control in Bridgman systems. For example, let us consider the prior studies studies of Volz *et al.* [87] and Zhang *et al.* [3] that sought to influence the interface shape through direct modification of the applied furnace profile.

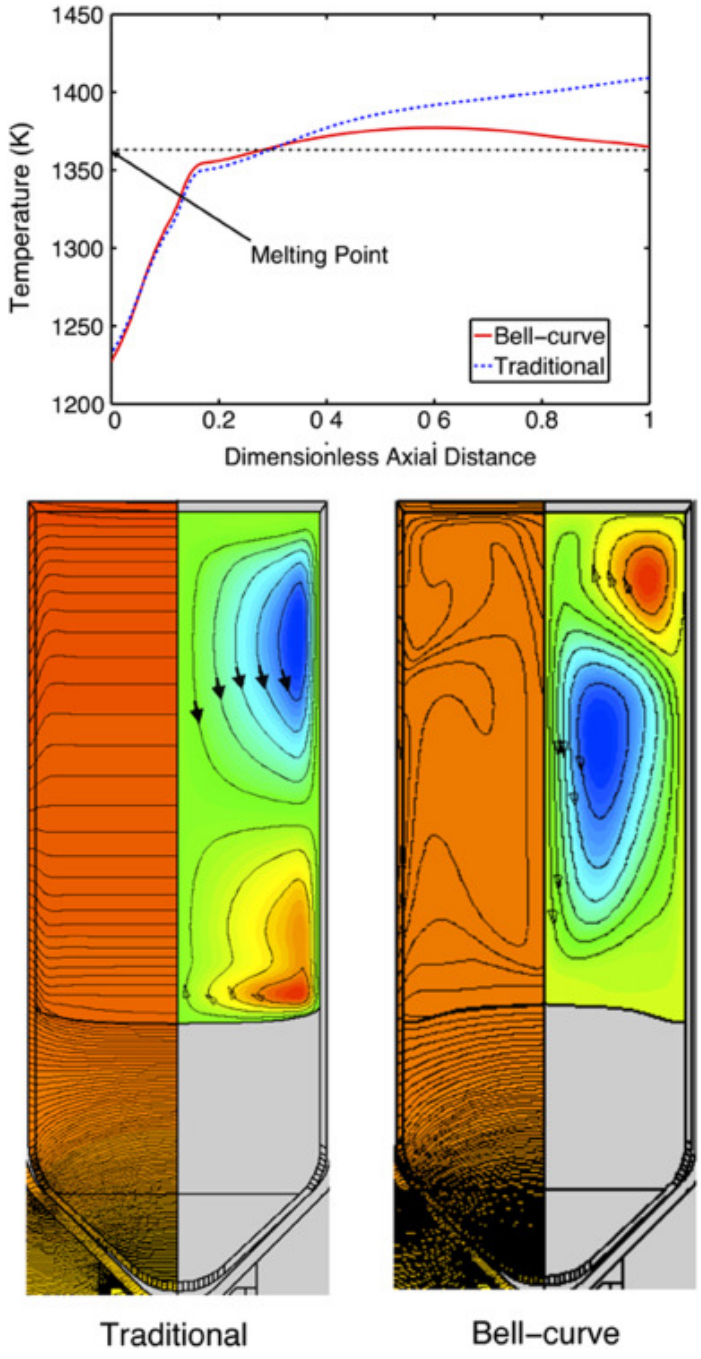

Figure 6.3: Top: Axial furnace temperatures; dashed indicates linear profile and solid is the bell-curve profile. Bottom: Simulations of CZT growth under the two profiles. A convex interface shape is produced by the bell-curve profile, which exhibits negative curvature above the melting point. Adapted from [3] with permission from Elsevier.

The former introduced a Gaussian component to an otherwise linear gradient region between the hot and cold zones of the furnace, and the latter used a vertical gradient freeze furnace to completely challenge the standard notion of a hot and cold zone. In both studies, the transition from a convex to concave interface shape was achieved via changes in the axial thermal profile from positive or zero curvature to negative curvature near the melting point.

With the linear profile used as a base-line by Volz *et al.*, the dominant effects on the shape of the interface were the ratio of melt and solid thermal conductivities (a value of 2 in their analysis, tending to promote a concave interface) and the latent heat of solidification. As a result, the interface naturally adopts a concave shape with the assumed linear profile of the furnace. Upon increasing the contribution of the Gaussian component of the temperature profile (argued as the outcome of a booster heater), a region is formed where $\mathrm{d}^2T/\mathrm{d}z^2 < 0$. As this effect is increased and the curvature of the furnace profile becomes more negative, the interface shape eventually switches from concave to convex.

Figure 6.3 shows an outcome from Zhang *et al.* [3] in which one can very clearly see the change in interface shape from concave to convex when the traditional, linear furnace profile is replaced by the bell-curve profile. Consistent with the analysis discussed above, the bell-curve profile exhibits negative axial curvature, $\mathrm{d}^2T/\mathrm{d}z^2 < 0$, above the melting point.

6.3.2 Application to furnace design

The negative curvature criterion can be applied to furnace design. For example, we and LBNL collaborators have proposed a multi-zone Bridgman furnace to grow mixed-halide, scintillator crystals that features a hot zone, a cold zone, and a one-coil booster heater. Heat transfer in this system was simulated using the CrysMAS code developed by the Fraunhofer IISB. The calculations incorporated both conductive and radiative heat transport, as well as tracking of the liquid-solid interface, but the effects of flow, latent heat, composition, and growth rate were not considered. A close-up view of furnace and ampoule are shown in Fig. 6.4, along with predicted thermal fields obtained using control points for the hot and booster zones of 1243 K and 1193 K, respectively.

Results for the initial design, shown in Fig. 6.4(a), clearly demonstrate that, despite

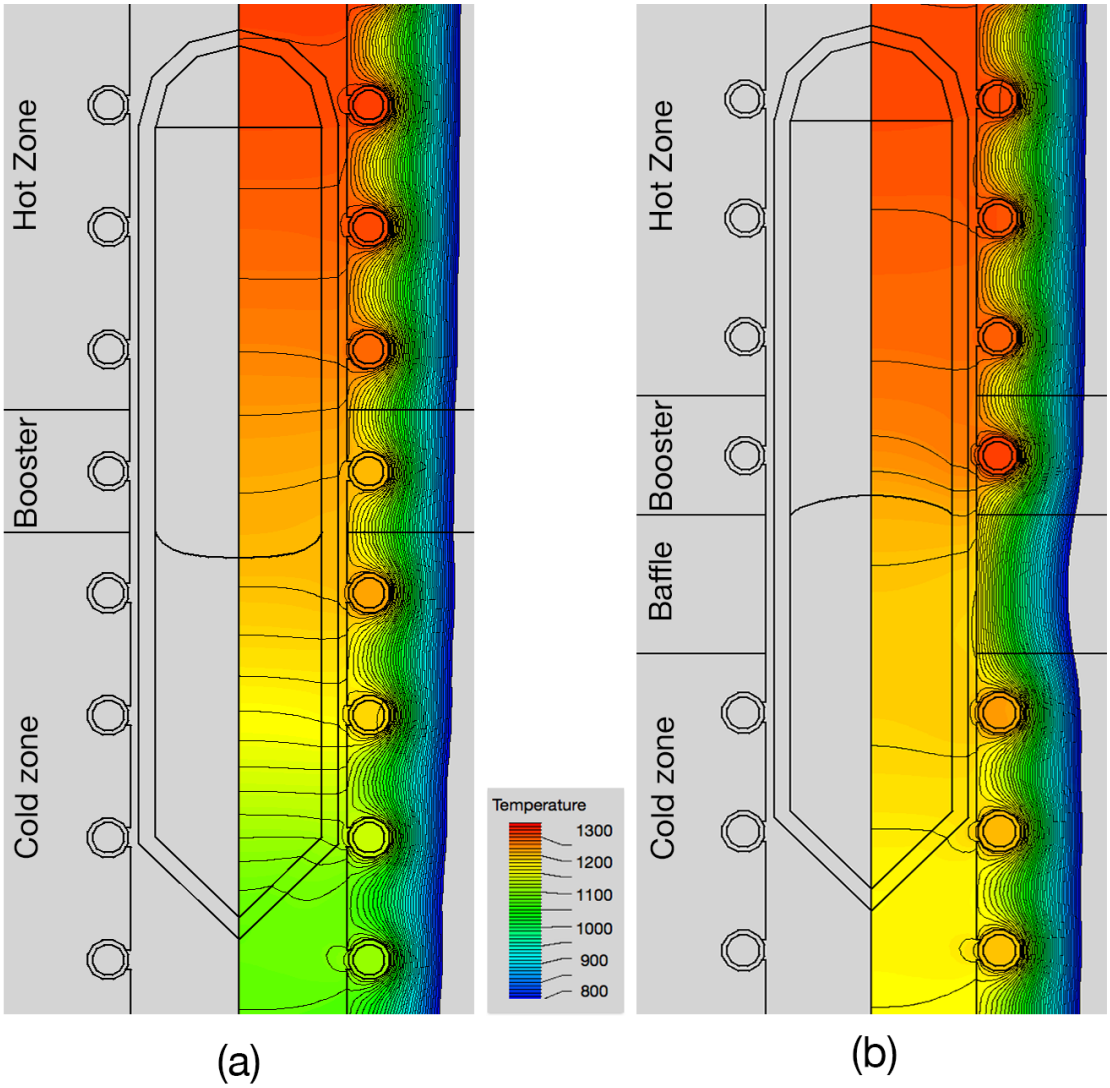

Figure 6.4: Two designs for a four-zone Bridgman with temperature isotherms plotted on the right side of each image. In (a), the furnace design incorporates a booster heater but also shows a concave growth interface. By adding a baffle zone below the booster heater in (b), the interface has been transformed from concave to convex.

the existence of the booster zone, the interface adopts a concave shape; this is despite of the fact that the liquid has a lower thermal conductivity than the solid, which would tend to promote a convex interface. In this case, the heat transfer within the furnace has completely overwhelmed the natural tendency of the interface to be convex. Looking carefully at the temperature field, it is apparent that the booster heater is only providing a small amount of heating and is, in fact, slightly cooler than the adjacent melt. As a result of this design and the choice of heater set-points, the booster zone is actually acting as a heat sink, drawing heat away from the ampoule and promoting a concave interface.

As was discussed in section 6.2, the challenge with a booster is not the adding of heat but finding a way to remove it. In order to incorporate the booster heater without changing the set-points, heat must be removed directly below the growth interface. This was accomplished in a modified design by adding a small baffle zone immediately below the booster heater, as seen in Fig. 6.4(b). With the introduction of the baffle, the interface shape switches from concave to convex and the booster heater is now much hotter than the adjacent melt.

Intriguingly for this case, the shape of the growth interface can be inferred by simply considering the temperature profile within the empty furnace, without the full calculation of heat transfer within the ampoule. Fig. 6.5 plots the centerline axial profiles of the two furnace designs operating empty and under the same control points as used above (the hot-zone control point is located outside the area displayed in Fig. 6.4). In the case of the original design with a booster alone, the axial thermal profile exhibits positive curvature in the booster region, and this condition was shown to result in a concave interface. The modified design featuring a booster and baffle, however, provides an axial profile that has negative curvature above the melting point and that gives rise to a convex interface during growth.

6.4 Conclusions

Using simple heat transfer arguments, we have put forth a general criterion for determining whether a furnace design will tend to promote a convex or concave interface

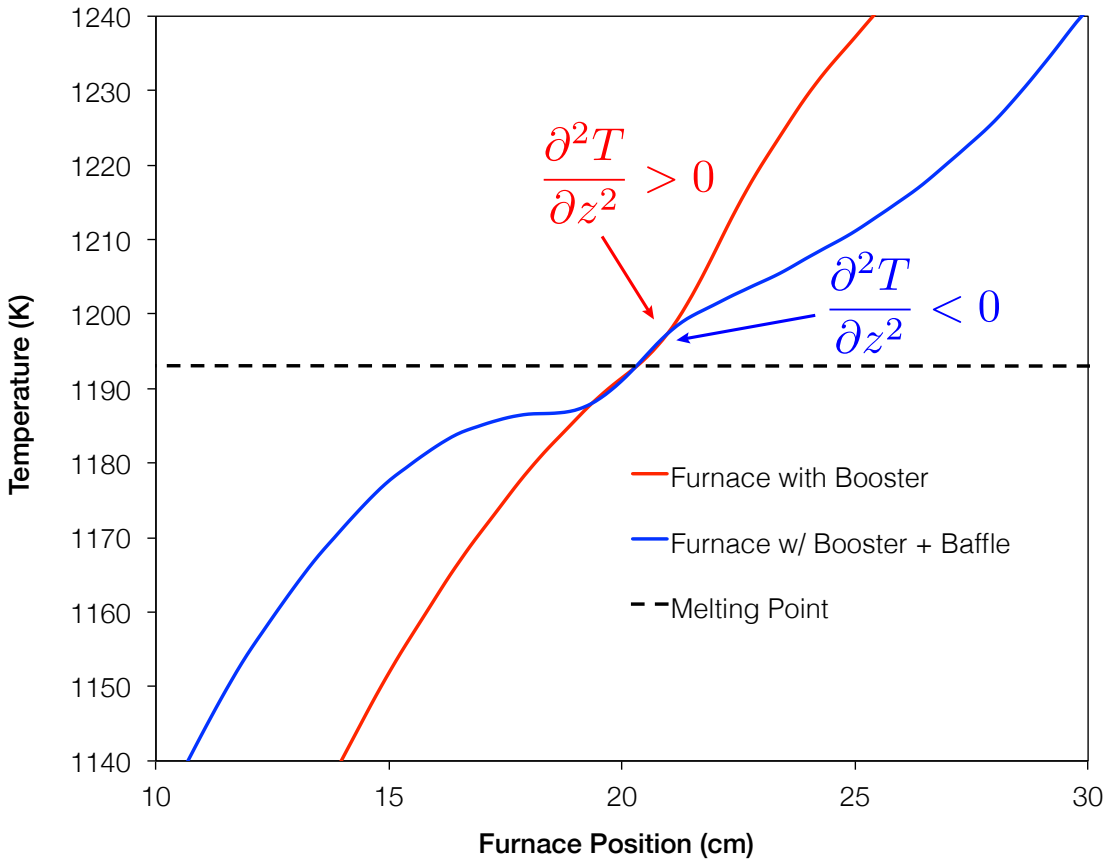

Figure 6.5: Axial thermal profiles of the two furnace designs shown in Fig. 6.4. The design with the baffle produces a region of negative curvature in the profile around the melting point.

shape. We posit that attaining a convex melt-solid interface requires an axial temperature profile through the growth furnace that exhibits negative curvature, $\mathrm{d}^2T/\mathrm{d}z^2 < 0$, above the melting point of the crystal.

As demonstrated above, this criterion works well to reinterpret prior results on interface control and to understand postulated furnace designs for the growth of mixed-halide, scintillator crystals. Interestingly, the results suggest that the negative curvature criterion may be valid even for the case of an empty furnace. Thus, a simple, open-bore axial temperature measurement may provide insight about a furnace's suitability for convex interface growth, without growing a crystal or conducting simulations.

While the derivation presented above ignores phenomena that are known to contribute to concave interface shapes, such as melt convection, adverse thermal conductivities, and the release of latent heat, the concept behind our criterion remains valid when these additional factors influence system behavior. Namely, the magnitude of the negative curvature of the axial thermal profile above the melting point is a measure of the amount of inward radial heat flux that is available to overcome other factors and influence interface shape. Thus, we believe that this idea can be universally applied toward engineering desired, convex interface shapes in Bridgman-like crystal growth processes.

Chapter 7

Concluding Remarks

7.1 Summary of thesis and discussion of results

Over fifty years has passed since the traveling heater method was first proposed as a technique for the growth of high quality crystals and nearly as much time has been spent using mathematical models to gain further understanding. However, the growth method has only recently seen more wide-spread adoption for the growth of CZT even though many of the fundamental aspects of the system are not well-understood. Part of this is due to the incomplete or incorrect models that have been used in investigating the system, and so we present here and in other works [90] what we believe is the most complete mathematical treatment of the THM system.

Using this model, the fundamental physics in the THM system were identified in chapter 4 to better understand how the system behaves under a variety of different conditions. We demonstrated that the strong interplay between temperature, flow, and concentration leads to an extremely non-linear system that is difficult to characterize without modeling. The extremely non-linear flows in the THM system lead to surprising effects including the evolution of additional flow cells and an interface morphology that defies the simple notions of concave or convex. Within the context of needing to scale up growth of CZT, we have also demonstrated that these non-linearities only increase as the system gets larger. Indeed, future work on larger systems may require a time-dependent 3-D model to fully capture the dynamics of a large system. Our work has also demonstrated the dire need for physical properties in the context of technological

development. New materials are discovered on a regular basis with properties that could revolutionize entire industries but the path from lab-scale to production-scale is fraught with challenges. Models such as ours can help in understanding the fundamental aspects of the system, but a more detailed analysis requires a more accurate knowledge of the physical properties in the system.

In chapter 5, we were able to understand the non-linear flows of the THM system using ideas borrowed from atmospheric science. In this thesis and associated works [90, 68], we have been the first to identify lee waves in the THM system while also being able to characterize their evolution using the Brunt-Väisälä frequency and characterize their shape using an understanding of the Kelvin-Helmholtz instability. Most importantly though, we were able to link the formation of these lee waves to constitutional supercooling at growth rates well below the classical limit demonstrated by Tiller [82]. We propose that it is this supercooling that is responsible for the slow growth rates exhibited by the THM system and posit that the supercooling leads to a morphologically unstable growth interface and poor crystal quality. Classically, supercooling is alleviated by simply increasing the thermal gradients at the interface, but our analysis suggests that such a strategy will serve to increase the strength of the lee wave, thereby increasing tellurium accumulation. As a result, our model predicts that a new strategy is needed in order to increase growth rates in the THM system; such strategies will be discussed later in this chapter.

In addition to the work on the THM growth of CZT, chapter 6 discusses a strategy for interface control in Bridgman processes. While many *ad hoc* techniques have been presented for interface control in such systems, none were truly generalizable for the design of actual furnaces. Our temperature profile curvature criterion provides a method by which a furnace design can be evaluated for its ability to produce a convex interface even without considering the crystal growth whatsoever. Specifically, we generalize the results from previous efforts to show that when the axial thermal profile exhibits negative curvature, i.e. $\mathrm{d}^2T/\mathrm{d}z^2 < 0$, the heat fluxes will tend to promote a convex interface shape. This criterion can be readily applied to furnace selection where competing designs can be evaluated by simply considering the axial temperature profile; combined with heat transfer modeling, this can greatly accelerate furnace development. At present, the criterion only takes into account heat transfer but later in this chapter, further

directions will be discussed whereby the criterion can be expanded to take into account latent heat of solidification and thermal conductivity mismatches.

7.2 Directions for future work

While the work presented in this thesis answers some very important questions about the THM and Bridgman crystal growth systems, they also bring up additional avenues for research. In the THM system, we have only been able to speculate on the stability of the growth interface and have posited that the undercooled liquid would naturally lead to instability without true proof of this occurring. The first step will be to implement a criterion for interface stability that is formulated off of the well-known linear stability analysis performed by Mullins and Sekerka [32] that takes into account stabilizing influences. After assessing the interface stability in a more complete and rigorous manner, the next step is to investigate techniques for improving crystal quality through mixing of the melt. In the following sections, we will discuss current work that has been performed in understanding the effects of the accelerated crucible rotation technique (ACRT) as well as using rotating [91] and translating magnetic fields and how these techniques could be used to eliminate the supercooling caused by the lee wave flow structure. Finally, we will comment on the future directions for the axial temperature curvature criterion and interface control in Bridgman systems.

7.2.1 Interface instability

It has long been understood that the rate of solidification greatly influences the quality of the growing crystal, but even at moderate growth rates, the growth interface can sometimes lose stability and transform from a planar shape into a cellular structure. These cells tend to produce liquid inclusions that lead to detrimental material properties, compromising performance in the end application. In 1953, Rutter and Chalmers [70] connected a cellular structure with the existence of constitutional supercooling in front of the growth interface. As was explained in chapter 5, the supercooling arises as solvent is rejected at the growth interface to the point where the concentration-dependent melting point actually exceeds the local temperature in the adjacent liquid. When the supercooling is present and ignoring all other effects, the growth interface will become

morphologically unstable.

However, constitutional supercooling is not the only factor that affects interface stability. In their seminal work, Mullins and Sekerka [32] used a linear stability analysis to arrive at a stability criterion that included interactions between the composition and temperature fields as well as surface energy of the growth interface. But even when the stabilizing effects of surface energies are neglected, Mullins and Sekerka showed both that an interface could be stable with undercooling and unstable without any undercooling due to the effects of latent heat and thermal conductivities. Without accounting for surface energy effects, the classic stability criterion developed by Mullins and Sekerka is

$$\begin{aligned} -\frac{1}{2}(\mathcal{G}' + \mathcal{G}) + mG_{\mathrm{c}} < 0 \quad &\text{stable} \\ > 0 \quad &\text{unstable} \end{aligned} \tag{7.1}$$

where m is the slope of the liquidus line and G_{c} is the concentration gradient in front of the interface. The symbols $\mathcal{G}$ and $\mathcal{G}'$ represent scaled thermal gradients given by

$$\mathcal{G} = G\frac{k_{\mathrm{L}}}{\bar{k}}, \quad \mathcal{G}' = G'\frac{k_{\mathrm{S}}}{\bar{k}} \tag{7.2}$$

where G is the thermal gradient in the liquid, G' is the thermal gradient in the solid, k_{L} is the thermal conductivity of the liquid, k_{S} is the thermal conductivity of the solid, and $\bar{k} = \frac{1}{2}(k_{\mathrm{L}} + k_{\mathrm{S}})$ is the average of the two thermal conductivities. By equating like Fourier terms in their linear stability analysis, Mullins and Sekerka also showed that this criterion can be rewritten as

$$\begin{aligned} (-G + mG_{\mathrm{c}}) + G\left(\frac{k_{\mathrm{S}} - k_{\mathrm{L}}}{k_{\mathrm{S}} + k_{\mathrm{L}}}\right) - V\left(\frac{L}{k_{\mathrm{S}} + k_{\mathrm{L}}}\right) < 0 \quad &\text{stable} \\ > 0 \quad &\text{unstable} \end{aligned} \tag{7.3}$$

to incorporate the effect of the latent heat of fusion per unit length, L, and the growth rate, V. The first term in parentheses is the now familiar effect of constitutional supercooling and is destabilizing as the concentration gradient increases. The third term incorporates the effect of latent heat and is always negative, thereby stabilizing the interface. Interestingly, the second term tells us that the interface will tend to be stabilized when the thermal conductivity of the liquid is greater than the solid but not in the reverse case. To understand why this effect arises, we must analyze the heat fluxes and how they affect the shape of the interface.

Consider a planar interface with an instantaneous perturbation applied to it in a linear thermal field with heat fluxes traveling from top to bottom such as that in figure 7.1 (a). All things being equal, we would expect the interface to return to a flat shape in order to lie along the melting point isotherm that is perpendicular to the vertical heat flux lines. If instead, something is driving the instability and the peaks of the waves are advancing, we would expect them to release latent heat as they grow. The effect then would be to rearrange the heat fluxes so that they resemble figure 7.1 (b). If an isotherm is plotted perpendicular to the heat flux lines (blue dashed line), we see that the isotherm will be exactly out of phase with the initial perturbation. In other words, the peaks will become hotter and the valleys will be colder, thus providing a mechanism to shrink the instability.

Similarly, we can apply the same analysis for the perturbation but this time thinking about the effect of the thermal conductivity ratio. If the solid has a higher thermal conductivity than the melt, the solid will represent less resistance to heat transfer and in a 2-D space, heat fluxes will tend to bend towards solid material and away from the melt. This will then produce an isotherm that is in phase with the original perturbation and will tend to cause the instability to grow. Conversely if the liquid thermal conductivity is higher than the solid, the heat flux will be diverted towards the melt valleys which will tend to form an isotherm exactly out of phase with the original perturbation. These two situations are schematically shown in figure 7.2.

In the THM growth of CZT, our temperature solutions include the effects of latent heat and thermal conductivity natively so equation 7.1 can be used to assess stability of the interface in the presence of constitutional supercooling. Since the melt is more thermally conductive than the solid, we expect that a certain amount of undercooling will be tolerable without seeing the interface become unstable. The next obvious step in this research is to use the Mullins-Sekerka stability limit to evaluate our previous calculations for interface stability. Indeed, we have seen that only certain growth rates lend themselves to steady state solutions and the loss of solution existence could be explained by an interface becoming unstable. Compared to simply analyzing the amount of undercooling present in the system, the Mullins-Sekerka criterion should prove a more robust means of evaluating the success of various techniques that have been proposed for increasing growth rates. Eventually, we will likely need to also consider surface

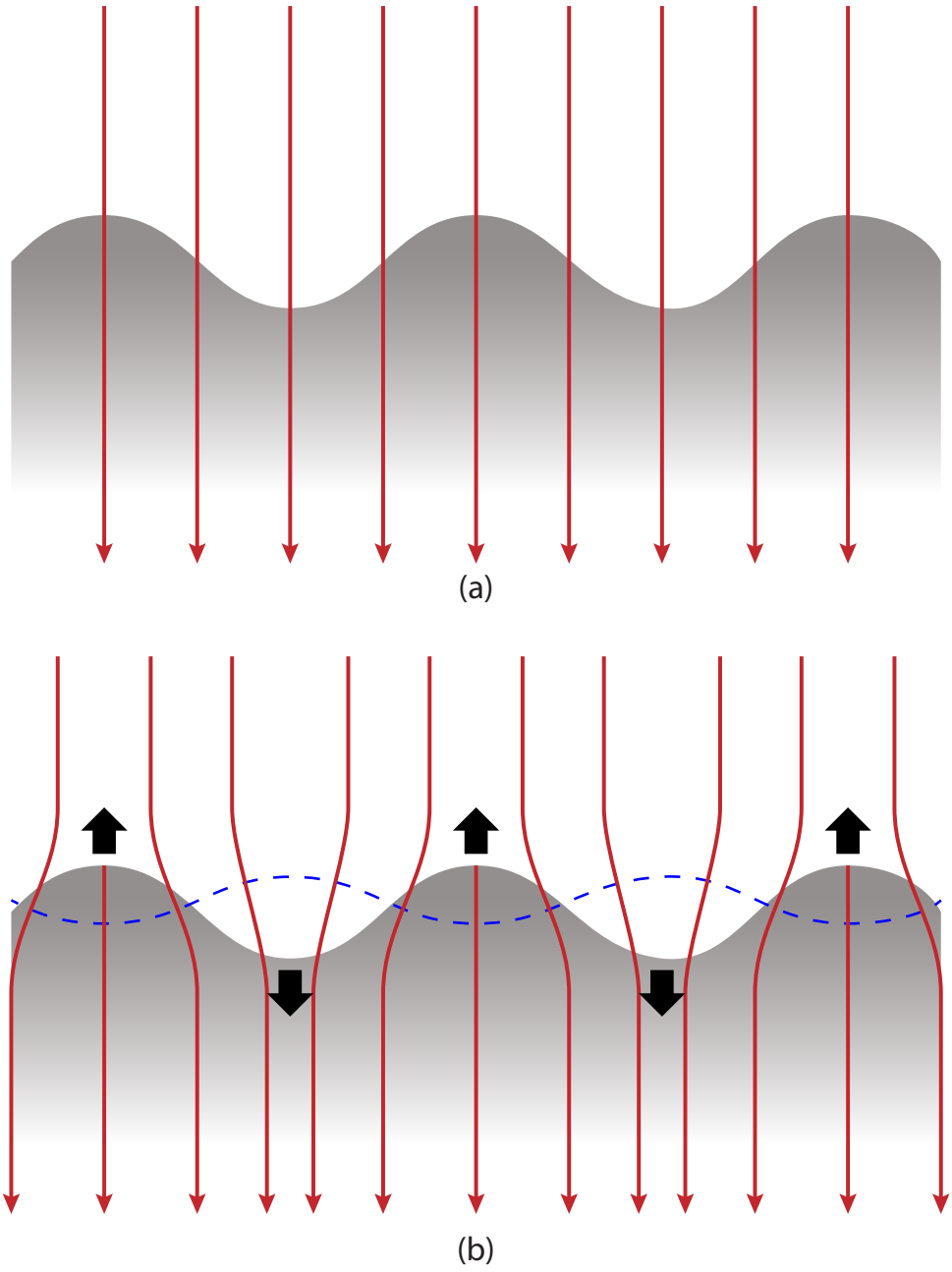

Figure 7.1: Heat flux lines for a linear temperature field with a perturbed interface both excluding (a) and including (b) the effect of latent heat. If the perturbation is growing, latent heat will be released at the perturbation peaks and will distort the thermal field such that the heat flux lines resemble the situation shown in (b). The resulting melting point isotherm will then be exactly out of phase with the initial perturbation, causing the interface to return to a planar configuration.

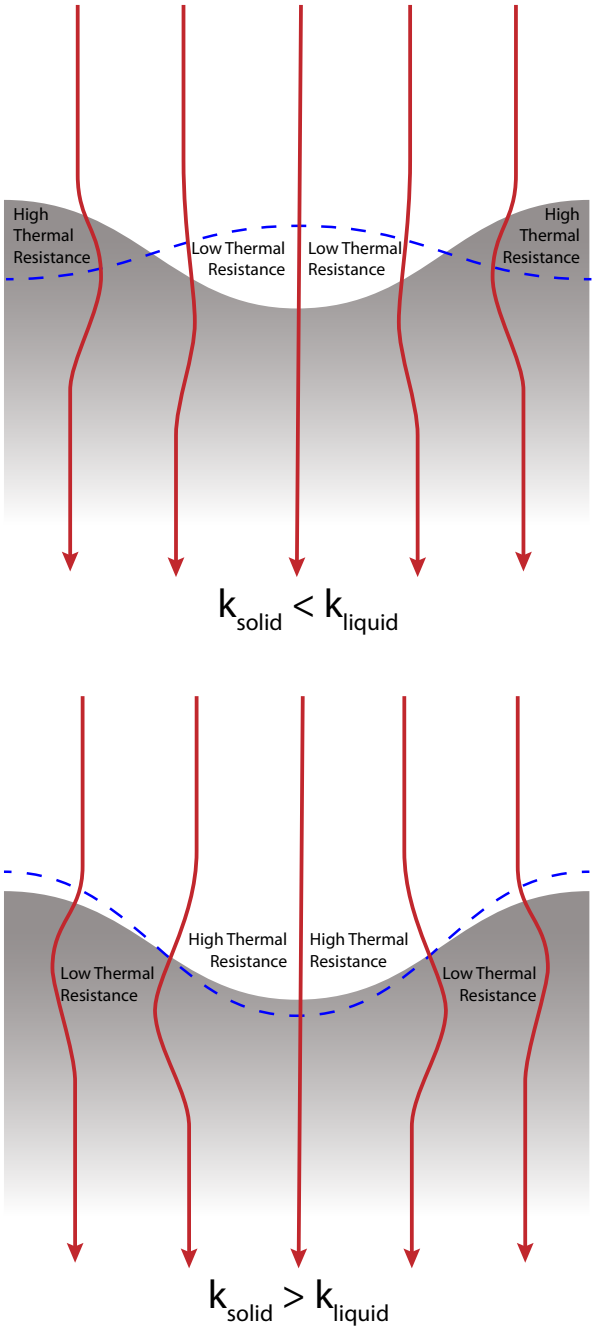

Figure 7.2: A higher solid thermal conductivity will favor heat flowing more through the solid than the melt, diverting the heat fluxes so that the resulting isotherm is in phase with the original perturbation. Conversely, the isotherm will be out of phase with the original perturbation when the melt has a higher thermal conductivity.

energy effects to compute the modified equilibrium melting point temperature. With increasing curvature comes higher surface energies that inhibit the formation of new solid and thereby lower the effective melting point, a phenomena known as the Gibbs-Thompson effect.

7.2.2 Use of accelerated crucible rotation technique (ACRT) to eliminate lee waves

Our analysis of the THM growth of CZT crystals has yielded an important result: the formation of lee waves inhibits the transport of excess tellurium away from the solidification interface and leads to a constitutional supercooling in the liquid ahead of the growth front. We believe this is the limiting factor in THM growth of CZT and is responsible for the reported growth rates in the literature of only a couple millimeters per day [16, 15, 14, 13, 17] when the growth rate limit proposed by Tiller [69] is many times this limit. Now that this mechanism has been identified, the appropriate question to ask is how to alleviate it.

Since the underlying mechanism for constitutional supercooling is mass transport, the logical solution is one that disrupts the natural transport mechanisms in the THM system. One such possible solution is the accelerated crucible rotation technique (ACRT) [92, 93] that has been modeled in Bridgman and Vertical Gradient Freeze systems [94, 95, 71] and is used to enhance homogenization in the melt. Yeckel and Derby [71] gave a particularly complete explanation of the flows involved in an ACRT cycle and highlighted some considerations needed when designing an ACRT cycle. However, there have been far fewer studies on the application of ACRT to the THM and related systems [96, 97] and these studies have not focused on the effects of mass transport.

The central idea in the application of ACRT is to cyclically interrupt the natural buoyancy-driven flows in the system to better mix the liquid zone. Two particular flows arise that are of interest during an ACRT cycle: Ekman flows and Taylor-Görtler flows and both are shown in figure 7.3. Ekman flows are created when the system first is accelerating. The fluid closest to the interface is accelerated and flows outwards due to the centrifugal force just as in a centrifugal pump. The pumping action continues throughout the acceleration phase but weakens as the system approaches solid body rotation; the time required for the system to achieve solid body rotation is characterized

by the Ekman timescale. During deceleration, the rotation rate decreases and from the perspective of the rotating fluid, the solid surfaces will appear to be moving in the opposite direction. As a result, the flows near the interface reverse since the faster rotating fluid seeks to be outside of the slower-rotating fluid immediately in front of the growth interface. Meanwhile, flows can appear at the ampoule surface where the slower-moving flow in contact with the ampoule seeks to switch positions with the faster-moving flow in the bulk of the fluid. This rearrangement results in a series of stacked vortices at the edge of the liquid zone that are called Taylor-Görtler vortices.The net effect of these time-dependent flows as identified by Yeckel and Derby [71] will be to disrupt the existing concentration boundary layers, enhance mass transport in the fluid, and homogenize the composition field in general. With our recent discovery of lee waves in the THM system, we would expect the application of ACRT to first disrupt the formation of the lee wave and second to decrease gradients in the liquid zone soas to reduce the danger of constitutional supercooling. However, our initial work has showed that this naive understanding is too simplistic for such a complex system.

To begin such an analysis of the effectiveness of ACRT, we first need to develop a metric by which to judge improvement in the system. Since constitutional supercooling is our hypothesized mechanism for detrimental crystal effects at high growth rates, we have up until this point simply looked for the presence or absence of constitutional supercooling as an indicator for crystal quality. Given the time-dependent nature of ACRT however, we now must ask whether the time-fluctuating presence of supercooling is enough to produce an unstable interface. Naturally, this requires the use of the Mullins-Sekerka criterion that was outlined in the previous section. Mullins and Sekerka [32] began their linear-stability analysis by first analyzing the normalized growth rate of an instability under a given set of process conditions. Before deriving their important criterion in equation 7.1, they first derived an expression for the rate, $\dot{\delta}$, at which an instability of wavelength ω would grow with respect to its amplitude, δ,

$$\frac{\dot{\delta}}{\delta} = \frac{2V\omega\Big(\omega^* - (V/D)(1-k)\Big)\Big[- T_{\mathrm{mp}}\Gamma\omega^2 - \frac{1}{2}(\mathcal{G}' + \mathcal{G}) + mG_{\mathrm{c}}\Big(\frac{\omega^* - (V/D)}{\omega^* - (V/D)(1-k)}\Big)\Big]}{(\mathcal{G}' - \mathcal{G})\Big(\omega^* - (V/D)(1-k)\Big) + 2\omega m G_{\mathrm{c}}}, \tag{7.4}$$

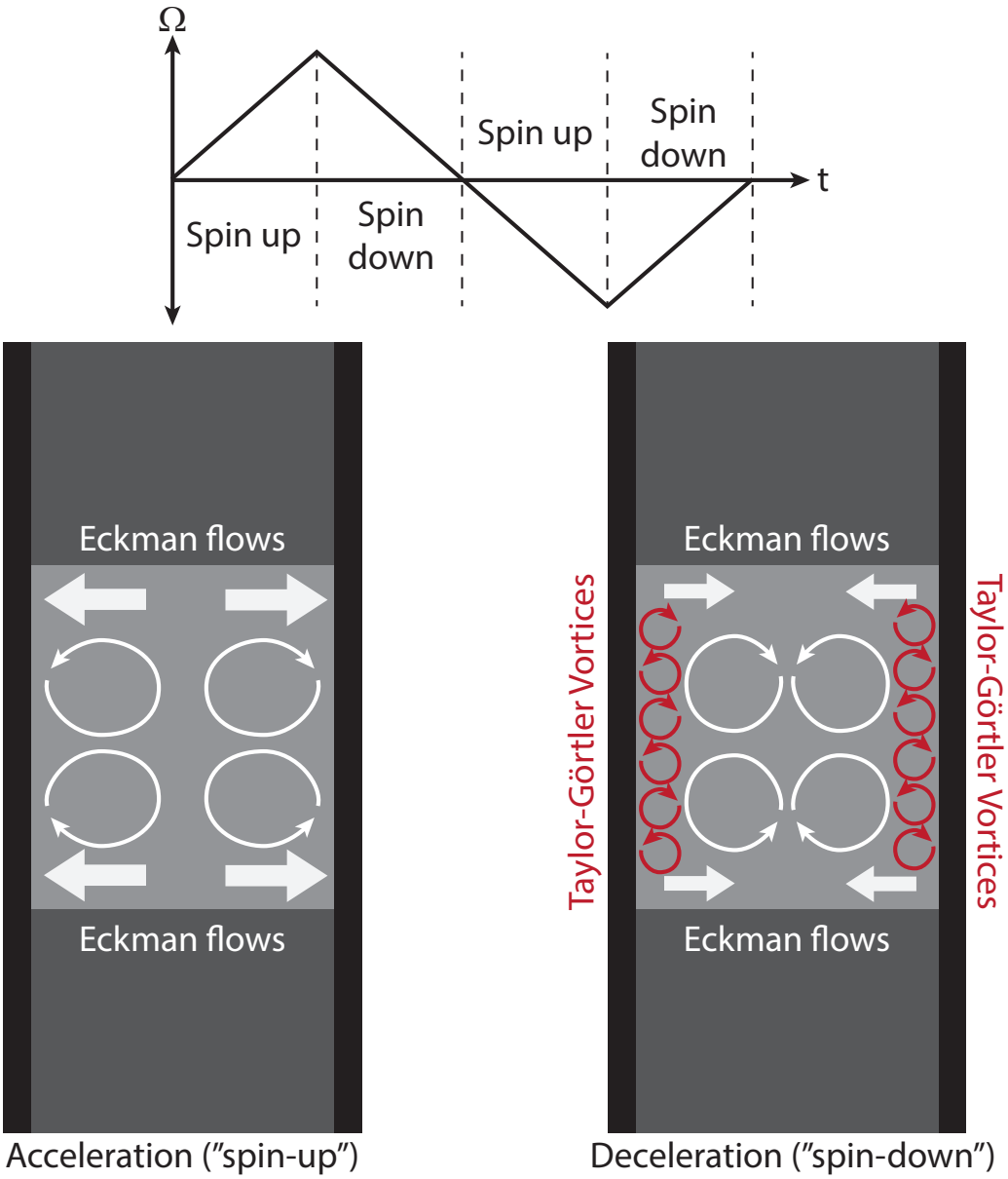

Figure 7.3: Schematic representation of an ACRT cycle with Ekman flows and the vortices they cause shown in white. Taylor-Görtler vortices appear at the edges of the melt zone near the ampoule wall during the deceleration phase.

where the interested reader is directed to the original work by Mullins and Sekerka [32] for definitions of symbols not already defined here.

We can also rearrange equation 7.1 to reframe the criterion as

$$\frac{mG_{\mathrm{c}}}{\frac{1}{2}(\mathcal{G}' + \mathcal{G})} = \frac{mG_{\mathrm{c}}}{\frac{Gk_{\mathrm{L}}+G'k_{\mathrm{S}}}{k_{\mathrm{L}}+k_{\mathrm{S}}}} = \begin{array}{ll} \mathrm{Sk} < 1 & \text{stable} \\ > 1 & \text{unstable,} \end{array} \tag{7.5}$$

where Sk is a dimensionless group that is defined as the Sekerka number [98]. The important conclusion from the numerator of equation 7.4 is that if the quantity in the brackets is positive, the instability will grow with time whereas if it is negative, the instability will shrink. Mullins and Sekerka go on to demonstrate that if surface energy effects are small, the sign of equation 7.4, and hence stability, will be solely determined by equation 7.1 and thus whether Sk is greater or less than one. Given a perturbation of some wavelength, we may then assume that the rate at which an instability grows will be roughly proportional to the Sekerka number minus one or

$$\dot{\delta} \propto \mathrm{Sk} - 1. \tag{7.6}$$

Of course, a more desirable metric would directly equate the growth rate of the instability to the state of the system. Indeed, the assertion of direct proportionality is probably wrong due to non-linear effects, but within a small range of values it should provide at least an acceptable starting-point.

Using the Sekerka number as an indicator for stability, we can extend this concept within the context of an ACRT cycle. We anticipate that there will be times during an ACRT cycle where $\mathrm{Sk} > 1$ and thus the interface is unstable, but we must also consider the timescales over which a cellular interface would evolve. While the linear stability analysis of Mullins and Sekerka is insufficient to predict the interface morphology after it has gone unstable, we may assume that in many instances, the instability would evolve over multiple ACRT cycles. As a result, an interface will only be unstable if conditions in a single ACRT cycle tend to promote instability more than stability. Otherwise the interface will tend towards its flat configuration and any instabilities will be suppressed on average. A sensible extension would be to simply integrate the Sekerka number over the entire ACRT cycle,

$$S = \int_0^1 (\ \mathrm{Sk} - 1)\, \mathrm{d}t, \tag{7.7}$$

where the time is normalized to units of an ACRT cycle. However, this result is not physical because prolonged periods where Sk is less than one will cancel out future periods when Sk is greater than one. In other words, this result would allow the interface to be preemptively fortified against an instability by stable periods which is not the case. Instead, a better measure would parameterize this integral so that

$$S = \sum_{i=1}^{N} \begin{cases} s_i = \int_{t_{i-1}}^{t_i} (\,\mathrm{Sk} - 1)\,\mathrm{d}t & \text{if } S \geq 0 \\ 0 & \text{if } S = 0 \text{ and } s_i < 0 \end{cases} \tag{7.8}$$

where intervals $[t_{i-1}, t_i]$ are chosen such that s_i is always non-negative if it is added to the sum. In practice, it makes more sense to evaluate this integral at each timestep and then determine whether s_i should be added to the running sum, S, or not. This expression may appear unwieldy, but it is actually much easier to represent as a discrete algorithm (syntax is python):

```
for i in range(1, N):
        dt = time[i] - time[i-1]
        step = S[i-1] + 0.5*(Sk[i]+Sk[i-1])*dt
        if step < 0:
                step = 0
        S[i] = step + S[i-1]
```

Here the integral is performed over N timesteps using the trapezoid rule and the value of S at each timestep is stored in the vector S. The most important condition is that the integral can only be zero or positive so steps that would make the sum negative are ignored.

To introduce ACRT into the crystal growth system, we must now solve for u_θ in the Navier-Stokes equations (equation 2.4). Note that although we are now solving for velocity in three dimensions, we are not fully solving the 3-D problem. By requiring that all of the gradients in the θ-direction be zero, we preserve the axisymmetry of the system and only moderately increase the amount of computation. Introducing the time-dependent rotation rate, $\Omega(t)$ only requires specifying another term in the no-slip boundary condition, requiring that

$$u_\theta = \Omega(t) r \tag{7.9}$$

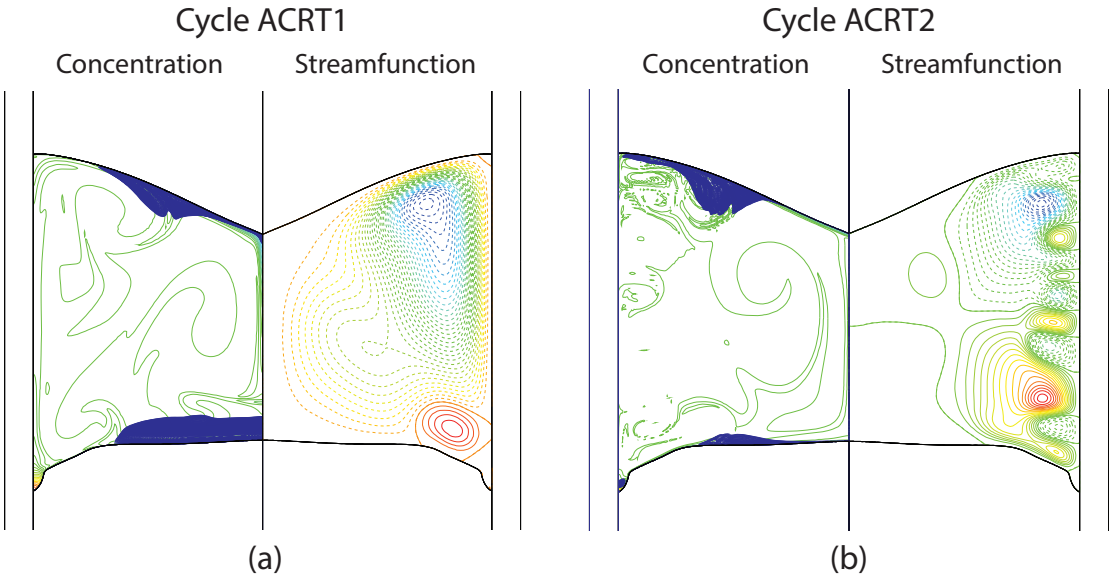

Figure 7.4: Contour plots of excess tellurium concentration and the Stokes streamfunction at a growth rate of 4.06 mm/day for two different ACRT cycles, ACRT1 and ACRT2, in (a) and (b) respectively. Undercooled melt is identified by the shaded region in the concentration contours. Positive values for the streamfunction indicate a clock-wise vortex while negative values (shown as dashed contours) represent counter-clockwise vortices. Both images represent a time 60% through an ACRT cycle after the system has reached a periodic steady state.

at any solid-liquid interfaces. The only remaining boundary condition is to guarantee symmetry by imposing $u_\theta = 0$ at the centerline.

Initial results with ACRT applied to the THM system show that undercooling is not eliminated by the mixing. After an initial transient, the system settles into what appears to be a periodic steady state after approximately five cycles. While mixing is enhanced in general, the periodic melting and solidification during the cycle does lead to significant concentration gradients near the interfaces. Importantly, the application of ACRT does not appear to eliminate the constitutional supercooling and in some circumstances it can actually exacerbate it. Take for example the images shown in figure 7.4 with two different ACRT cycles, ACRT1 and ACRT2 and undercooling indicated by the dark shaded area: the area that is undercooled in the second cycle appears to be greatly reduced while ACRT1 seems to be completely ineffective. Other portions of each ACRT cycle (not pictured) show that the undercooling largely persists at the centerline for (a)

but in (b) the undercooling travels across the entire interface such that few areas are constantly undercooled. Focusing on the perspective of undercooling, it would appear that ACRT1 would be worse for interface stability.

However, analyzing the stability through use of the Sekerka number reveals that much of this undercooling may in fact be stabilized. Figures 7.5 (a) and (c) (corresponding to cycles ACRT1 and ACRT2 respectively) show only unstable Sekerka numbers (Sk $>$ 1) plotted as a function of position on the horizontal axis and time on the vertical axis. Because the values are plotted as a function of r^2 instead of r, each point in time shows the area of the interface that is feeling a stabilizing or destabilizing influence. Again, only values of the Sekerka number greater than one are plotted so any white regions represent a time and position where the interface is stabilized. Simply by looking at the amount of blank space on each plot, we see that although ACRT1 may have produced more undercooling, ACRT1 appears to produce an interface that is actually more stable than that for ACRT2.

To analyze the cumulative effect of interface stability over the entire ACRT cycle, we can take the Sekerka number and integrate it via equation 7.8. The result then is an indication of the cumulative effect of stabilizing and destabilizing influences in the system over a single ACRT cycle. If this integral is zero, then the stabilizing effects are more prevalent while any positive result indicates that destabilizing effects have dominated. Figures 7.5 (b) and (d) show the Sekerka number integrated over time in exactly this manner for cycles ACRT1 and ACRT2 respectively. For these plots, the absolute values of the scale are not important except for in comparison between the two systems. Areas where there is no contour gradient (shown in dark blue for color prints) indicate positions and times where the interface would be expected to be more or less flat. Contours are a rough measure of how large an instability has gotten at that point in time. We see in (d) that even if there are periods of stabilizing influences during the cycle, they are overwhelmed by the times where the interface is unstable. Graphically, we understand this because the integral instability value is increasing over the entire ACRT cycle, which means that subsequent cycles will only exacerbate any instability. By contrast, (b) shows a more cyclical result where any instability will grow but then shrink again until a flat interface again appears. This analysis assumes that the rate of instability growth–and by association the rate of instability suppression–is proportional

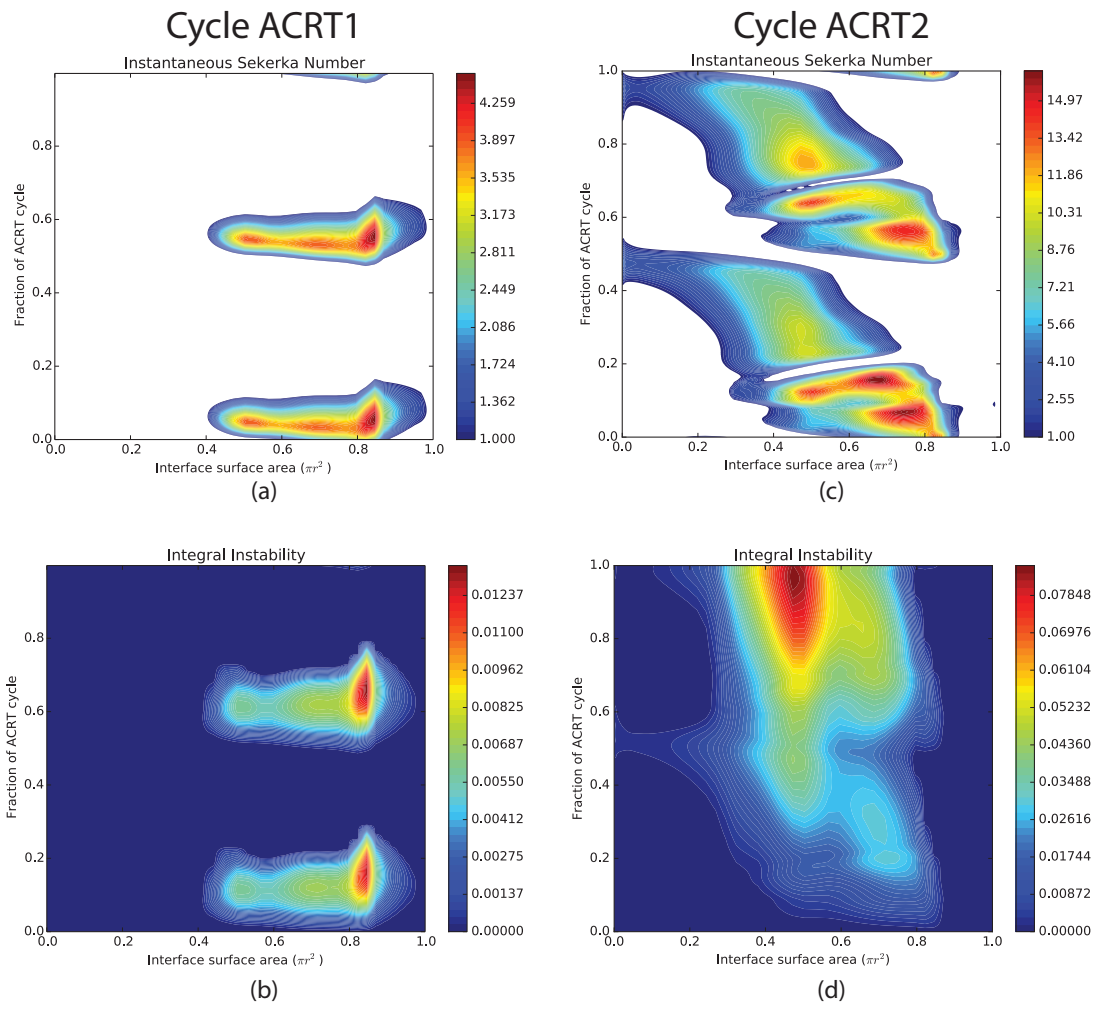

Figure 7.5: Contour plots showing interface stability. On each plot, time is plotted on the vertical axis while the radius scaled by the surface area is plotted on the horizontal axis. Figures (a) and (c) are produced by measuring the instantaneous Sekerka number given by equation 7.5 where white space indicates a stabilizing environment at that position and time. Figures (b) and (d) represent cumulative effect of destabilizing influences over time given by equation 7.8; contours are then a rough measure of how large an instability has grown on the interface. Sub-figures (a) and (b) correspond to the ACRT1 cycle of figure 7.4 (a) while sub-figures (c) and (d) correspond to ACRT2 in figure 7.4 (b).

to the value of the Sekerka number. The large areas of the plot in (b) that are zero are a reflection of this idea and if these oscillations occur on a timescale that is much faster than the instability growth, we would expect few deleterious effects from the brief periods of instability.

One of the primary mechanisms by which an unstable interface can be detrimental to CZT crystal quality is through a process of creating liquid inclusions. Phase field calculations by Meca and Plapp [99] have shown that a bifurcation exists at a certain amount of undercooling for an unstable interface. Before this bifurcation, the instability can be metastable with cells at a specific amplitude and wavelength. As the undercooling is increased, the system passes through a Hopf bifurcation where the the shape of the cell oscillates between states where the cell tip is either sharp or flat. When the cell is flattened, the grooves between adjacent cells become very narrow and, in a process analogous to the Rayleigh instability, the narrow groove breaks down to form a liquid droplet inclusion. Unfortunately, Meca and Plapp state that the critical amount of undercooling required before the interface begins to oscillate is a function of interface thickness, a parameter in their phase field simulation. They point out that while the size of the cells is approximately 100 µm, the interface thickness is five orders of magnitude smaller. Because such disparate length-scales are not practically simulated with current computational resources, the interface thickness parameter in the model is chosen to be much larger. As a result, it would be difficult to say with certainty whether a given amount of undercooling would drive an unstable interface that actually produces liquid inclusions. Meca and Plapp do mention though that the timescale for droplet formation is on the order of a few diffusion times. If this period is longer than the length of time the interface is unstable in our system, it is plausible that no liquid inclusions would be formed.

While these calculations are only preliminary, they begin to cast the issue of interface stability in a new light. First, they reveal that the distinction between morphological instability and constitutional supercooling is not trivial. In fact, our initial results seem to indicate that the presence of undercooling can actually be a very misleading indicator when it comes to evaluating interface stability during transient flows. The next step will be to verify the mechanism responsible for stabilizing the interface in the presence of such extensive undercooling. While the analysis of Mullins and Sekerka [32]

provides a starting point, the transient nature of the temperature field also requires a careful analysis. Since our current model assumes that the interface is at all times in thermodynamic equilibrium, it may also be appropriate to re-examine this assumption and investigate the system from a non-equilibrium point of view. Furthermore, care must be taken to ensure that these results are not somehow related to the choice of timestep; with such fast and non-linear flows, the choice of timestep could influence the solution.

Once the main driving forces for stability and instability have been identified, the next step will be to design a set of guidelines for designing an ACRT cycle that best stabilizes the interface despite undercooling. The traditional wisdom is that an ACRT cycle that promotes Taylor-Görtler vortices will best mix the melt and consequently will lead to the best growth conditions. However, the two cycles that have been presented in this thesis contradict this assumption. Both of the plots of the Stokes streamfunction in figure 7.4 represent a state that is 60% through a given ACRT cycle, which is at the end of the deceleration phase and exactly where the Taylor-Görtler vortices would normally form. Indeed, in figure 7.4 (b), these vortices are clearly shown at the periphery of the melt zone near the ampoule wall but they are not present in figure 7.4 (a). While we have not yet examined the exact link between these vortices and interface stability, our initial analysis (including data not presented here) seems to suggest that an ACRT schedule designed to promote Taylor-Görtler vortices may not be the best for promoting interface stability.

Our initial hypothesis is that the outward Ekman flow is primarily responsible for decreasing concentration gradients in the system. During the deceleration phase, however, the flow reverses (see figure 7.3) and a wave of excess tellurium is pushed along the interface. This effect is best seen in a sequence of images, but it is also visible where the sharp tip of the plume at the front of the wave can be seen bending outwards in the concentration contour plots. As the wave sweeps over the interface, it runs into the fluid at the centerline and with nowhere to go, the wave pushes much of the excess tellurium into this area, causing a large amount of undercooling. Therefore, we hypothesize that the best ACRT cycle will be one that lengthens the acceleration time while minimizing the amount of time spent decelerating, and thus minimizing the effect of this deceleration wave. More simulations are needed to verify this hypothesis and understand the

underlying mechanisms that lead to a successful ACRT strategy.

7.2.3 Magnetic fields in the THM system

While the accelerated crucible technique represents a method of mechanical stirring to improve mass transfer in the liquid, electromagnetic stirring can also be used in crystal growth systems. Since the heating element in most furnaces is composed of wire coils wrapped in a helical geometry surrounding the ampoule, often they can easily modified through use of a controlled AC current to produce a magnetic field in the melt. Electromagnetic stirring methods are distinctive from mechanical methods in how their respective forces act upon the fluid; while a mechanical method such as ACRT is imposed through a velocity boundary condition, electromagnet stirring introduces additional body forces to the Navier-Stokes equations. As a result, the flows created by these two methods are also very different.

In general, magnetic stirring techniques either take the form of rotating magnetic fields (RMF) or traveling magnetic fields (TMF). Since the fields are time-dependent, they will induce electric currents in the melt and the interaction between this current and the magnetic field will produce the well-known Lorenz force. A RMF is typically created through applying a time-dependent field in the radial and azimuthal directions at a fairly high frequency. If the skin-depth of the magnetic field, $\delta = (\mu_{\mathrm{M}}\sigma\omega)^{-1/2}$, is much larger than the radius of the ampoule, the Lorenz forces can be time-averaged so that a steady-state solution can be found. Here μ_{M} is the magnetic permeability of the material, σ is the conductivity, and ω is the frequency. Just as in ACRT, the body forces exist in three dimensions and so we can solve the problem in axisymmetric coordinates by assuming that all gradients in the azimuthal direction are zero. By contrast, application of a TMF makes use of the existing heating coils to produce a time-dependent magnetic field. If each coil is independently-controlled, a carefully-calibrated AC current can be used such that a position-dependent phase shift exists between each subsequent coil. As a result of these phase shifts, a traveling wave will be formed in the magnetic potential that travels down the length of the ampoule. Again, the resulting Lorenz force can be time-averaged and added as a body force term in the Navier-Stokes equations. Additionally, a Joule-heating term must be added as a source term in the energy equation. For more information on the specifics of the mathematical

implementations of these models, the interested reader is referred to the work by Yeckel and Derby on TMF [100] and that by Barz on RMF [26] with the note that the full RMF equations can be solved in our model here, rendering some of the simplifications by Barz unnecessary.

We have already studied some of the effects of RMF on the THM method in the work by Li, Peterson, Yeckel, and Derby [91] for this exact system. These initial results showed that a 10 mT magnetic field drives a strong azimuthal flow that then also leads to a secondary flow in the form of two toroidal vortices. This structure is very similar to that seen in the deceleration phase of the ACRT cycle because the underlying mechanisms are also very similar. Recall that during the acceleration phase of an ACRT cycle, the fluid has achieved solid-body rotation. During the deceleration phase, the flows are characterized by fast moving fluid moving to the outside while the slower-moving fluid at the decelerating interface moves inwards. In the application of RMF, the same situation occurs since the bulk of the fluid is rotating due to the magnetic field while the solid interfaces remain stationary.

However, the flows due to the rotating 10 mT field were fairly weak and only demonstrated a strong influence on convection under microgravity conditions. In full gravity, we would predict that the magnetic field would not so much produce new flows so much as it will rearrange some of the existing flows. Since the flow along the growth interface due to RMF is inwards as opposed the the natural outwards flow due to buoyancy effects, we would also predict that the application of RMF might actually strengthen the lee wave vortex and further increase the danger of constitutional supercooling. Another option for the use of RMF then might be to use accelerated rotation along with the magnetic field (aRMF). By switching the rotation direction, other effects might arise that better mix the melt without enhancing the lee wave vortex.

Yeckel and Derby [100] have produced a thorough review on the application of TMF for various vertical gradient freeze (VGF) systems. They show that the primary action is to produce a single large toroidal flow cell in the melt with liquid rising at the centerline and falling along the ampoule. Again, this is the opposite direction of buoyancy-driven flow in the THM system and so it is unclear whether this would be beneficial. Additionally, Yeckel and Derby show that the effect of TMF on CZT growth is minimal due to the poor electrical conductivity of liquid CZT. In the THM system

however, this may not be an issue since the tellurium-enriched melt is much more highly conductive and is theorized to exhibit metallic character [53] so the magnetic field may actually have a strong effect.

To our knowledge, no published reports exist on the use of traveling magnetic fields (TMF) in the THM system at present. A TMF is relatively straight-forward to incorporate into VGF systems since the heating elements themselves resemble a solenoid. However, in the THM system, the heater is necessarily much smaller in order to achieve the strong gradients necessary for alleviate constitutional supercooling. Despite this, some presentations from other researchers in the field indicate a large degree of success in achieving higher growth rates and better crystal quality using TMF in the THM system [101]. We believe that a thorough mathematical treatment is required to understand whether TMF could provide a suitable method for improving the THM system.

7.2.4 Generalization of axial inflection point criterion in Bridgman systems to include the effects of thermal conductivity and latent heat

In chapter 6, a simple criterion was developed that allows a crystal grower to design a furnace in order to promote a convex interface shape. The criterion was fundamentally based on a simple mathematical analysis of heat flows in the system but neglected the effects of latent heat and differing thermal conductivities. Latent heat production at an interface will always tend to promote a concave interface since the latent heat naturally increases the temperature along the centerline and produces a negative radial temperature gradient. Similarly, if the liquid is more thermally conductive than the solid, the heat flux lines will tend to diverge at the liquid solid interface; axial heat flux is resisted by the solid and redirected in a radial direction. Both processes lead to *escaping* heat at the growth interface, a situation that the booster heater is designed to compensate. In this sense, a higher *degree* of negative curvature in the axial thermal profile will be needed to offset these effects.

Intrinsically, the second derivative of the axial thermal profile, $\partial^2 T/\partial z^2$, is a measure of the radial heat transfer at a point in the furnace; if $\partial^2 T/\partial z^2 < 0$, the flux is directed inwards. This also implies that the flux is proportionate to the curvature of the axial thermal profile. By equating this additional flux to the positive radial flux produced by

latent heat and mismatched thermal conductivity, we can arrive at a measure for how concave a thermal profile must be in order to promote a convex interface shape.

However, this extension was not included in the original analysis because it remains to be tested and quantified. The first step will be to develop a rigorous method for quantifying the additional outwards flux due to latent heat and thermal conductivity mismatch. The second step will be to further prove this technique by creating a more controlled "toy" model where these parameters can be adjusted and the overall effect can be measured. Since we are reducing an inherently 2-D phenomena into what amounts to a 0-D criterion, the envelope of reliability needs to also be examined and quantified. At present, the analysis here relies on purely subjective evaluations of previous literature and incomplete heat transfer calculations. We intend to assess interface curvature in a more quantitative way and use a coupled model for the furnace and ampoule to assess overall effectiveness of this technique.

Bibliography

[1] J.H. Greenberg, "P-T-X phase equilibrium and vapor pressure scanning of non-stoichiometry in CdTe", *Journal of Crystal Growth* **161**, pp. 1 – 11 (1996).

[2] Jeff Schmaltz and NASA Earth Observatory, "Wave clouds near amsterdam island", `http://earthobservatory.nasa.gov/IOTD/view.php?id=6151`, Online; accessed 9-January-2017.

[3] Nan Zhang, Andrew Yeckel, and Jeffrey J. Derby, "Maintaining convex interface shapes during electrodynamic gradient freeze growth of cadmium zinc telluride using a dynamic, bell-curve furnace profile", *Journal of Crystal Growth* **355**(1), pp. 113 – 121 (2012).

[4] "Wilhelm conrad röntgen - biographical", `http://www.nobelprize.org/nobel_prizes/physics/laureates/1901/rontgen-bio.html`, Online; accessed 8-February-2017.

[5] K. Zanio, "Semiconductors and semimetals volume 13 cadmium telluride", In K. Zanio, editor, *Cadmium Telluride* volume 13 of *Semiconductors and Semimetals* , pp. 164–209. Elsevier (1978).

[6] Ronald Nutt, "The history of positron emission tomography", *Molecular Imaging & Biology* **4**(1), pp. 11 – 26 (2002).

[7] Gopal B. Saha, "Scintillation and semiconductor detectors", In *Physics and Radiobiology of Nuclear Medicine* , pp. 91–116. Springer New York New York, NY (2013).

[8] T Takahashi and S Watanabe, "Recent progress in CdTe and CdZnTe detectors", *IEEE Transactions on Nuclear Science* **48**(4, 1), pp. 950–959 (2001).

[9] T.E. Schlesinger, J.E. Toney, H. Yoon, E.Y. Lee, B.A. Brunett, L. Franks, and R.B. James, "Cadmium zinc telluride and its use as a nuclear radiation detector material", *Materials Science and Engineering: R: Reports* **32**, pp. 103 – 189 (2001).

[10] F.N. Flakus, "Detecting and measuring ionizing radiation - a short history", *IAEA Bulletins* **23**(4), pp. 31–36.

[11] Peter Rudolph and Manfred Mhlberg, "Basic problems of vertical bridgman growth of CdTe", *Materials Science and Engineering: B* **16**(13), pp. 8 – 16 (1993).

[12] P. Rudolph, "Fundamental studies on bridgman growth of CdTe", *Progress in Crystal Growth and Characterization of Materials* **29**, pp. 275 – 381 (1994).

[13] M. Funaki, T. Ozaki, K. Satoh, , and R. Ohno, "Growth and characterization of CdTe single crystals for radiation detectors", *Nuclear Instruments and Methods in Physics Research Section A: Accelerators, Spectrometers, Detectors and Associated Equipment* **436**, pp. 120 – 126 (1999).

[14] H. Chen, S.A. Awadalla, J. Mackenzie, R. Redden, G. Bindley, A.E. Bolotnikov, G.S. Camarda, G. Carini, and R.B. James, "Characterization of traveling heater method (THM) grown Cd0.9Zn0.1Te crystals", *Nuclear Science, IEEE Transactions on* **54**(4), pp. 811 –816 (2007).

[15] S.A. Awadalla, J. Mackenzie, H. Chen, B. Redden, G. Bindley, M.C. Duff, A. Burger, M. Groza, V. Buliga, J.P. Bradley, Z.R. Dai, N. Teslich, and D.R. Black, "Characterization of detector-grade CdZnTe crystals grown by traveling heater method (THM)", *Journal of Crystal Growth* **312**(4), pp. 507 – 513 (2010).

[16] A. El Mokri, R. Triboulet, A. Lusson, A. Tromson-Carli, and G. Didier, "Growth of large, high purity, low cost, uniform CdZnTe crystals by the cold travelling heater method", *Journal of Crystal Growth* , pp. 168 – 174.

[17] Yue Wang, Katsuaki Kudo, Yuko Inatomi, Rongbin Ji, and Tetsuichi Motegi, "Growth interface of CdZnTe grown from Te solution with THM technique under static magnetic field", *Journal of Crystal Growth* **284**, pp. 406 – 411 (2005).

[18] U.N. Roy, S. Weiler, and J. Stein, "Growth and interface study of 2 in diameter CdZnTe by THM technique", *Journal of Crystal Growth* **312**(19), pp. 2840 – 2845 (2010).

[19] Carmen Stelian and Thierry Duffar, "Numerical modeling of CdTe crystallization from te solution under terrestrial and microgravity conditions", *Journal of Crystal Growth* **400**, pp. 67 – 75 (2014).

[20] J. D. Broder and G. A. Wolff, "A new method of GaP growth", *Journal of The Electrochemical Society* **110**(11), pp. 1150–1153 (1963).

[21] F. V. Wald and R. O. Bell, "Natural and forced-convection during solution growth of CdTe by traveling heater method (THM)", *Journal of Crystal Growth* **30**(1), pp. 29–36 (1975).

[22] C.J. Chang, B. Baird, P.K. Liao, R. Chang, and L. Colombo, "Finite element thermal analysis on the crystal growth of HgCdTe by the travelling heater method", *Journal of Crystal Growth* **98**(4), pp. 595 – 609 (1989).

[23] Yu.V. Apanovich and E.D. Ljumkis, "The numerical simulation of heat and mass transfer during growth of a binary system by the travelling heater method", *Journal of Crystal Growth* **110**(4), pp. 839 – 854 (1991).

[24] C. W. Lan and D. T. Yang, "A computer simulation of crystal growth by the traveling-solvent method (TSM): pseudo-steady-state calculations", *Modelling and Simulation in Materials Science and Engineering* **3**(1), pp. 71 (1995).

[25] X. Ye, B. Tabarrok, and D. Walsh, "The influence of thermosolutal convection on CdTe growth by the traveling heater method", *Journal of Crystal Growth* **169**(4), pp. 704 – 714 (1996).

[26] R.U. Barz, G. Gerbeth, U. Wunderwald, E. Buhrig, and Yu.M. Gelfgat, "Modelling of the isothermal melt flow due to rotating magnetic fields in crystal growth",

Journal of Crystal Growth **180**(34), pp. 410 – 421 (1997), Modelling in Crystal Growth.

[27] C. K. Ghaddar, C. K. Lee, S. Motakef, and D. C. Gillies, "Numerical simulation of THM growth of CdTe in presence of rotating magnetic fields (RMF)", *Journal of Crystal Growth* **205**(1-2), pp. 97 – 111 (1999).

[28] M.C. Martínez-Tomás, V. Muñoz-Sanjosé, and C. Reig, "A numerical study of thermal conditions in the THM growth of HgTe", *Journal of Crystal Growth* **243**(3-4), pp. 463 – 475 (2002).

[29] Y. Okano, S. Nishino, S. Ohkubo, and S. Dost, "Numerical study of transport phenomena in the THM growth of compound semiconductor crystal", *Journal of Crystal Growth* **237–239**, pp. 1779–1784 (2002).

[30] Y. Liu, S. Dost, B. Lent, and R. F. Redden, "A three-dimensional numerical simulation model for the growth of CdTe single crystals by the travelling heater method under magnetic field", *Journal of Crystal Growth* **254**(3-4), pp. 285 – 297 (2003).

[31] S. Dost and Y.C. Liu, "Controlling the growth interface shape in the growth of CdTe single crystals by the traveling heater method", *Comptes Rendus Mecanique* **335**(5-6), pp. 323 – 329 (2007).

[32] W. W. Mullins and R. F. Sekerka, "Stability of a planar interface during solidification of a dilute binary alloy", *Journal of Applied Physics* **35**(2), pp. 444–451 (1964).

[33] E. Scheil, "Bemerkungen zur schichtkristallbildung", *Z. Mettalk.* **34**, pp. 70 (1942).

[34] V. G. Smith, W. A. Tiller, and J. W. Rutter, "A mathematical analysis of solute redistribution during solidification", *Canadian J. Phys.* **33**, pp. 723–745 (1955).

[35] R. A. Brown and D. H. Kim, "Modeling of directional solidification: From Scheil to detailed numerical simulation", *J. Crystal Growth* **109**, pp. 50–65 (1991).

[36] Oleg Weinstein and Simon Brandon, "Dynamics of partially faceted melt/crystal interfaces I: Computational approach and single step–source calculations", *J. Crystal Growth* **268**(1–2), pp. 299–319 (2004).

[37] P. Moskvin, V. Khodakovsky, L. Rashkovetskyi, and A. Stronski, "Polyassociative model of A^2B^6 semiconductor melt and p–T–x equilibria in Cd–Hg–Te system", *Journal of Crystal Growth* **310**, pp. 2617–2626 (2008).

[38] N. Zhang, A. Yeckel, A. Burger, Y. Cui, K.G. Lynn, and J.J. Derby, "Anomalous segregation during electrodynamic gradient freeze growth of cadmium zinc telluride", *Journal of Crystal Growth* **325**(1), pp. 10 – 19 (2011).

[39] J. J. Derby and A. Yeckel, "Heat transfer analysis and design for bulk crystal growth: Perspectives on the Bridgman method", In T. Nishinaga and P. Rudolph, editors, *Handbook of Crystal Growth* , pp. 793–843. Elsevier second edition (2015).

[40] J. Fainberg, D. Vizman, J. Friedrich, and G. Müller, "A new hybrid method for the global modeling of convection in CZ crystal growth configurations", *J. Crystal Growth* **303(1)**, pp. 124–134 (2007).

[41] Crystal Growth Laboratory, Fraunhofer IISB, *CrysMAS User Manual and Tutorial* (2003), `https://download.iisb.fraunhofer.de/downloads/Manual/index.html`.

[42] A. S. Senchenkov, M. Fiederle, and N. N. Kolesnikov, "CZT crystal growth by THM in microgravity - preparation of experiments for FOTON-M4 mission", In *The 65th International Astronautical Congress* Toronto, Canada (2014).

[43] Jacques Steininger, Alan J. Strauss, and Robert F. Brebrick, "Phase diagram of the ZnCdTe ternary system", *Journal of The Electrochemical Society* **117**(10), pp. 1305–1309 (1970).

[44] S. Sen, W.H. Konkel, S.J. Tighe, L.G. Bland, S.R. Sharma, and R.E. Taylor, "Crystal growth of large-area single-crystal CdTe and CdZnTe by the computer-controlled vertical modified-Bridgman process", *Journal of Crystal Growth* **86**(1), pp. 111 – 117 (1988).

[45] C. Y. Ho, R. W. Powell, and P. E. Liley, "Thermal conductivity of the elements", *Journal of Physical and Chemical Reference Data* **1**(2), pp. 279–421 (1972).

[46] Y.S. Touloukian and D.P. DeWitt, *Thermophysical properties of matter - The TPRC data series. Volume 7. Thermal radiative properties - Metallic elements and alloys*, Thermophysical and Electronic Properties Information Analysis Center Lafayette, IN (1970).

[47] Shen Zhu, C. Li, Ching-Hua Su, B. Lin, H. Ban, R.N. Scripa, and S.L. Lehoczky, "Thermal diffusivity, thermal conductivity, and specific heat capacity measurements of molten tellurium", *Journal of Crystal Growth* **250**(1-2), pp. 269 – 273 (2003).

[48] V.M. Glazov, S.N. Chizhevskaia, and N.N. Glagoleva, *Liquid semiconductors*, Monographs in semiconductor physics. Plenum Press (1969).

[49] L Shcherbak, O Kopach, Yu Plevachuk, V Sklyarchuk, Ch Dong, and P Siffert, "The viscosity of liquid cadmium telluride", *Journal of Crystal Growth* **212**(3-4), pp. 385 – 390 (2000).

[50] C. Li, C.-H. Su, S. L. Lehoczky, R. N. Scripa, B. Lin, and H. Ban, "Thermophysical properties of liquid Te: Density, electrical conductivity, and viscosity", *Journal of Applied Physics* **97**(8) (2005).

[51] E. Ko, M.M.G. Alemany, J.J. Derby, and J.R. Chelikowsky, "Ab initio simulations of nonstoichiometric Cd_xTe_{1-x} liquids", *The Journal of Chemical Physics* **123**(8), pp. 084508 (2005).

[52] V. V. Godlevsky, J. J. Derby, and J. R. Chelikowsky, "*Ab initio* molecular dynamics simulations of liquid CdTe and GaAs: Semiconducting versus metallic behavior", *Phys. Rev. Lett.* **81**, pp. 4959–4962 (1998).

[53] Vitaliy V. Godlevsky, Manish Jain, Jeffrey J. Derby, and James R. Chelikowsky, "First-principles calculations of liquid CdTe at temperatures above and below the melting point", *Physical Review B* **60**(12), pp. 8640–8649 (1999).

[54] J. R. Chelikowsky, Jeffrey J. Derby, Vitaliy V. Godlevsky, Manish Jain, and J. Y. Raty, "*Ab initio* simulations of liquid semiconductors using the pseudopotential-density functional method", *J. Phys.: Condens. Matter* **13**, pp. R817–R854 (2001).

[55] V. M. Glazov, S. N. Chizhevskaya, and N. N. Glagoleva, *Liquid Semiconductors*, Plenum New York (1969).

[56] J. Akola, R. O. Jones, S. Kohara, T. Usuki, and E. Bychkov, "Density variations in liquid tellurium: Roles of rings, chains, and cavities", *Phys. Rev. B* **81**, pp. 094202 (2010).

[57] Philip M. Gresho and Robert L. Sani, *Incompressible Flow and the Finite Element Method*, Wiley, Chichester, New York (2000).

[58] A. Yeckel and R.T. Goodwin III, *Cats2D (Crystalization and Transport Simulator) User Manual* (2003), `http://www.msi.umn.edu/~yeckel/cats2d.html`.

[59] A. Yeckel, A.G. Salinger, and J.J. Derby, "Theoretical analysis and design considerations for float-zone refinement of electronic grade silicon sheets", *Journal of Crystal Growth* **152**, pp. 51 – 64 (1995).

[60] Gaurab Samanta, Andrew Yeckel, Edith D. Bourret-Courchesne, and Jeffrey J. Derby, "Parametric sensitivity and temporal dynamics of sapphire crystal growth via the micro-pulling-down method", *Journal of Crystal Growth* **359**, pp. 99 – 106 (2012).

[61] Andrew Yeckel, Prodromos Daoutidis, and Jeffrey J. Derby, "Stabilizing detached bridgman melt crystal growth: Model-based nonlinear feedback control", *Journal of Crystal Growth* **361**, pp. 16 – 24 (2012).

[62] Parthiv Daggolu, Andrew Yeckel, Carl E. Bleil, and Jeffrey J. Derby, "Stability limits for the horizontal ribbon growth of silicon crystals", *Journal of Crystal Growth* **363**, pp. 132 – 140 (2013).

[63] G. K. Batchelor, *An Introduction to Fluid Dynamics*, Cambridge University Press (1967).

[64] T. Jasinski and A. F. Witt, "On control of the crystal melt interface shape during growth in a vertical Bridgman configuration", *J. Crystal Growth* **71**, pp. 295–304 (1985).

[65] J. J. Derby, "Fluid dynamics in crystal growth: The good, the bad, and the ugly,", *Progress in Crystal Growth and Characterization of Materials* , p. in press (2016).

[66] H. K. Moffatt, "Viscous and resistive eddies near a sharp corner", *Journal of Fluid Mechanics* **18**, pp. 1–18 (1964).

[67] Carmen J. Nappo, "Fundamentals", In Carmen J. Nappo, editor, *An Introduction to Atmospheric Gravity Waves* volume 102 of *International Geophysics* , pp. 29 – 56. Academic Press (2012).

[68] Jeffrey H. Peterson, Andrew Yeckel, and Jeffrey J. Derby, "A fundamental limitation on growth rates in the traveling heater method", *Journal of Crystal Growth* **452**, pp. 12 – 16 (2016), ACCGE-20-OMVPE-17 (The 20th American Conference on Crystal Growth and Epitaxy in conjunction with the 17th US Biennial Workshop on Organometallic Vapor Phase Epitaxy, August 2-7, 2015, Big Sky, MT, USA).

[69] W. A. Tiller, K. A. Jackson, J. W. Rutter, and B. Chalmers, "The redistribution of solute atoms during the solidification of metals", *Acta Metallugica* **1**, pp. 428–437 (1953).

[70] J. W. Rutter and B. Chalmers, "A prismatic substructure formed during solidification of metals", *Canadian Journal of Physics* **31**(1), pp. 15–39 (1953).

[71] A. Yeckel and J. J. Derby, "Effect of accelerated crucible rotation on melt composition in high-pressure vertical Bridgman growth of cadmium zinc telluride", *J. Crystal Growth* **209**, pp. 734–750 (2000).

[72] A. Yeckel and J. J. Derby, "Buoyancy and rotation in small-scale vertical Bridgman growth of cadmium zinc telluride using accelerated crucible rotation", *J. Crystal Growth* **233**, pp. 599–608 (2001).

[73] Zaoyang Li, Jeffrey H. Peterson, Andrew Yeckel, and Jeffrey J. Derby, "Analysis of the effects of a rotating magnetic field on the growth of cadmium zinc telluride by the traveling heater method under microgravity conditions", *Journal of Crystal Growth* , p. in press (2016).

[74] Percy W. Bridgman, "Nobel lecture: General survey of certain results in the field of high-pressure physics", *Nobelprize.org* (1946).

[75] P. W. Bridgman, "Certain physical properties of single crystals of tungsten, antimony, bismuth, tellurium, cadmium, zinc, and tin", *Proceedings of the American Academy of Arts and Sciences* **60**(6), pp. 305–383 (1925).

[76] Edwin C.. Kemble and Francis Birch, *Percy Williams Bridgman, 1882 - 1961*, Columbia University Press (1970).

[77] Donald C. Stockbarger, "The production of large single crystals of lithium fluoride", *Review of Scientific Instruments* **7**(3) (1936).

[78] M.P. Volz, M. Schweizer, N. Kaiser, S.D. Cobb, L. Vujisic, S. Motakef, and F.R. Szofran, "Bridgman growth of detached gesi crystals", *Journal of Crystal Growth* **237 239, Part 3**, pp. 1844 – 1848 (2002), The thirteenth international conference on Crystal Growth in conj unction with the eleventh international conference on Vapor Growth and Epitaxy.

[79] Kazuo Nakajima, Toshihiro Kusunoki, Yukinaga Azuma, Noritaka Usami, Kozo Fujiwara, Toru Ujihara, Gen Sazaki, and Toetsu Shishido, "Compositional variation in si-rich sige single crystals grown by multi-component zone melting method using si seed and source crystals", *Journal of Crystal Growth* **240**(34), pp. 373 – 381 (2002).

[80] Yongcai Liu, Alexander Virozub, and Simon Brandon, "Facetting during directional growth of oxides from the melt: coupling between thermal fields, kinetics and melt/crystal interface shapes", *Journal of Crystal Growth* **205**(3), pp. 333 – 353 (1999).

[81] X.M. Li and J.Y. Xu, "Bridgman growth of zno crystals from high temperature solution", *Applied Physics A* **82**(2), pp. 373–376 (2006).

[82] W. A. Tiller, In J. J. Gilman, editor, *The Art and Science of Growing Crystals* , p. 276. Wiley (1963).

[83] Chong E. Chang and William R. Wilcox, "Control of interface shape in the vertical bridgman-stockbarger technique", *Journal of Crystal Growth* **21**(1), pp. 135 – 140 (1974).

[84] Ta-Wei Fu and William R. Wilcox, "Influence of insulation on stability of interface shape and position in the vertical bridgman-stockbarger technique", *Journal of Crystal Growth* **48**(3), pp. 416 – 424 (1980).

[85] T. Jasinski and A.F. Witt, "On control of the crystal-melt interface shape during growth in a vertical bridgman configuration", *Journal of Crystal Growth* **71**(2), pp. 295 – 304 (1985).

[86] K. Taghavi and W.M.B. Duval, "Inverse heat transfer analysis of bridgman crystal growth", *International Journal of Heat and Mass Transfer* **32**(9), pp. 1741 – 1750 (1989).

[87] M.P. Volz, K. Mazuruk, M.D. Aggarwal, and A. Cröll, "Interface shape control using localized heating during bridgman growth", *Journal of Crystal Growth* **311**(8), pp. 2321 – 2326 (2009).

[88] Satheesh Kuppurao and Jeffrey J. Derby, "Designing thermal environments to promote convex interface shapes during the vertical bridgman growth of cadmium zinc telluride", *Journal of Crystal Growth* **172**(3), pp. 350 – 360 (1997).

[89] C.W Lan, M.C Su, and M.C Liang, "A visualization and computational study of horizontal bridgman crystal growth", *Journal of Crystal Growth* **208**(14), pp. 717 – 725 (2000).

[90] Jeffrey H. Peterson, Michael Fiederle, and Jeffrey J. Derby, "Analysis of the traveling heater method for the growth of cadmium telluride", *Journal of Crystal Growth* **454**, pp. 45 – 58 (2016).

[91] Zaoyang Li, Jeffrey H. Peterson, Andrew Yeckel, and Jeffrey J. Derby, "Analysis of the effects of a rotating magnetic field on the growth of cadmium zinc telluride

by the traveling heater method under microgravity conditions", *Journal of Crystal Growth* , pp. – (2016).

[92] H.J. Scheel and E.O. Schulz-Dubois, "Flux growth of large crystals by accelerated crucible-rotation technique", *Journal of Crystal Growth* **8**(3), pp. 304 – 306 (1971).

[93] E.O. Schulz-Dubois, "Accelerated crucible rotation: Hydrodynamics and stirring effect", *Journal of Crystal Growth* **12**(2), pp. 81 – 87 (1972).

[94] P. Capper, J.J.G. Gosney, and C.L. Jones, "Application of the accelerated crucible rotation technique to the bridgman growth of CdxHg1 xTe: Simulations and crystal growth", *Journal of Crystal Growth* **70**(1), pp. 356 – 364 (1984).

[95] P. Capper, W.G. Coates, C.L. Jones, J.J. Gosney, C.K. Ard, and I. Kenworthy, "Quenching studies in CdxHg1xTe crystals grown using {ACRT}", *Journal of Crystal Growth* **83**(1), pp. 69 – 76 (1987).

[96] C.W Lan and J.H Chian, "Effects of ampoule rotation on vertical zone-melting crystal growth: steady rotation versus accelerated crucible rotation technique (acrt)", *Journal of Crystal Growth* **203**(12), pp. 286 – 296 (1999).

[97] R. U. Barz, P. Sabhapathy, and M. Salcudean, "A numerical study of convection during THM growth of CdTe with ACRT", *J. Crystal Growth* **180**, pp. 566–577 (1997).

[98] D.T.J. Hurle, "On similarities between the theories of morphological instability of a growing binary alloy crystal and Rayleigh-Bnard convective instability", *Journal of Crystal Growth* **72**(3), pp. 738 – 742 (1985).

[99] Esteban Meca and Mathis Plapp, "Phase-field study of the cellular bifurcation in dilute binary alloys", *Metallurgical and Materials Transactions A* **38**(7), pp. 1407–1416 (2007).

[100] Andrew Yeckel and Jeffrey J. Derby, "The prospects for traveling magnetic fields to affect interface shape in the vertical gradient freeze growth of cadmium zinc telluride", *Journal of Crystal Growth* **364**, pp. 133 – 144 (2013).

[101] S. Motakef, P. Becla, K. Becla, I. Abselem, M. Overholt, and A. Datta, "Control of te inclusion size distribution in cdznte crystals through exogenous modification of convection during thm growth", Presented at the 2016 IEEE Nuclear Science Symposium in Strasbourg, Germany.

[102] Jeffrey H. Peterson and Jeffrey J. Derby, "An axial temperature profile curvature criterion for the engineering of convex crystal growth interfaces in bridgman systems", *Journal of Crystal Growth* , pp. – (2016).

Appendix A

License agreements allowing reproduction of published work in this thesis

Contents from three publications by the author were used in writing this thesis [90, 68, 102]. The author has permission from the publisher of these works for the sole use of reproduction in this thesis through licenses 4000511233198, 4017840411408, and 4018290279503 with Elsevier.